

# Tunable Microwave Resonator Using Liquid Metal And 3D Printed Fluidic Channel For The Development Of Microwave Spectroscopy

by

Md. Abdur Rafi

B.Sc. Engg., Islamic University of Technology (IUT), 2016

A THESIS SUBMITTED IN PARTIAL FULFILLMENT OF  
THE REQUIREMENTS FOR THE DEGREE OF

MASTER OF APPLIED SCIENCE

in

THE COLLEGE OF GRADUATE STUDIES

(Electrical Engineering)

THE UNIVERSITY OF BRITISH COLUMBIA

(Okanagan)

January 2021

© Md. Abdur Rafi, 2021

---

The following individuals certify that they have read, and recommend to the College of Graduate Studies for acceptance, a thesis/dissertation microelectronics:

TUNABLE MICROWAVE RESONATOR USING LIQUID METAL AND 3D  
PRINTED FLUIDIC CHANNEL FOR THE DEVELOPMENT OF MICROWAVE  
SPECTROSCOPY

submitted by MD. ABDUR RAFI in partial fulfilment of the requirements of the degree of Master of Applied Science

Dr. Mohammad Hossein Zarifi, School of Engineering  
**Supervisor**

Dr. Ian Foulds, School of Engineering  
**Supervisory Committee Member**

Dr. Kevin Golovin, School of Engineering  
**Supervisory Committee Member**

Dr. Sina Kheirkhah, School of Engineering  
**University Examiner**

# Abstract

This thesis presents an innovative and practical approach to developing planar resonant-based spectroscopy in microwave sensor technology. Resonant based microwave sensors have drawn attention for decades now in terms of sensing and measuring materials dielectric properties because of demonstrating a higher accuracy, precision, and sensitive measurement compared to non-resonant based sensors. This method has been mostly used on binary solvents due to their ability to display a highly delicate response to the materials under test. This thesis presents a comprehensive analysis of the sensor design and fabrication, sensor characterization, and testing samples to achieve the materials' frequency selective response.

Microwave resonator sensors are limited in their current form to a single fixed resonant frequency, leading to issues in selectivity among materials or mixtures with similar dielectric properties. The first study presents a successful effort of achieving a frequency-tunable resonator circuit by utilizing the liquid metal and 3D printed microchannel with a modified split ring resonator. The resonator utilizes liquid metal in a microfluidic channel to change the resonant frequency of the resonator over a wide, continuous spectrum by changing the effective capacitance of the sensor. In the second study, highly sensitive interdigitated capacitive traces have been added with the designed sensor structure for material sensing. The designed and fabricated sensor demonstrated an operating resonant frequency that could be tuned between 2.1 and 2.8 GHz for both solid and liquid sensing. The sensitivity of the designed sensor structure is investigated by sensing standard solid samples, and sensitivity variation was noticed due to the increased reactive loading introduced by the liquid metal.

Experimental validation of the sensor and standard liquid mixtures confirmed that the frequency tunability enables similar dielectric materials to be distinctly identified using multiple frequency spectra. Specific attention was made towards materials with identical dielectric properties at specific frequencies, simulated with the Debye model, and matched experimentally with dielectric probe validation. The device enables multi-phase material detection with the ability to investigate dielectric properties over a frequency

*Abstract*

---

spectrum rather than a single point.

# Lay Summary

This thesis demonstrates a successful approach to detecting materials in different phases using a resonant based spectroscopy method. The designed structures were employed in multiple independent studies in order to achieve material identification in different resonant frequencies. The initial study discusses the frequency tuning capability of the designed structure by utilizing the potential application of liquid metal in a 3D printed microfluidic channel. The second study shows a modification in the designed structure and includes performance characterization of the designed sensor by sensing standard solid samples in different tunable resonant frequencies. In the third study, coaxial probe measurements indicate the liquid samples that exhibit similar dielectric properties at a frequency, which defines the inability to sense those samples using a single fixed resonant frequency. In the final study, the designed tunable resonant structure was successfully utilized to identify samples of identical dielectric properties in microwave sensor technology.

# Preface

This work has been performed under the guidance of Dr. Mohammad Hossein Zarifi at the School of Engineering at The University of British Columbia. The fourth chapter of this thesis contains materials that have been published in the following journal:

- Wideband Tunable Modified Split Ring Resonator Structure Using Liquid Metal and 3-D Printing, *IEEE Microwave and Wireless Components Letters*, vol. 30, no. 5, pp. 1–4, 2020.

The chapter five of this thesis has also been presented in the following journal for review:

- Continuously Tunable Resonator Development utilizing Liquid Metal to generate Spectroscopic Data for Multi-phase Material Identification, *IEEE Transactions on Microwave Theory and Techniques*.

# Table of Contents

<b>Abstract</b> . . . . .	<b>iii</b>
<b>Lay Summary</b> . . . . .	<b>v</b>
<b>Preface</b> . . . . .	<b>vi</b>
<b>Table of Contents</b> . . . . .	<b>vii</b>
<b>List of Tables</b> . . . . .	<b>x</b>
<b>List of Figures</b> . . . . .	<b>xi</b>
<b>Acknowledgements</b> . . . . .	<b>xvii</b>
<b>Dedication</b> . . . . .	<b>xviii</b>
<b>Chapter 1: Introduction</b> . . . . .	<b>1</b>
1.1 Motivation . . . . .	1
1.2 Objective . . . . .	3
1.3 Thesis Organization . . . . .	3
<b>Chapter 2: Introduction to microwave technology, planar transmission lines and measurement techniques</b> . . . . .	<b>5</b>
2.1 Introduction to microwave technology . . . . .	5
2.2 Planar transmission lines . . . . .	7
2.2.1 Microstrip . . . . .	7
2.2.2 Coplanar waveguide . . . . .	8
2.2.3 Coplanar strip and differential line . . . . .	8
2.2.4 Stripline . . . . .	9
2.2.5 Embedded differential line . . . . .	9
2.3 Microwave technology in material detection . . . . .	9

TABLE OF CONTENTS

---

2.4	Different measurement techniques in microwave technology . . .	13
2.4.1	Transmission/reflection (TR) line method . . . . .	13
2.4.2	Open-ended coaxial probe method . . . . .	14
2.4.3	Free space method . . . . .	16
2.4.4	Resonant method . . . . .	17
<b>Chapter 3: Planar microstrip resonator, tuning mechanisms and microwave spectroscopy . . . . .</b>		<b>20</b>
3.1	Planar Microstrip Resonator . . . . .	20
3.1.1	Theory of operation . . . . .	20
3.1.2	Resonant frequency and quality factor . . . . .	24
3.1.3	Split ring resonator . . . . .	27
3.2	Tuning Mechanisms . . . . .	30
3.2.1	External devices . . . . .	30
3.2.2	Microfluidic-based tuning . . . . .	32
3.3	Review of Microfluidic Applications . . . . .	33
3.3.1	Challenges and limitations of microfluidic based tuning	35
3.3.2	Microfluidic Channel . . . . .	38
3.4	Microwave Spectroscopy . . . . .	40
<b>Chapter 4: Adjustable Microwave Resonator . . . . .</b>		<b>44</b>
4.1	Design and Simulation . . . . .	44
4.1.1	Design methodology of the resonator structure . . . . .	45
4.1.2	Design methodology of the fluidic channel . . . . .	49
4.1.3	Structural simulation . . . . .	51
4.2	Fabrication and Experimental Setup . . . . .	56
4.2.1	Fabrication of highly coupled resonator structure . . . . .	56
4.2.2	3D printed fluidic channel . . . . .	57
4.2.3	Experimental setup . . . . .	60
4.3	RF Characterization . . . . .	60
4.3.1	Scattering (s) parameter measurement . . . . .	61
4.3.2	Equivalent circuit modeling . . . . .	64
4.3.3	Results comparison . . . . .	65
4.4	Chapter summary . . . . .	67
<b>Chapter 5: Resonant Based Spectroscopy for multi-phase ma- terial detection . . . . .</b>		<b>68</b>
5.1	Problem statement . . . . .	68
5.2	Operating principle of the designed resonator sensor . . . . .	70
5.3	Design methodology and simulation . . . . .	71

*TABLE OF CONTENTS*

---

5.3.1	Structure design and tunable operation . . . . .	71
5.3.2	Sensitivity analysis of the designed sensor . . . . .	75
5.3.3	Sensor performance analysis . . . . .	79
5.4	Experimental setup and measurement discussion . . . . .	80
5.4.1	Characterizing the designed resonator sensor . . . . .	80
5.4.2	Standard probe measurement . . . . .	85
5.4.3	Validation of the designed resonator sensor . . . . .	90
5.5	Chapter summary . . . . .	95
<b>Chapter 6: Conclusion and Future Investigations . . . . .</b>		<b>97</b>
6.1	Thesis outcome and conclusion . . . . .	97
6.2	Future work . . . . .	98
<b>Bibliography . . . . .</b>		<b>100</b>

# List of Tables

Table 3.1	Comparison of different switching techniques . . . . .	33
Table 3.2	Comparison of physical properties of Copper, Galinstan, EGaIn and Mercury © 2015 IEEE . . . . .	36
Table 4.1	Design parameters of the designed modified resonator structure . . . . .	48
Table 4.2	Defining the values of the parameters of the equivalent circuit model based on the simulation results. . . . .	65
Table 5.1	Defining the values of the parameters of the designed sensor . . . . .	72
Table 5.2	Measured effective permittivity of the sample liquid solutions . . . . .	87
Table 5.3	Measured frequency difference due to sample liquids presence in microfluidic channel in different resonant frequencies. . . . .	94

# List of Figures

Figure 2.1	Electromagnetic frequency spectrum and associated wavelengths. . . . .	6
Figure 2.2	Cross sections of different planar transmission line structures where (a) microstrip, (b) coplanar waveguide, (c) coplanar strip and differential line, (d) stripline and (e) embedded differential line. . . . .	8
Figure 2.3	A dielectric with polar molecule: (a) in the absence of an external electric field $E_{ext}$ , (b) in the presence of an external electric field $E_{ext}$ and (c) the induced electric field $E_{ind}$ inside the dielectric produced by the induced surface charge $Q_i$ . . . . .	10
Figure 2.4	Complex dielectric permittivity spectrum over a range of frequencies where $\epsilon'$ and $\epsilon''$ denote the real and imaginary part, respectively. . . . .	12
Figure 2.5	Measurement using TR method with a waveguide . . .	13
Figure 2.6	Experimental setup of an open-ended coaxial probe method. . . . .	15
Figure 2.7	Measurement of sample under test using free space method. . . . .	16
Figure 2.8	Measurement of a thin rod using resonant method. . .	18
Figure 3.1	Lumped element representation of an infinitesimal part $\Delta Z$ of a microstrip transmission line where (a) the actual microstrip and (b) the modelled microstrip. . . . .	21
Figure 3.2	Electric (E-field) and magnetic (H-field) field distribution of a microstrip line. . . . .	22
Figure 3.3	Lumped element model of a microstrip resonant circuit. . . . .	23
Figure 3.4	Quality Factor of a resonant circuit. . . . .	26
Figure 3.5	A simple split ring resonator structure coupled with feedline. . . . .	27

*LIST OF FIGURES*

---

Figure 3.6	(a) Resonator sensor structure implemented in HFSS for the purpose of early detection breaches in pipeline coatings and (b) open split ring resonator structure (OSRR) . . . . .	28
Figure 3.7	Some geometries of split ring resonator (SRR). (a) Double split ring resonator, (b) Double split square resonator, (c) Singly split ring resonator, (d) Two-turn spiral (circular) resonator, (e) Two-turn spiral (rectangular) resonator and (f) Modified ring resonator.	29
Figure 3.8	Tuning by the external devices. (a) SRR with capacitor loaded, (b) Varactor loaded S-shaped resonator and (c) RF-MEMS loaded microstrip patch antenna.	31
Figure 3.9	Microfluidic based tuning. (a) Implemented prototype of the microfluidic waveguide switch, (b) Reconfigurable CPW folded slot antenna. . . . .	34
Figure 3.10	A liquid metal plug sandwiched between the carrier fluid inside the microfluidic channel. . . . .	36
Figure 3.11	(a) A mm syringe and (b) 11 Pico Plus Elite programmable syringe to control the liquid flow. . . . .	37
Figure 3.12	(a) EGaIn plug inside a PDMS and (b) 3D printed structure utilized as a microfluidic channel. . . . .	39
Figure 3.13	Dielectric spectra of soybean oil at 25°C temperature over a broadband where (a) real part and (b) imaginary part. . . . .	40
Figure 3.14	CPW folded slot antenna integrated with liquid metal to achieve three different frequency bands of 2.4, 3.5 and 5.8 GHz. . . . .	41
Figure 4.1	Pictorial depiction of the device development process.	44
Figure 4.2	Simple SRR integrated with (a) no microfluidic channel (MC), (b) one MC, (c) two MC, (d) three MC and (e) four MC filled with liquid metal, and (f) simulation result of different configurations of MC filled liquid metal. . . . .	46
Figure 4.3	Frequency spectra of a simple SRR with varying liquid metal inside the fluidic channel. . . . .	47
Figure 4.4	Designed highly coupled modified SRR structure with dimensions. . . . .	48

*LIST OF FIGURES*

---

Figure 4.5	(a) The cross-section of the designed fluidic channel, (b) channel height ( $h=$ ) 1.5 mm, width ( $w=$ ) 2.0 mm and channel separation ( $d_1=$ ) 50 $\mu$ m and (c) channel length ( $L=$ ) 3 cm. . . . .	50
Figure 4.6	Resonant frequency shift at different widths when liquid metal (LM) length is 32mm, 26mm and 20mm. . . . .	51
Figure 4.7	Layout of the designed resonator integrated with fluidic channel. . . . .	52
Figure 4.8	Cross-sectional sideview of the designed resonator integrated with fluidic channel. . . . .	53
Figure 4.9	Transmission spectra ( $S_{21}$ ) of the designed resonator structure for (a) different gap sizes, $g$ and (b) different coupling distances, $d$ . . . . .	53
Figure 4.10	Transmission spectra ( $S_{21}$ ) of the designed resonator structure. . . . .	54
Figure 4.11	EM field distribution plot of the designed resonator structure from HFSS at a resonance of 3.52 GHz. . . . .	55
Figure 4.12	Fabricated resonator structure on Rogers RT/duroid 5880 high-frequency substrate and SMA connectors are soldered with the feedlines. . . . .	57
Figure 4.13	(a) Fabricated PDMS microchannel and (b) the designed resonator structure integrated with the PDMS microchannel. . . . .	58
Figure 4.14	Fabricated resonator integrated with 3D printed fluidic channel. . . . .	58
Figure 4.15	Surface profile of the 3D printed fluidic channel along the length A to C. . . . .	59
Figure 4.16	Surface profile of the embedded channel inside the 3D printed structure. . . . .	60
Figure 4.17	Experimental setup used to measure the $S_{21}$ response of the tunable resonator. The fabricated resonator filled with liquid metal and microchannel implementation is shown in the top-left inset. . . . .	61
Figure 4.18	Frequency spectra from structure simulation for different liquid metal amounts. Few of the instances of liquid metal inside the channel is shown on the left side. . . . .	62

*LIST OF FIGURES*

---

Figure 4.19	Resonant $S_{21}$ spectra recorded by the VNA as the volume of metal inside the channel is varied. Few of the instances of liquid metal inside the channel are shown on the left side. . . . .	63
Figure 4.20	Equivalent circuit model overlaying the substrate, resonator and liquid metal. . . . .	64
Figure 4.21	Comparison between the simulated (HFSS and ADS) and measured $S_{21}$ frequency spectra for the resonator with the fluidic channel in a (a) empty state and (b) filled state. . . . .	66
Figure 4.22	Resonant frequencies recorded for different metal lengths with selected images included. . . . .	66
Figure 5.1	The calculated dielectric complex permittivity of material A and material B at 23.7°C modelled by Debye method. The parameters for material A were set to match water: $\epsilon_s=76.58$ $\epsilon_\infty=4.73$ $\tau=9.3$ ps. Material B was defined by $\epsilon_s=87.37$ $\epsilon_\infty=68.13$ $\tau=90.9$ ps. . . .	69
Figure 5.2	Structural design of the proposed resonator sensor with dimensions. . . . .	71
Figure 5.3	$S_{21}$ response of the unloaded resonator from the HFSS simulation software. . . . .	72
Figure 5.4	Field distribution plot (a) Electric field distribution at 2.57 GHz and (b) Magnetic field distribution at 2.75 GHz. . . . .	73
Figure 5.5	(a) Layout of the sensor structure from the HFSS software, (b) simulations results from HFSS when the channel is filled with liquid metal in the length of 18-32 mm of microfluidic channel referenced with unloaded resonator response, (c) change in resonant frequency and (d) resonant amplitude with varying length of liquid metal. . . . .	74
Figure 5.6	(a) Simulations results from HFSS when liquid metal is filled in the length of 25 mm of the microfluidic channel, and different solid materials are tested and (b) scatter plot indicating the achieved resonant frequencies over materials with different permittivity. . .	75
Figure 5.7	Frequency difference over different dielectric constant materials when liquid metal is in different locations inside the microfluidic channel. . . . .	76

*LIST OF FIGURES*

---

Figure 5.8	Simulation results from HFSS while varying loss tangent of test samples of permittivity 16.5, 10.0, and 5.7 at different liquid metal settings inside the microchannel. Varying loss tangent of test samples varies the amplitude of the sensor response while liquid metal is at (a) 18 mm, (b) 21.5 mm, (c) 25 mm, (d) 28.5 mm, and (e) 32 mm location. The magnification of the amplitude difference is shown in the bottom right inset at every liquid metal setting. . . . .	77
Figure 5.9	Amplitude difference compared against the loss tangent for a MUT of permittivity 10 at different locations of liquid metal. . . . .	78
Figure 5.10	Simulated result from HFSS while testing the materials at (a) 2.258 GHz and (b) 2.55 GHz of frequency. . . . .	79
Figure 5.11	Experimental setup of the designed resonator used for testing standard samples (solid) at different resonant frequencies. The magnification of the sensor with MUT is inset in the top right corner. . . . .	81
Figure 5.12	Measured response of liquid metal being at different locations inside the microchannel resulting in tunable resonant frequencies. . . . .	82
Figure 5.13	Measured response of standard materials ( $\epsilon_r=2.20$ , 6.15 and 10.20) influencing resonant frequency of 2.68 GHz. . . . .	83
Figure 5.14	Measured response of standard material ( $\epsilon_r=6.15$ ) influencing different resonant frequencies. . . . .	84
Figure 5.15	Sensitivity of the designed resonator sensor by testing samples of permittivity 2.20, 6.15 and 10.20 in different resonant frequency. . . . .	85
Figure 5.16	Experimental setup of the coaxial probe measurement. . . . .	86
Figure 5.17	Measured real ( $\epsilon'$ ) and imaginary part ( $\epsilon''$ ) of the complex permittivity of different solutions where (a) 15% ethanol-water and 10% IPA-water, (b) 30% ethanol-water and 25% IPA-water, (c) 40% ethanol-water and 35% IPA-water and (d) 65% ethanol-water and 55% IPA-water. . . . .	88
Figure 5.18	Dielectric response of (a) 80% and 85% ethanol-water compared with pure methanol and (b) 80% and 85% IPA-water compared with pure ethanol. . . . .	89

*LIST OF FIGURES*

---

Figure 5.19	Experimental setup of the designed sensor used for sensing liquid samples of pure methanol, pure ethanol, 81% ethanol-water and 83% IPA-water solutions at different resonant frequencies. . . . .	91
Figure 5.20	Measured frequency shift due to the presence of pure methanol and 81% ethanol-water at resonant frequencies of (a) 2.817 GHz, (b) 2.719 GHz, and (c) 2.685 GHz. The corresponding liquid metal position and frequency shifts are shown in the top right inset and bottom right inset, respectively. . . . .	92
Figure 5.21	Measured frequency shift due to the presence of pure ethanol and 83% ethanol-water at resonant frequencies of (a) 2.817 GHz, (b) 2.719 GHz and (c) 2.685 GHz. . . . .	93

# Acknowledgements

Some of the very important people need to be recognized here because of their unwavering support and mindful contribution to my thesis. I would like to begin by thanking Prof. Mohammad Hossein Zarifi, my supervisor, who encouraged me in the first place to pursue master's in microwave resonator technology. His continuous assistance and tenacious encouragement always push me beyond my level to achieve the desire. Every meeting with him brings a new idea and inspires me to think outside the box. His mentorship has provided me with so many new prospects, and I have learned a great deal from him. While working with him, I have learned so many technical details and developed a tremendous theoretical knowledge which will help me further. His undiluted guidance and sincere advice help me develop many more skills that I can utilize in my professional and personal life. I consider myself very fortunate to work under the supervision of such a generous and encouraging professor like him.

I would also like to thank my committee members, Prof. Ian Foulds, Prof. Kevin Golovin, and Prof. Sina Kheirkhah, for their excellent guidance throughout the Master's program. Besides, I would like to acknowledge the contribution of the Natural Sciences and Engineering Research Council of Canada (NSERC) Discovery Grant Program, Canada Foundation for Innovation program for partial financial assistance, and CMC Microsystems for the use of their software and equipment.

I would like to extend my gratitude by thanking Benjamin Wiltshire, Ph.D. student, for mentoring me to the necessary software and hardware skills and being actively involved in developing and validating the presented work. His previous experience and in-depth knowledge benefit me to transform the failures into success. My sincere thanks go to my colleagues at the OMEGA (Okanagan Microelectronics & Gigahertz Application) Lab for all their support, constructive suggestions, and being open to questions at any time. Finally, I would like to appreciate my parents undivided attention throughout my post-graduate journey at the University of British Columbia. A special thanks to my wife, Nawshin Tabassum, for always being there as my mental support.

# Dedication

*To my father, Abdul Wazed,*  
who has always been my inspiration.

*To my mother, Abeda Begum,*  
who has always shown unconditional love and support.

*To my loving wife, Nawshin Tabassum,*  
who has always been there as a motivator and friend.

# Chapter 1

## Introduction

### 1.1 Motivation

Sensors play an important role in numerous modern industrial applications. The term “Sensor” generally refers to a device that detects events or changes in its environment and then provides a corresponding output, typically electrical or optical signals, read by an observer or by an instrument. Most sensors are electronic, but some are simple, such as a mercury-in-glass thermometer, which provides visual data. The use of sensors has grown beyond the most conventional fields of temperature, pressure, or flow measurement with developments in micro-machinery and easy-to-use microwave platforms. The preferred choice of sensors is determined by different aspects such as sensor cost, size, complexity, and the form of measurement. Microwave sensors have gained popularity regarding detecting and characterizing different materials of every state, such as solid, liquid, semi-liquid, and gas. It utilizes the microwave portion of the electromagnetic spectrum that occupies the wavelength range from approximately 1m to 1mm. Longer wavelength microwave radiation can pass through the cloud, wind, dust, snow, and this property enables microwave energy to be detected under almost all weather and environmental conditions. Moreover, microwave sensors are highly sensitive and can detect very small changes in the environment. Due to the characteristics, microwave sensors are widely used to detect and characterize different materials dielectric properties. Every material shows distinctive dielectric behavior based on the operating frequency due to their unique dielectric properties, thus transmitting different dielectric responses at different frequencies. Furthermore, microwaves have demonstrated other interesting sensing properties, such as low-cost, material interaction at various scales, compatibility with planar technology, and robustness.

Microwave sensors can be divided into resonant and non-resonant methods for the identification and characterization of dielectric materials. The non-resonant methods are based on wave propagation and suitable for broadband measurement. Resonant methods are more precise and appropriate

### 1.1. Motivation

---

for low loss material characterization; however, only a single frequency or a discrete number of frequencies may provide measurement results. The combination of sensor size and performance of a resonant-type sensor is hard to achieve with non-resonant methods. Compared to wide-band non-resonant structures, resonance dependent sensors have higher resolution in their performance, even though limited in the monitoring of discrete finite frequencies. Resonant sensors have the advantages of providing higher sensitivity, simpler signal processing, and lower cost compared to non-resonant sensors. This inspires researchers to integrate resonators into sensing actions, often at a single frequency, and extract the material's dielectric properties in various environments using the resonators behavioral variation. Recent investigations show a comprehensive versatile application scope of the microwave resonators.

Since microwave resonator sensors have already been successfully prominent in sensing solid, liquid, and gas, the innovation of tunable resonance optimizes the sensing technology more extensively. Tunable microwave resonator sensors can lower the cost much more due to its wideband performance and reusability. It also reduces the complexities of a microwave system by minimizing the number of circuits required for different operating conditions. Researchers have utilized different modes (harmonics) of resonators to detect materials dielectric properties in multiple points instead of one. This benefits in achieving more comprehensive data over multiple resonant points and understanding the material behavior at different frequencies. However, this technique limits the accuracy of the measurement when higher resonant modes are used to characterize the sample. In recent years, researchers employed liquid metal filled fluidic channel in different locations of a microwave resonator to tune resonant frequency into multiple resonant points. Despite the advantage of highly accurate material characterization over multiple resonant points, this technique can only provide two or three discrete resonant points over a wideband. Therefore, developing a continuously tunable microwave resonator would be very attractive for resonant-based spectroscopy development. Through this work, a proof of concept of developing a wideband continuously tunable microwave resonator for the development of resonant based microwave spectroscopy in microwave technology will be presented.

## 1.2 Objective

This thesis aims to design a wideband continuously tunable planar microwave resonator sensor to develop resonant-based microwave spectroscopy and utilize the resonant-based spectroscopy to sense materials of similar dielectric properties. The designed sensor should provide continuous tuning of resonant frequency and detect materials in multiple operating points. Considering the aim of the thesis, the objectives of this thesis work are presented below:

The first objective of this thesis is to design a planar microwave resonator structure to achieve user-controlled continuous tuning of resonant frequency over a wideband. To achieve this objective, the influence of liquid metal on the planar resonator has been investigated. Subsequently, the advantages of 3D printing technology have been fully utilized by creating 3D printed microchannels to guide the fluid. The entire process contains a suitable resonator structure design, use of the 3D printed fluidic channel, liquid metal integration, and optimization of the overall model to attain the desired aim. The progress of this objective will be measured by analyzing and comparing the data collected from the experiment and structural simulation. The achieved result should reflect continuous tuning of the resonant frequency of the user's interest over a wideband of frequency.

The second objective of this thesis is to utilize the developed resonant-based spectroscopy by tuning the resonant frequency to detect sample materials that exhibit similar dielectric properties. To achieve this objective, the designed resonant structure was modified and integrated with a newly fabricated 3D printed fluidic channel to guide the liquid metal and the material under test (MUT). Initially, solid samples of different dielectric properties were tested to characterize the designed sensor structure, followed by preparing liquid samples of similar dielectric properties. The progress of this objective was measured by analyzing the data collected from the measurement. The achieved result would show successful implementation of resonant-based spectroscopy of tuning the resonant frequency to detect samples of similar dielectric properties.

## 1.3 Thesis Organization

This thesis contains six chapters where Chapter 1 discusses the motivation and objectives of the work. Chapter 2 outlines an introduction to microwave technology and a discussion on different planar transmission

### 1.3. Thesis Organization

---

lines. The discussion then continuous to different available measurement techniques in microwave technology. Chapter 3 begins with the operating principle of the planar microstrip resonator in addition to a background investigation on different tuning mechanisms in microstrip resonator. The benefits of microwave spectroscopy in terms of material characterization is also identified and mentioned in this chapter. Chapter 4 presents the design methodology of the tunable microwave resonator and RF characterization of the designed resonator. The designed resonator's performance was validated by comparing the measured and simulated results and presented in this chapter. The developed tunable resonant structure was modified and utilized as a tool to successfully distinguish between samples of similar dielectric properties and detailed in terms of the design idea, and RF characterization is presented in chapter 5. Chapter 6 is devoted to the conclusion of the thesis that summarizes the thesis achievements and outlines some future study directions.

## Chapter 2

# Introduction to microwave technology, planar transmission lines and measurement techniques

This chapter starts with introducing microwave technology and is followed by presenting different planar transmission line structures. One of the significant applications of microwave technology is material detection in different environments, and the fundamentals of material detection in microwave technology are presented in this chapter. There are different measurement techniques available in microwave technology, and choosing the best one depends on the material structure and the frequency of interest. This chapter closes with a detailed discussion of different measurement techniques based on their operation, advantages and limitations, and frequency range.

### 2.1 Introduction to microwave technology

Electromagnetic rays with frequencies between 300 MHz and 300 GHz in the electromagnetic spectrum, with a corresponding electrical wavelength between 1m to 1mm, are referred to as microwaves. As compared with the waves used in radio broadcasting, microwaves are smaller. Their spectrum ranges from radio waves to infrared waves. Microwaves travel by line of sight, and the troposphere can impact them slightly. They do not require any medium to travel. Microwaves are reflected by metals and are partly transparent to nonmetals such as glass and particles [1].

Microwave is a portable communication line-of-sight platform that enables high-speed wireless connections to send and receive audio, video, and data information using high-frequency radio wave beams. Microwave connections are commonly used for point-to-point communications because their

## 2.1. Introduction to microwave technology

short wavelength enables easily sized antennas to direct them into narrow beams, directly guided at the receiving antenna. This allows microwave systems nearby to use the same frequencies without interfering with each other as radio waves of lower frequency do [2]. Another benefit is that the high microwave frequency has a very broad information-carrying capacity for the microwave band; the microwave band has a bandwidth 30 times that of all the rest of the radio spectrum below it. Figure 2.1 shows the electromagnetic spectrum to indicate the wavelength and frequency correlated with the various bands.

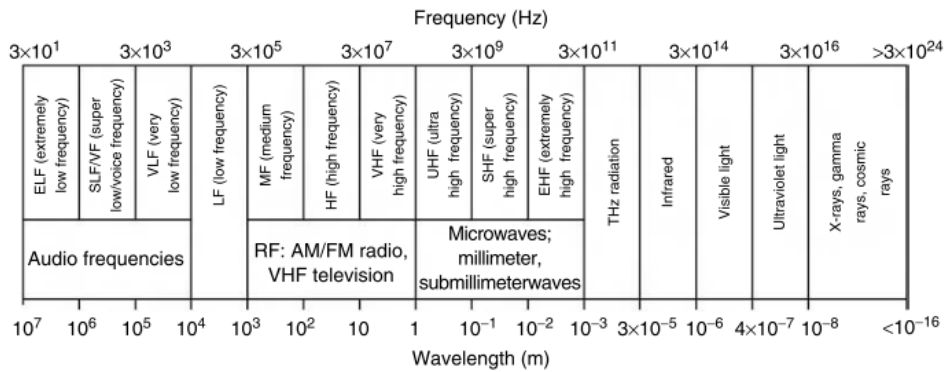


Figure 2.1: Electromagnetic frequency spectrum and associated wavelengths. Copyright © 2008 Taylor & Francis Group, LLC. All rights reserved [3].

Over the years, microwave technology has experienced substantial growth in terms of power consumption, scale, and cost due to the advancement of solid-state devices, technology for printed circuit boards, and integrated circuit technology. In satellite communications, radar signals, phones, and marine applications, microwaves are used most widely. Due to the enormous improvement in microwave technology, it is found to be utilized in various industries such as communication [4, 5], manufacturing, processing for drying and curing [6–10], healthcare [11–13] and food industry [14]. The use of microwave technology in biomedical and pharmaceutical applications widens the range of possibility of early detection of deadly diseases. Many important applications include detecting and monitoring food quality, drug research, human tissue characterization for tumor and cancer detection [15, 16], brain activities detection [17], concealed weapon detection [18] and motion detection [19]. Researchers prefer microwave technology due to its

low cost, robust, compact, non-contact, and label-free detection properties.

## 2.2 Planar transmission lines

In the early days, RF (radio frequency) and microwave systems depend on waveguides, two-wire lines, and coaxial lines for the low-loss transmission of power in high frequencies. Waveguides can handle high-power applications with low loss, but they are bulky and expensive. Two-wire lines are low-cost, but they lack shielding [20]. Coaxial lines are shielded, but they are a difficult medium to fabricate complex microwave components [20]. An alternative, in the form of strip lines, microstrip lines, slot lines, coplanar waveguides, and many other forms of similar geometries, is given by planar transmission lines [21]. Because of the trend toward miniaturization and integration, most modern microwave circuitry is fabricated using planar transmission lines such as microstrips and stripline rather than waveguides [20]. These transmission lines are lightweight, cost-effective, and easily integrated into active circuit devices to form integrated microwave circuits [20]. The most fascinating feature of planar transmission lines operating in microwave frequencies and beyond is that such lines can replace lumped elements, such as capacitances and inductances, thus eliminating lumped components that increase the complexity and costs of the circuit [21].

The configuration of the planar transmission line includes both the transmission line selection and the substrate. Each structure of the planar transmission line comprises a combination of metal and dielectric. In most cases, the dielectric primarily supports the metal pattern, serves as a substrate, and affects the wave's propagation. In this section, different types of planar transmission lines will be discussed.

### 2.2.1 Microstrip

The easiest structure to produce with a thin dielectric substrate with metal on both sides is the microstrip. One metal sheet is held as the electrical ground plane, while the other is patterned by way of photolithography. The metal is chemically etched to form a microstrip transmission network. The cross-section of a microstrip transmission line is shown in Figure 2.2(a). Under the current-carrying conductor traces, the ground plane avoids excessive field leakage and thereby reduces the radiation loss [22]. The presence of a ground plane in the backside of the substrate effectively isolates the structure from the backside region and prevents it from potential interference effects caused by other circuits or materials [21].

## 2.2. Planar transmission lines

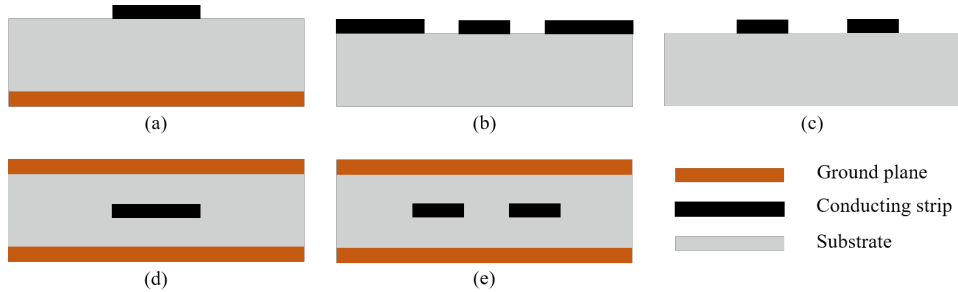


Figure 2.2: Cross sections of different planar transmission line structures where (a) microstrip, (b) coplanar waveguide, (c) coplanar strip and differential line, (d) stripline and (e) embedded differential line. Copyright © 2019 by M.B.Steer. All rights reserved [22].

### 2.2.2 Coplanar waveguide

Coplanar waveguide (CPW) can be formed with the active metallization and the ground planes on the same side of the substrate. Each side-plane conductor is grounded, and the signal is carried by the center strip, so as compared to the microstrip, much less field reaches the substrate. Due to the center conductor's presence and the proximity of the ground planes, coplanar waveguides are especially useful for making active circuitry [20]. CPW's may also be implemented with backside metallization (also known as conductor backed CPW's). However, due to the parasitic parallel-plate waveguides present on both sides of the CPW axis, this backside metallization can cause leaky-wave propagation [21]. The cross-sectional geometry of a CPW is shown in Figure 2.2(b). CPW does a good job of reducing radiation; it has low-frequency dispersion and is preferred to microstrip for large spatially distributed circuits at frequencies above 20 GHz or so. There are disadvantages to it, including the increased area required and the need to use field straps (compared with microstrips) [22].

### 2.2.3 Coplanar strip and differential line

This planar transmission line structure is simple and consists of two conductors in the same plane above the dielectric substrate. When one of the conductors is grounded, this form is called coplanar stripline or coplanar strip (CPS). CPS is used as an area-effective variation of CPW in this configuration. If neither conductor is grounded and the line is operated, the

interconnection is called a differential line. A differential line is commonly used in high-speed optical networks with RFICs, and essential networks [22]. Both types have nearly similar electrical properties, with variations from communicating with other metallic structures such as ground planes. The cross-section of the coplanar strip and differential line is shown in Figure 2.2(c).

#### 2.2.4 Stripline

Stripline is a planar transmission line that is well suited for integrated microwave circuitry, miniaturization, and photolithographic manufacture [21]. The geometry of the stripline is shown in Figure 2.2(d). A thin conducting strip is centered between the two conducting ground planes, and the region between the ground planes is filled with a dielectric material. Stripline is typically built on a grounded dielectric substrate by etching the center conductor and then covering it with another grounded substrate [20]. In comparison with the microstrip line, the stripline manufacturing process is complicated because it requires multiple layers to support the embedded trace between two ground planes [22]. The selection of the transmission line depends on the need of the design [23].

#### 2.2.5 Embedded differential line

This simple transmission structure shown in Figure 2.2(e), is created by having only two conductors embedded in a substrate with no unique ground plane. It follows the same manufacturing procedure as stripline, except in embedded differential line, there are two conductors. This structure is incidental to the potential presence of ground planes, and preferably these should not impact the field pattern [21]. In multilayer boards, this trace architecture is more convenient and has less attenuation and radiation than in microstrips at higher frequencies [24].

### 2.3 Microwave technology in material detection

With industrial advancement, the modern industry depends on data obtained from an immense number of sensors in today's date. These sensors not only need to display sensitivity, selectivity, and high resolution in their service, but they should also be able to withstand environments that are harsh, inaccessible, and dangerous. Microwave technology can be easily

### 2.3. Microwave technology in material detection

implemented in sensing, and monitoring applications in unpleasant environments [25]. Microwave devices have recently shown significant efficiency in detecting and observing solid, liquid, and gaseous materials [26–28]. These devices have gained quite a popularity because of real time and highly accurate sensing.

The operating principle of material sensing in microwave technology utilizes the electromagnetic wave interaction between an input signal and the material in the sensors local environment, which translates information into a quantifiable electric signal [29]. This information can be used to characterize the material, allowing better processing and decision making of the information [30]. In this case, the dielectric properties of the materials play a vital role because of their unique characteristics. Coaxial probes, waveguides, dielectric resonators, and planar microstrip resonators are the microwave sensors in use, each following the general working theory of translating the dielectric properties (permittivity and conductivity) of material into factors of impedance and scattering, to be analyzed by readout circuitry [25, 31, 32].

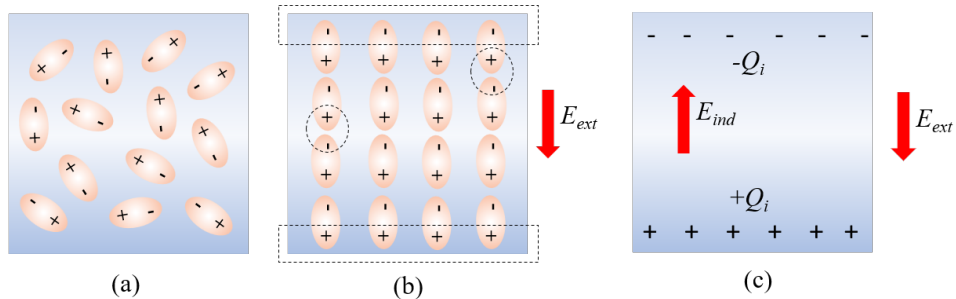


Figure 2.3: A dielectric with polar molecule: (a) in the absence of an external electric field  $E_{ext}$ , (b) in the presence of an external electric field  $E_{ext}$  and (c) the induced electric field  $E_{ind}$  inside the dielectric produced by the induced surface charge  $Q_i$ . Copyright © 2018 Rice University. All rights reserved [33].

A material is categorized as “dielectric” if it can store energy while an external electric field is applied. When a DC voltage source is applied across a parallel plate capacitor, more charge is stored if there is a dielectric material compared to no material (vacuum) in between the plates. The dielectric material between the plates increases the capacitor’s energy storage capacity by neutralizing the electrode charges, which would usually contribute to the

external field [33]. The effect of dielectric will be understood by gazing at its behavior at the molecular level. In the absence of any external electric field  $E_{ext}$ , the electrical dipoles of the molecules are randomly oriented, as shown in Figure 2.3(a). When the dielectric material is placed in an external electric field, the dipoles align with the external field, as shown in Figure 2.3(b). Opposite charges on neighboring dipoles neutralize each other within the dielectric volume, so there is no net charge within the dielectric volume [33]. This, however, is not the case very close to the upper and lower surfaces that border the dielectric (rectangular dash lines in Figure 2.3(b)), where the alignment produces a net charge. The induced surface charges ( $+Q_i$  and  $-Q_i$ ) produce an additional electric field  $E_{ind}$  which opposes the external field shown in Figure 2.3(c) [33].

The ability of a material to resist the electric field is called the permittivity of that material. The permittivity of free space is the resistance offered by the vacuum between two conducting plates. Dielectric constant or relative permittivity indicates how easily a material can become polarized by the imposition of an electric field on an insulator. Relative permittivity is expressed as the ratio of a substance's permittivity to the permittivity of free space or vacuum.

$$\epsilon_r = \frac{\epsilon}{\epsilon_o} \quad (2.1)$$

Where  $\epsilon_r$  refers to the relative permittivity and  $\epsilon$  is the permittivity of the substance (F/m) and  $\epsilon_o$  is the permittivity of the vacuum or free space ( $8.85 \times 10^{-12}$  F/m). So,  $\epsilon_r > 1$  indicates that a material can store more electric energy in a volume that can be stored in a vacuum.

In general, permittivity is a complex number where the real part describes the energy storage and the imaginary part describes energy dissipation between the electromagnetic field and the material. Energy storage represents the lossless component of energy exchange between the field and the material, and energy dissipation occurs when electromagnetic energy is consumed by the material [34]. The complex permittivity can be expressed as,

$$\epsilon_r = \epsilon' - j\epsilon'' \quad (2.2)$$

Where the real part ( $\epsilon'$ ) defines the dielectric constant and the imaginary part ( $\epsilon''$ ) accounts for the loss in the medium. Dielectric material losses are primarily caused by dielectric damping ( $\omega\epsilon''$ ) and conduction loss ( $\sigma$ ). A related quantity of the interest is loss tangent, which can be expressed as,

$$\tan\delta = \frac{\omega\epsilon'' + \sigma}{\omega\epsilon'} \quad (2.3)$$

Where  $\omega\epsilon'' + \sigma$  is accounted for total effective conductivity. The term loss tangent ( $\tan\delta$ ) is also called by terms such as tangent loss, dissipation factor, or loss actor.

Materials are usually characterized by these two properties (dielectric constant and loss tangent), which are highly frequency dependent. Microwave sensor devices utilize these frequency-dependent dielectric properties to characterize the materials. Figure 2.4 quantitatively shows the behavior of dielectric properties as a function of frequency [34].

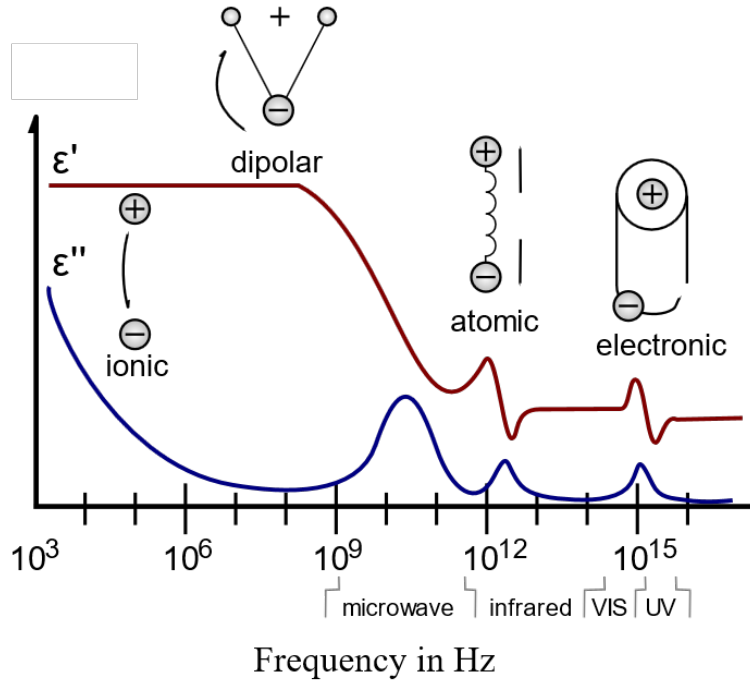


Figure 2.4: Complex dielectric permittivity spectrum over a range of frequencies where  $\epsilon'$  and  $\epsilon''$  denote the real and imaginary part, respectively. All rights reserved [35].

## 2.4 Different measurement techniques in microwave technology

The measurement techniques involve measuring the scattering parameters (S-parameters) using a vector network analyzer (VNA). The particular method used depends on the frequency range of interest and the type of target material. There are different measurement techniques available in microwave technology. Four significant methods of material detection in microwave technology will be discussed here.

### 2.4.1 Transmission/reflection (TR) line method

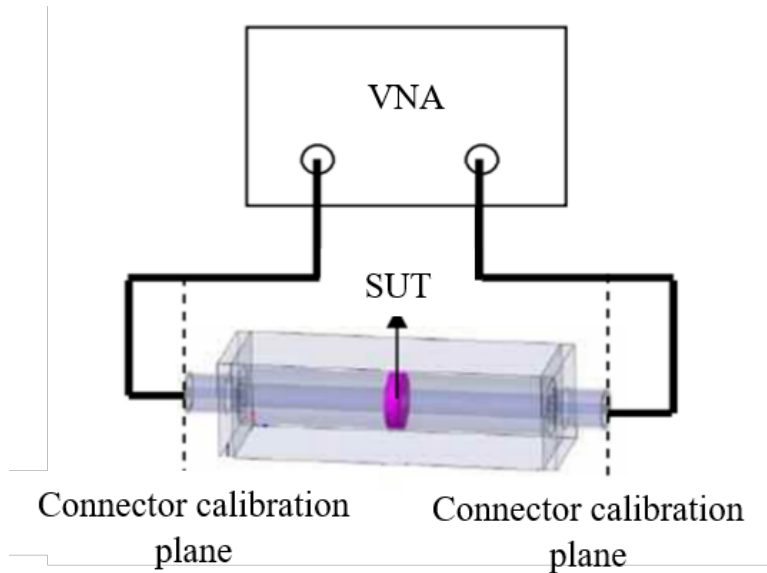


Figure 2.5: Measurement using TR method with a waveguide. All rights reserved [36].

In a transmission/reflection (TR) line method, the sample material is placed inside a portion of an enclosed transmission line. The line is typically a section of the rectangular waveguide or coaxial line. The VNA connected to the ports of the transmission line measures the S-parameters and records both the reflected ( $S_{11}$ ) and transmitted signal ( $S_{21}$ ). This method requires sample preparation (machining) so that the sample can fit tightly into the

waveguide or coaxial line. Figure 2.5 shows a typical measurement using TR method with a waveguide.

Calibration of the VNA must be taken out before making the measurement. After the calibration of the VNA, the prepared sample is placed in a sample holder. To reduce the uncertainty of the measurement caused by air gaps, the sample must be tightly fit in the sample holder. This method is used widely for the extraction of complex permittivity of materials. For instance, Costa *et al.* utilized this technique for electromagnetic characterization of materials because of wider bandwidth, but he also mentioned the sample preparation complexity [37]. On the other hand, Maleki *et al.* used the transmission line method to characterize the ferrite materials due to easy implementation and no requirement to measure the phase [38].

This technique benefits to measure samples with medium to high loss [36, 39, 40]. The disadvantage of this method is the limited measurement accuracy due to air-gap effects. It also limits the accuracy when the length of the sample is the multiple of one-half wavelength in the material [36].

#### 2.4.2 Open-ended coaxial probe method

The open-ended coaxial probe method is widely used as a non-destructive testing method. It is a modification of the transmission line method. This technique calculates the dielectric properties from the phase and amplitude of the reflected signal at the end of an open-ended coaxial line inserted into a sample to be measured [41]. The main component of this method is the high-temperature probe, which includes a circular flange with an aperture in the center. The properties of the sample material are measured by immersing the probe into a liquid or touching a flat surface of a solid. The fields at the end of the probe fringe into the substance and change when they come into contact with the sample material. The reflection coefficient is measured using a VNA. The setup for this type of measurement is shown in Figure 2.6. This technique is best suited for liquids, and semi-liquids [42].

Calibration at the tip of the probe must be performed before taking the measurement. The calibration corrects the directivity, tracking, and the source match that can be presented in the reflection measurement in the VNA [42]. The standard calibration procedure requires a three-fold (open, short and match) calibration [36]. The three known standards are air, a short circuit, and distillate and de-ionized water [42]. As a calibration norm, the referenced liquid is used and must be a liquid with "known" dielectric properties. The reference liquids are commonly selected as water, saline, and methanol. To eliminate the measurement's systematic errors,

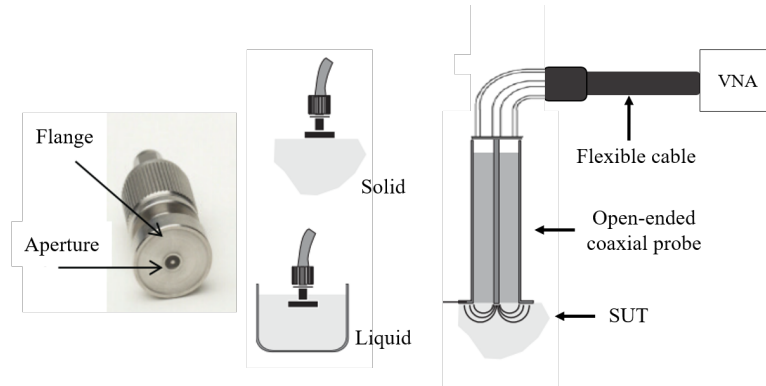


Figure 2.6: Experimental setup of an open-ended coaxial probe method. All rights reserved [36, 42].

the difference between the predicted and actual values is used. There are additional sources of error (such as cable stability, air gaps and sample thickness) even after calibrating the probe that can impact the probe and the measurement precision [42]. One needs to be very careful about cable stability and air gap before taking the measurement.

The open-ended coaxial probe method is prevalent because it allows flexibility and permittivity measurements at high temperatures. Santos *et al.* utilized this technique for permittivity measurements of liquid at high temperatures [43]. The open-ended coaxial probe technique is used to measure snow water content in [44] by Mavrovic *et al.* One of the benefits of this procedure is, after calibration, the dielectric properties of a large number of samples can be measured within a very short time. This technique can be utilized to measure the dielectric properties over a wide range of frequencies. For instance, the effect of different measurement probe on tissue contact pressure was monitored in a wide frequency range from 0.5 to 2.5 GHz in [45]. While using this technique, cautions must be exercised because errors are introduced at very low frequencies and very high frequencies, as well as with low dielectric constant and loss factor values [41]. Limited accuracy under certain conditions is a drawback of the coaxial probe system compared with the other methods such as transmission line, free space, or resonant [42].

### 2.4.3 Free space method

Free space techniques use antennas concentrating microwave energy on or through a sheet of material or slab. As the sample is never touched or contacted, high-temperature measurements are simple to perform in free space. It generally operates in wideband frequencies [42]. Besides, this can easily be used for continuous monitoring and control in industrial applications. For instance, Kraszewski *et al.* presented various aspects of measuring and continuous monitoring of moisture content in solids and liquids using free space technique [46].

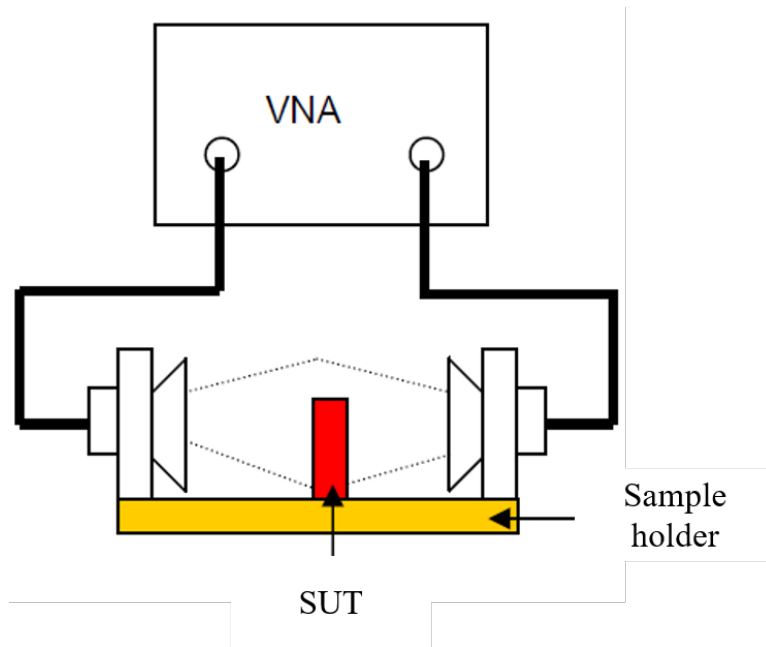


Figure 2.7: Measurement of sample under test using free space method. All rights reserved [36].

In a free-space technique, the sample is placed between a transmitting antenna and a receiving antenna, and the attenuation and phase shift of the signal is measured using a VNA, as shown in Figure 2.7. The measurement requires the sample to be large and flat [42]. Initially, by positioning the empty sample holder halfway between the two antennas, the s-parameters of an empty sample holder is determined. The sample is then placed between the antennas on the sample holder, and the s-parameter measurement is

again performed. The VNA's de-embedding function is used to cancel the sample holder's effect, and only the s-parameter of the sample can be calculated [36]. By utilizing this method, both the reflection and transmission coefficient of the s-parameters can be determined.

Prior to measurements, calibration of the network analyzer is mandatory. It is not easy to calibrate the network analyzer for free space as they are connector-less. Moreover, there are a variety of methods of calibration which can be used, such as through-reflect-line (TRL), through-reflect-match (TRM), and the line-reflect-line (LRL) [36]. However, The LRL calibration method will generate the highest level of calibration [36].

This measurement technique benefits the characterization of materials in high temperature, and hostile environment [47–51]. The free space method can also be used over a wide range of frequencies. Hakansson *et al.* utilizes this technique to measure the dielectric properties of polymerized films on synthetic textile substrates over a wide range of frequency from 1-18 GHz [52]. On the contrary, Trabelsi *et al.* accounted for multiple reflections, mismatches, and diffraction effects at the edges of the sample, which are the common drawbacks of this method [41]. Special attention must be paid to the choice of the radiating elements, the sample holder's configuration, and the sample geometry and position between the two radiating elements to improve the measurement accuracy [41].

### 2.4.4 Resonant method

The most accurate methods of obtaining the dielectric properties of materials are resonant methods because the resonant cavities are high quality factor (Q) structures that resonate at specific frequencies [42]. The resonant frequency and the Q-factor of the cavity are influenced by a piece of sample material inserted into the cavity. The complex permittivity of the material can be determined from these parameters at a single frequency.

Perturbation method and low loss measurement method are the two types of resonant measurement methods which are widely used [36]. Perturbation methods are suitable for medium to high loss material measurement whereas, and the low loss measurement method is a measurement of low loss materials using a larger sample [36, 53]. In Figure 2.8, a typical setup of the resonant method is shown where the perturbation method is utilized especially using a transverse magnetic (TM) cavity geometry to determine the dielectric properties of a thin rod. Initially, the measurement of an empty cavity is performed by measuring the resonant frequency and Q-factor. The second step is to place the sample thin rod along the center of the cavity

and record the new resonant frequency and the Q-factor in the VNA. With the sample in the cavity, any field shifts can result in the measured resonant frequency or Q-factor changing. Using the frequency, volume, and Q-factor, the sample's dielectric properties can then be computed [36].

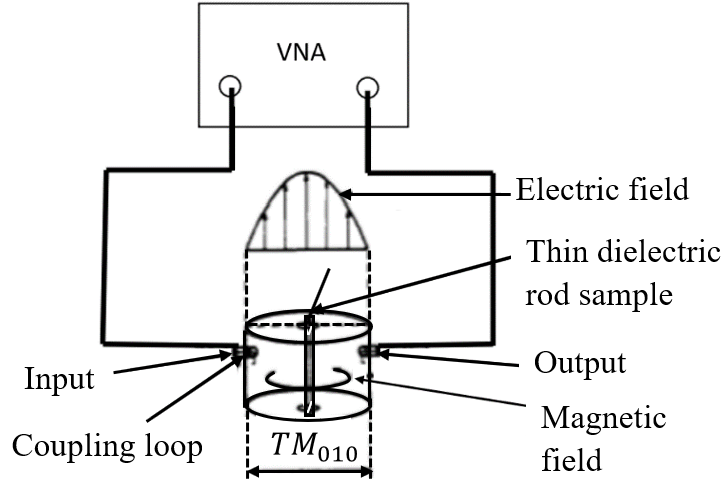


Figure 2.8: Measurement of a thin rod using resonant method. All rights reserved [36].

Resonant-based method is very popular for obtaining complex dielectric properties of materials such as permittivity due to its non-contact, portable, label-free sensing, and highly accurate measurement. Saeed *et al.* presented the use of substrate integrated waveguide cavity resonators to accurately characterize the material properties due to the attractive features such as high sensitivity and high Q-factor [54]. In [55], Tian *et al.* proposed a microwave resonant cavity-based sensor for measuring the moisture content in wet granules. The variable moisture content in the cellulose granule impacts the resonant frequency and Q-factor differently. The frequency difference is utilized as a signature to identify the different moisture levels.

Among the discussed measurement techniques in this section, the resonant based technique uses less expensive devices [56]. Machining the samples to fit properly in the cavity is an essential part of the measurement since a limited air gap can cause an error in the measurement. Microstrip line

#### 2.4. *Different measurement techniques in microwave technology*

---

sensor can be utilized because it offers the advantages such as low-cost fabrication, portability, robustness, non-contact, small sample size, and ease of integration with microfluidic chips [54, 57–62].

## Chapter 3

# Planar microstrip resonator, tuning mechanisms and microwave spectroscopy

This chapter aims to address the operating concept of a planar microstrip resonator and explore the wide variety of versatility in design. It is accompanied by a detailed discussion of various ways of tuning the resonant frequency used in the past and particular attention given to tuning based on microfluidics. An inquiry into the advantages of microwave spectroscopy in material detection has been described and provided in this chapter.

### 3.1 Planar Microstrip Resonator

Planar microstrip resonator is one of a kind of microstrip transmission lines that is characterized by a resonant frequency ( $\omega_o$ ). This frequency gives a rate of periodic exchange of electric and magnetic energy in the system. Among the other transmission lines discussed in section 2.2, in engineering, microstrip-based technology is well known to transmit signals in the microwave regime, and this is mainly due to the compact nature of the resonant microstrip circuits [63]. Planar microstrip resonators have gained quite popularity in different industries like bio-medical, healthcare, pharmaceuticals, food processing, agriculture, and communication due to its easy fabrication, non-contact measurement, real-time response, robust and high sensitivity [57–62].

#### 3.1.1 Theory of operation

Microstrips are planar transmission lines that consist of a conducting strip and a ground plane separated by a dielectric. In a transmission line, inductance ( $L$ ), capacitance ( $C$ ), resistance ( $R$ ), and conductance ( $G$ ) are evenly distributed along the length of the line [20]. It is convenient to

### 3.1. Planar Microstrip Resonator

model small segments of a transmission line in terms of lumped elements, as presented in Figure 3.1. It helps to understand the model elements as a representation of physical phenomena occurring in the transmission. The inductance per unit length  $L'$  describes the inductance associated with the ground plane and the conductor. The capacitance per unit length  $C'$  originates from the immediate vicinity of the conducting layers. The resistance per unit length  $R'$  is the conductors' resistance, and the shunting conductance per unit length  $G'$  describes the losses in the dielectric layer.

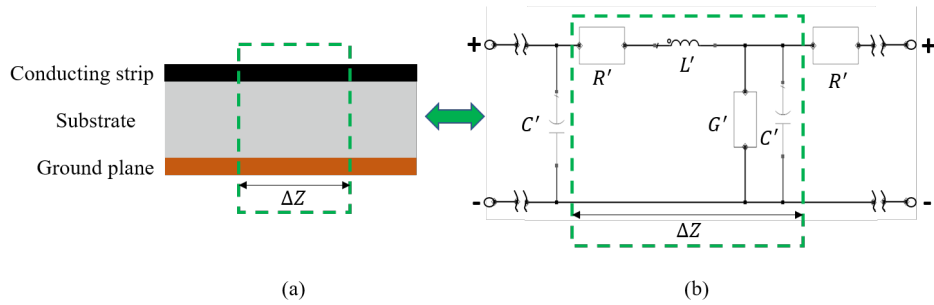


Figure 3.1: Lumped element representation of an infinitesimal part  $\Delta Z$  of a microstrip transmission line where (a) the actual microstrip and (b) the modelled microstrip. All rights reserved [63].

In practical applications, transmission lines exhibit low loss [64]. Using the Telegraphers equations [20], the wavelength ( $\lambda$ ) of the signals propagating along the transmission line can be determined by the equation,

$$\lambda = \frac{2\pi}{\omega\sqrt{L'C'}} \quad (3.1)$$

The phase velocity ( $v_{ph}$ ) is given by the formula [20],

$$v_{ph} = \frac{1}{\sqrt{L'C'}} \quad (3.2)$$

Two important quantities defining a transmission line are the characteristic impedance ( $Z_o$ ) and the propagation constant ( $\beta$ ), which can be defined as,

$$Z_o = \sqrt{\frac{L'}{C'}} \quad (3.3)$$

### 3.1. Planar Microstrip Resonator

$$\beta = k_o \sqrt{\epsilon_{eff}} \quad (3.4)$$

Where  $k_o$  is the propagation constant of the surrounding medium and  $\epsilon_{eff}$  is the effective permittivity of the surrounding medium.

When a time-varying electromagnetic signal travels through a transmission line, it generates electric and magnetic fields around it. The electromagnetic wave propagating on a microstrip line exists in two separate media: air (above the conducting trace) and substrate (between conducting strip and ground plane). The fields have to follow electromagnetic boundary conditions at the air-substrate interface. These boundary conditions contribute to components of the longitudinal electrical and magnetic field. The electric and magnetic field lines of the microstrip exist in the dielectric layer as well as in the surrounding medium, as shown in Figure 3.2. The effective permittivity of the microstrip is given approximately by [20],

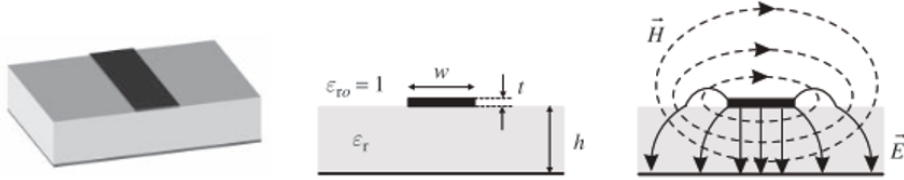


Figure 3.2: Electric (E-field) and magnetic (H-field) field distribution of a microstrip line. All rights reserved [65].

when  $(W/h \geq 1)$ ,

$$\epsilon_{eff} \approx \frac{\epsilon_r + 1}{2} + \frac{\epsilon_r - 1}{2} \left[ \frac{1}{\sqrt{1 + 12 \frac{h}{W}}} \right] \quad (3.5)$$

when  $(W/h < 1)$ ,

$$\epsilon_{eff} \approx \frac{\epsilon_r + 1}{2} + \frac{\epsilon_r - 1}{2} \left[ \frac{1}{\sqrt{1 + 12 \frac{h}{W}}} + 0.04 \left( 1 - \frac{W}{h} \right)^2 \right] \quad (3.6)$$

Where  $W$  is the width of the conducting strip and  $h$  is the thickness of the dielectric substrate. The characteristic impedance ( $Z_o$ ) of a microstrip line is determined by its geometry and the effective dielectric constant,

### 3.1. Planar Microstrip Resonator

---

when  $(W/h \geq 1)$ ,

$$Z_o \approx \frac{120\pi}{\sqrt{\epsilon_{eff}} [W/h + 1.393 + 0.667 \ln(W/h + 1.444)]} \Omega \quad (3.7)$$

when  $(W/h < 1)$ ,

$$Z_o \approx \frac{60}{\sqrt{\epsilon_{eff}}} \ln \left( \frac{8h}{W} + \frac{W}{4h} \right) \Omega \quad (3.8)$$

Such a transmission line functions as a resonator, the length of which is equal to half of its ground mode wavelength [20, 63, 65]. It is called a  $\lambda/2$  resonator. It is convenient and common practice to model a resonator as a parallel connection of a resistor, an inductor, and a capacitor in the vicinity of the resonant frequency [20, 66–69] as shown in Figure 3.3. The lumped element model of a transmission line resonant circuit is mainly based on the book by David Pozar [20], and article of Martin [67]. The input impedance  $Z_{in}$  ( $\Omega$ ) of this circuit is given by,

$$Z_{in} = \left( \frac{1}{R} + \frac{1}{i\omega L} + i\omega C \right)^{-1} \quad (3.9)$$

Where  $\omega$  is the frequency and  $i$  is the imaginary part. The complex input power  $P_{in}$  at the input of the resonators is given [68],

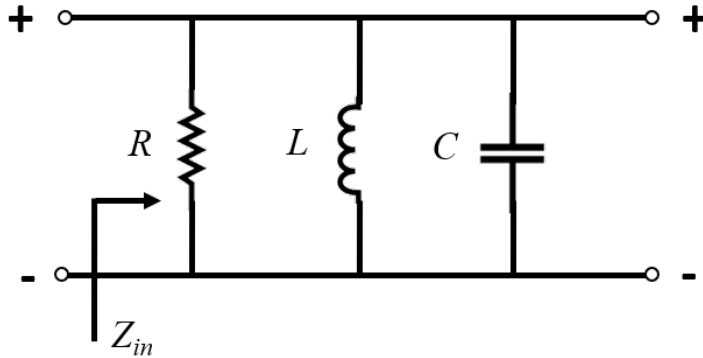


Figure 3.3: Lumped element model of a microstrip resonant circuit. All rights reserved [63].

### 3.1. Planar Microstrip Resonator

---

$$P_{in} = \frac{1}{2}|V|^2 \left( \frac{1}{R} + \frac{1}{i\omega L} + i\omega C \right)^{-1} \quad (3.10)$$

Where  $V$  is the voltage, the  $1/R$  term represents the energy ( $W_{loss}$ ) dissipated in the resistor. The complex terms define the stored magnetic ( $W_m$ ) and electric energy ( $W_e$ ) in the inductor and the capacitor, respectively. Resonance occurs when the planar resonant structure is able to transform the magnetic energy to electric energy and to fulfill this condition,  $W_m = W_e$  must hold. Therefore, the resonant frequency ( $\omega_o$ ) of the structure should be,

$$\omega_o = \frac{1}{\sqrt{LC}} \text{rad/s} \quad (3.11)$$

This is the frequency of the resonator's fundamental mode. The resonant frequency of the  $n^{th}$  mode of the resonator is given by,

$$\omega_n = n\omega_o = \frac{1}{\sqrt{L_n C}} \quad (3.12)$$

where [67],

$$L_n = L n^2 \quad (3.13)$$

and  $n \geq 1$  is an integral number. Then the internal quality factor of the resonant circuit is given by,

$$Q_{int} = \omega_n \frac{2W_m}{W_{loss}} = \frac{R}{\omega_n L_n} = \omega_n RC \quad (3.14)$$

#### 3.1.2 Resonant frequency and quality factor

Resonant frequency and quality factor are those parameters of a resonator that determines the performance of the resonator. Resonant amplitude is the maximum value of amplitude when the resonance occurs in a resonator circuit. It is the maximum value of oscillation at which the resonant occurs in a resonant system. In the previous section, the basic theory of calculating the resonant frequency and quality factor of a microstrip resonator is described as a lumped element model. One can also easily estimate the resonant frequency and Q-factor from the structural design, and this will be presented here.

#### Resonant frequency

Resonant frequency is the oscillation of a system at its natural or unforced resonance. Resonance occurs when a system can store and easily transfer energy between different storage modes, such as kinetic energy or potential energy. Most systems have one resonant frequency and multiple harmonic frequencies that get progressively lower in amplitude as they move away from the center. A system tends to oscillate at maximum amplitude at certain frequencies, known as the system's resonant frequency. Resonant frequencies are essential in both mechanical and electronic/electrical systems. Mechanical resonance can cause massive vibrations that can destroy objects. On the other hand, electrical/electronic resonance is generally used to tune a circuit. This may be parallel resonance used to maximize a signal one wants, to select a radio signal, or cause an oscillation. Series resonance may be used to absorb a specific signal. Combinations are used to filter signals selectively.

For passive resonators, the length of the microstrip line plays a critical role in determining the resonant frequency of the system. The resonators usually are designed with the half-wave resonator concept; thus, the resonant frequency can be estimated using the equation 3.15 [70].

$$f_r = \frac{c}{2l\sqrt{\epsilon_{eff}}}\text{Hz} \quad (3.15)$$

Where  $l$  is the total length of the resonator microstrip line (m),  $\epsilon_{eff}$  is the effective permittivity of the materials in the resonator ambient environment,  $c$  is the velocity of light (m/s) and  $f_r$  is the resonant frequency (Hz). Since the speed of the light is constant and effective permittivity varies slightly with the material, the resonant frequency mostly depends on the length of the resonator microstrip line. By varying the total length of the microstrip line, the resonant frequency can be altered. So, it can be said from the equation 3.15 that the higher the length of the microstrip line, the lower the resonant frequency of that resonator.

#### Quality factor

A parameter which is closely related to the finesse is the quality factor ( $Q$ ) of a resonator, which is a measure of the sharpness of the resonance [71]. For electronic circuits, the quality factor is defined as the ratio of the stored energy over the energy dissipated in one cycle. Therefore, an ideal resonator with no loss has an infinite quality factor [72]. The quality

### 3.1. Planar Microstrip Resonator

---

factor of a resonator can also be determined by the resonant frequency to bandwidth ratio. The following equation is utilized to find the Q-factor of a resonator.

$$Q = \frac{f_r}{\Delta f} = \frac{f_0}{f_{3dB}} \quad (3.16)$$

Where  $f_r$  is the resonant frequency and  $\Delta f$  is the resonant width, which is the bandwidth over which the power of vibration is greater than half power at the resonant frequency. Under this definition,  $Q$  is the reciprocal of fractional bandwidth. The Figure 3.4 clarifies the formula to calculate the Q-factor of a resonant circuit.

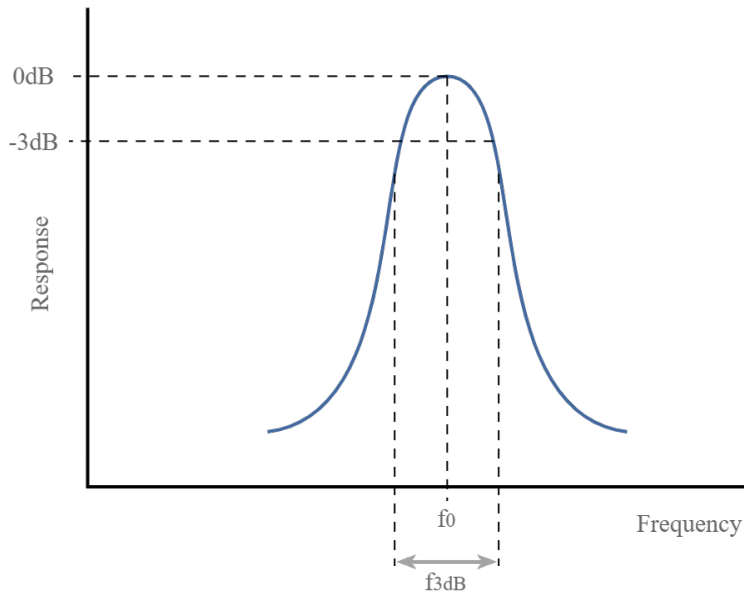


Figure 3.4: Quality Factor of a resonant circuit. Copyright © electronics-notes.com. All rights reserved [73].

When dealing with RF tuned circuits, there are many reasons why  $Q$  factor is important. Usually, a high value of  $Q$  is beneficial, but in some applications, a defined level of  $Q$  may be what is required. With increasing  $Q$  factor, the bandwidth of the tuned circuit is reduced. As the  $Q$  increases, the  $3dB$  bandwidth decreases and the overall response of the tuned circuit increases, and the losses decrease. So, the higher the resonator's quality factor, the better the performance of the oscillator [74]. In many instances,

a high  $Q$  factor is needed to ensure that the required degree of selectivity is achieved.

### 3.1.3 Split ring resonator

The split ring resonator (SRR) is merely a transmission line formed in a closed loop with a split. Resonator structures like the split ring resonator (SRR) are commonly used to shape metamaterials as building blocks [75–77]. The SRR structure was first introduced by Pendry in 1999 [78]. Metamaterial is an artificial material in which electromagnetic properties (permittivity,  $\epsilon$  and permeability,  $\mu$ ) can be controlled. This is important because it makes it possible for fields and waves to be controlled on a sub-wavelength scale. In particular composite media, electromagnetic waves interact with the inclusions, which produce electric and magnetic moments, affecting the macroscopic effective permittivity and permeability of the bulk composite medium. Since metamaterials can be synthesized by embedding artificially fabricated inclusions in a specified host medium, this provides the designer with an extensive collection of independent parameters such as properties of host materials, size, shape, and compositions of inclusions. All these design parameters play a significant role in getting the final result.

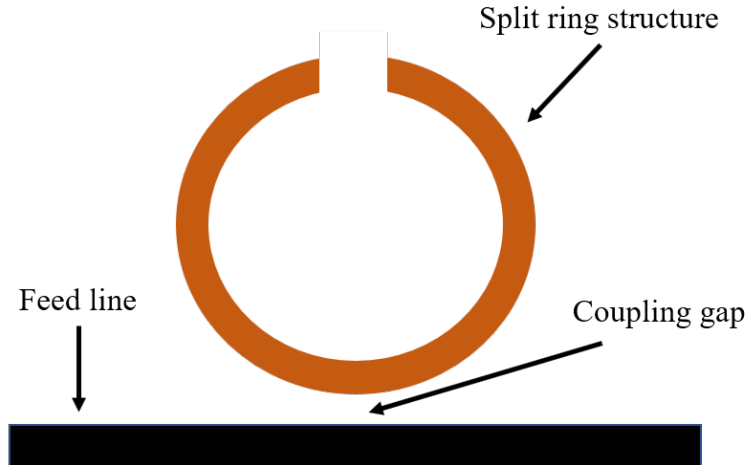


Figure 3.5: A simple split ring resonator structure coupled with feedline.

A simple split ring resonator structure is shown in Figure 3.5. The basic circuit consists of the feed lines, coupling gap, and the split ring struc-

### 3.1. Planar Microstrip Resonator

ture. Energy is coupled into and out of the resonator through feed lines and coupling gaps. The coupling gap plays a vital role in achieving a good resolution of the circuit. A larger coupling gap between the feedline and the ring structure is considered a loose coupling, which manifests the negligibly small capacitance of the coupling gap [79]. However, if the feedline is pushed closer to the resonator, the coupling becomes tight, and the gap capacitances are visible. This allows the circuit's resonant frequencies to deviate from the ring's intrinsic resonant frequencies [79]. Hence, designers need to consider the coupling gap effect based on the application while designing the structure.

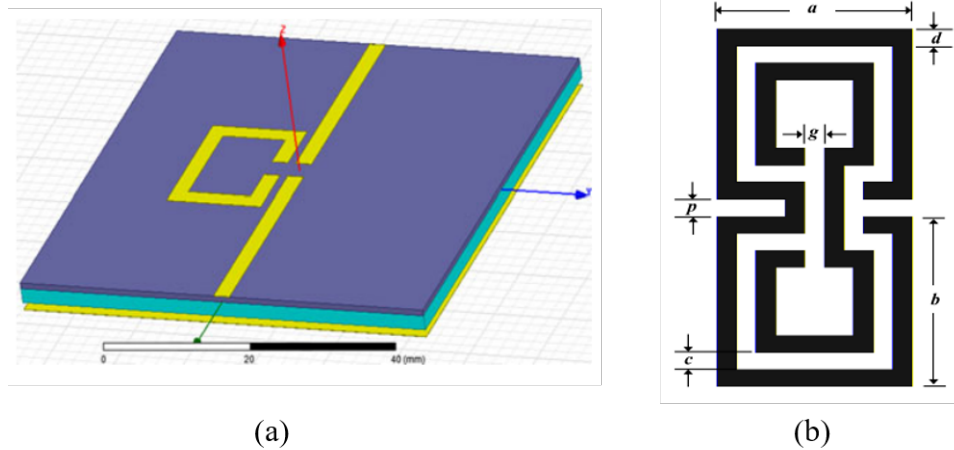


Figure 3.6: (a) Resonator sensor structure implemented in HFSS for the purpose of early detection breaches in pipeline coatings [57] and (b) open split ring resonator structure (OSRR) [80].

Different configurations of split ring resonators were designed to perform different applications. The basic configuration, which consists of a half wavelength, open ring microstrip structure in Figure 3.6(a) is reported in [57]. The ring resonator was coupled to the input-output signal ports using microstrip feed lines. The designed microwave resonance-based sensor was used for detecting the cause of defects in pipelines, which is mainly driven by coating failure. A double-ring resonator was proposed as the main component of getting real-time and hazard-free water quality monitoring in [81]. The strong capacitance between the two concentric rings helps the flow of current along SRR configuration. S.S. Karthaikeyan *et al.* [80] designed

### 3.1. Planar Microstrip Resonator

---

an open split ring resonator (OSRR) back in 2010, which has a geometry of given kind in the Figure 3.6(b). The OSRR and wire arrangement constructed the metamaterial cell. Scattering parameters determined the complex permittivity and permeability of the metamaterial cell. Dual-mode split ring resonator was also designed in [82] to eliminate relative humidity impact. One of the resonators resonates at 0.552 GHz, and another resonator resonates at 1.03 GHz, and the latter one was used to calibrate the potential measurement error.

There are different geometries of SRR used to realize artificial magnetic materials. In Figure 3.7, different geometries of SRR is shown to understand the wide range of design ideas. It can also be seen from the Figure that the split ring resonator is not just only confined to the circular shape; instead, rectangular shapes of the ring are also found in different investigations. So, based on the application, designers have the flexibility to play with different shapes and sizes of the resonators.

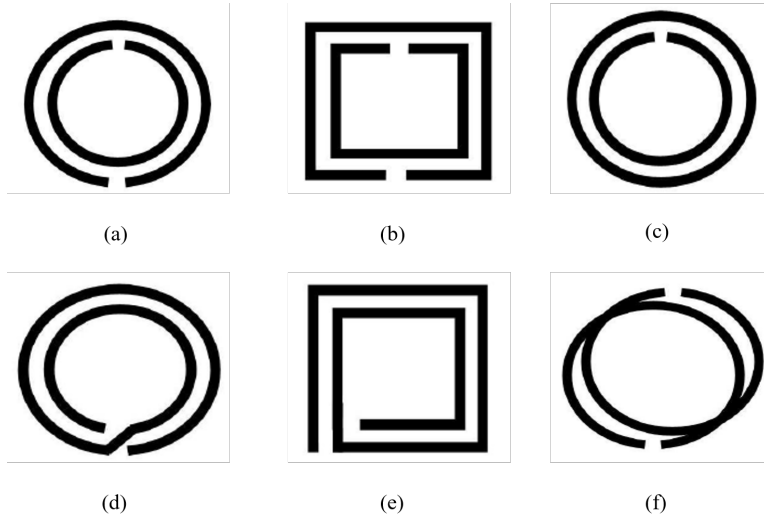


Figure 3.7: Some geometries of split ring resonator (SRR). (a) Double split ring resonator, (b) Double split square resonator, (c) Singly split ring resonator, (d) Two-turn spiral (circular) resonator, (e) Two-turn spiral (rectangular) resonator and (f) Modified ring resonator. Copyright © Ali Kabiri 2010. All rights reserved [83].

## 3.2 Tuning Mechanisms

The resonance of the constituent elements exhibits a narrowband frequency response in many electromagnetic devices, especially in metamaterial applications [84]. In this case, materials are characterized or monitored in one single resonant frequency. RF designers estimate this particular frequency based on the MUT's behavior and utilize the design parameters to design a compact resonant structure. This technique is beneficial in providing higher precision in measurement but limits the measurement to only one single frequency. In order to broaden the frequency coverage, a popular technique to resolve this issue is to add a tunable narrowband response. Several tuning methods have been suggested, and an analysis of these is provided according to their overarching operating mechanism in the following section.

### 3.2.1 External devices

In many different investigations earlier, it was proposed to incorporate external devices such as capacitors, varactors, and micro-electromechanical radio frequency systems (RF MEMS) into a resonator component to tune the frequency response [84]. These variable components are often loaded with the resonator structure, and by changing the values of the variable elements, the resonant frequency can be tuned [85, 86]. In Figure 3.8(a), a resonator structure is loaded with an external variable capacitor is presented. The variable capacitor element is placed in different positions such as the gap between two rings, the split of the outer ring and the split of the inner ring, and by changing the value of the capacitance, the change in the resonant frequency is observed [85].

Another way of tuning the resonant frequency is mounting varactor diodes across the gap of a resonator structure. The desired frequency tuning can be achieved by adjusting the bias voltage of the varactor diode [87, 89–92]. This technique normally allows a large range of frequency tunability. In [87], Nesimoglu *et al.* utilized this technique on an S-shaped resonator structure, where 28% tunability was achieved by using reverse-biased varactor diodes at a critical location on the structure, the structure is presented in Figure 3.8(b). Zhu *et al.* [92] proposed a varactor loaded split ring resonator antenna where the designed antenna's operating frequency was tuned from 365 MHz to 500 MHz by changing the bias voltage from 1 to 9 V. A relative frequency change of 37% was observed during this investigation. However, Biasing circuitries are introduced into the structure by the presence of varac-

### 3.2. Tuning Mechanisms

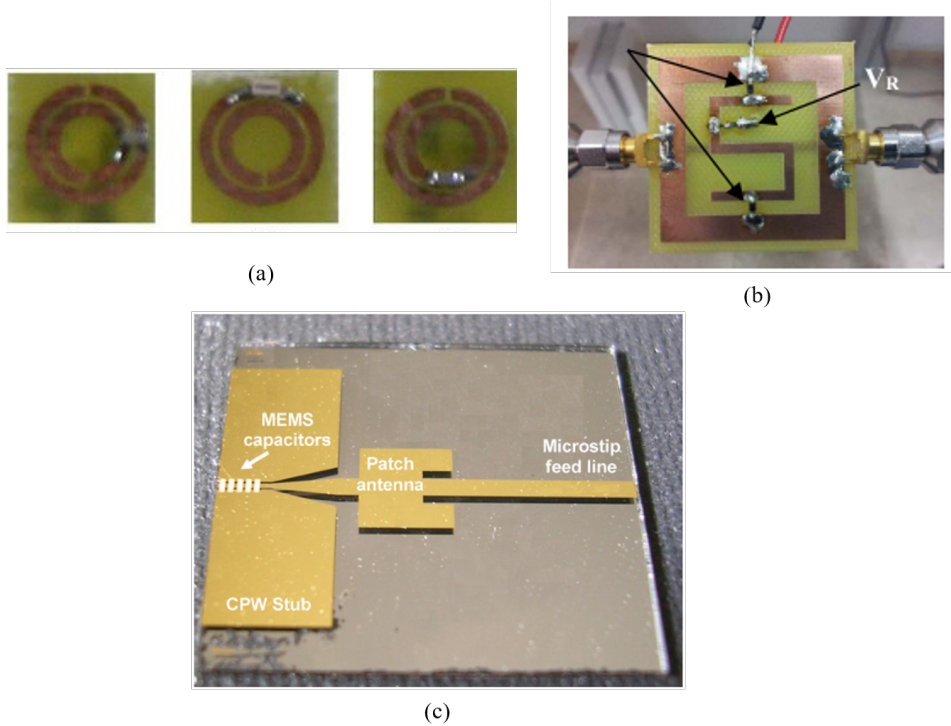


Figure 3.8: Tuning by the external devices. (a) SRR with capacitor loaded [85], (b) Varactor loaded S-shaped resonator [87] and (c) RF-MEMS loaded microstrip patch antenna [88]. Copyright © 2007 American Institute of Physics, 2007 and 2016 IEEE.

tors in the resonator, resulting in additional losses/reflections/coupling [84]. Besides, it will interfere with the RF signal and will restrict the resonator's efficiency. Furthermore, this also enhances the complexity and scalability limitations of manufacturing [84]. Ferroelectric varactors are found to maintain a relatively low  $Q$  and temperature-sensitive and can create distortion in high  $Q$ -tunable filters [93–95]. This makes the varactors not suitable for different environments.

Components of RF-MEMS were integrated with EM systems to achieve frequency tunability in many applications [88, 96–99]. As shown in Figure 3.8(c), Erdil *et al.* [88] presented a reconfigurable microstrip patch antenna integrated with RF-MEMS capacitors for tuning the resonant frequency. By changing the actuation voltage from 0 - 11.9 V, the antenna resonant fre-

quency can continuously be tuned from 16.05 GHz to 15.75 GHz. In [96], Bougye *et al.* proposed a combination of 4-pole bandstop filter and split ring resonator, which can digitally control the bandwidth due to frequency shift by the on-off state of the RF-MEMS switches. By moving a cantilever RF-MEMS bridge capacitor up or down, a metamaterial filter is electrostatically actuated as in [97], causing a high-frequency tunability. Although RF-MEMS switches provide very fast tuning speed, fabrication of the RF-MEMS is quite complex, especially while considering resonator arrays where a huge number of RF-MEMS will be required [84].

Other techniques were utilized for tuning the operating frequency, such as semiconductor switches, p-i-n diodes, and Yttrium iron garnet (YIG). Semiconductor switches cannot handle much power, and it generates a lot of distortion [100–102]. P-I-N diodes need biasing for achieving good linearity, and as a result, it consumes high power [101]. YIG (Yttrium iron garnet) enabled switches can maintain a very high Q and relatively low distortion. However, due to high current consumption and magnet requirements, it cannot be integrated into planar fashion. Therefore, YIG is not appropriate for low-cost portable solutions [101]. Due to the solid-solid contact in MEMS switches, it creates contact wear and heat generation, which result in a reliability issue [103–105].

#### 3.2.2 Microfluidic-based tuning

The appearance of microfluidics has led to the latest ongoing reputation of utilizing microfluidic innovation for reconfigurable RF components. Ordinarily, RF component tunability is found to use either mechanical rotation, solid-state and varactor diodes, or RF MEMS, which experience the ill effects of downsides of non-linearity, power losses, non-robustness, and fabrication complexity. The headway in microfluidics has as of late permitted researchers to defeat these disadvantages and execute RF devices. By the progress within the microfluidics fields, fluidic control can be utilized to acknowledge highly linear devices and fluids/liquids to flow in channels fit for dealing with high power RF inputs. Moreover, fluidic-based tuning dispenses with the plausibility of surface damage and can be utilized in flexible, wearable devices. Besides, liquid metal components are fit for holding their physical changes subsequent to expelling the activation power, killing the need for consistent actuation. Furthermore, it offers the simplicity of fabrication contrasted with other tuning mechanisms.

Table 3.1 shows a detailed analysis of different switching techniques available in microwave technology.

### 3.3. Review of Microfluidic Applications

Table 3.1: Comparison of different switching techniques

	Liquid metal	Semiconductor switch	YIG	MEMS
Temperature sensitivity	low	low	high	low
Tuning speed	ms	ns	ms	$\mu$ s
Biasing	no need	electric field	magnetic field	electric field
Operating frequency	unlimited	limited	limited	limited
Cost	low	high	high	high
Linearity	linear	non-linear	non-linear	linear
Maintaining Q-factor	possible	additional circuit	impossible	additional circuit
Planar	yes	yes	no	yes

### 3.3 Review of Microfluidic Applications

At current times, fluidic control for tuning microwave devices has pulled in much consideration attributable to the points of interest offered by fluidic control. The fluidic control can be divided into two major parts based on absorption and reflection switching techniques [106]. Both techniques have their merits and demerits. For high power applications, absorptive behavior is more important than the reflective switching technique since the reflective signal can adversely affect the circuit performance or lead to catastrophic failures [107]. So, for low power applications, conventional reflective MEMS switches are suitable.

Broadband absorption can be achieved by injecting liquid metal [110], or water [111]. In microwave and sub-mm region, water is a relatively lossy material with a complex dielectric constant, and it requires careful consideration to avoid losses. On the other hand, fluidic based tunable devices take part in the action and substitute the liquid elements with a type of liquid metal to ensure adjustability. Initially, mercury has been constrained to deformable body-wearable antennas [112], frequency selective surfaces, and metamaterials [113–115], since mercury is the only naturally occurring metal that exists as a liquid at room temperature. Nevertheless, mercury

### 3.3. Review of Microfluidic Applications

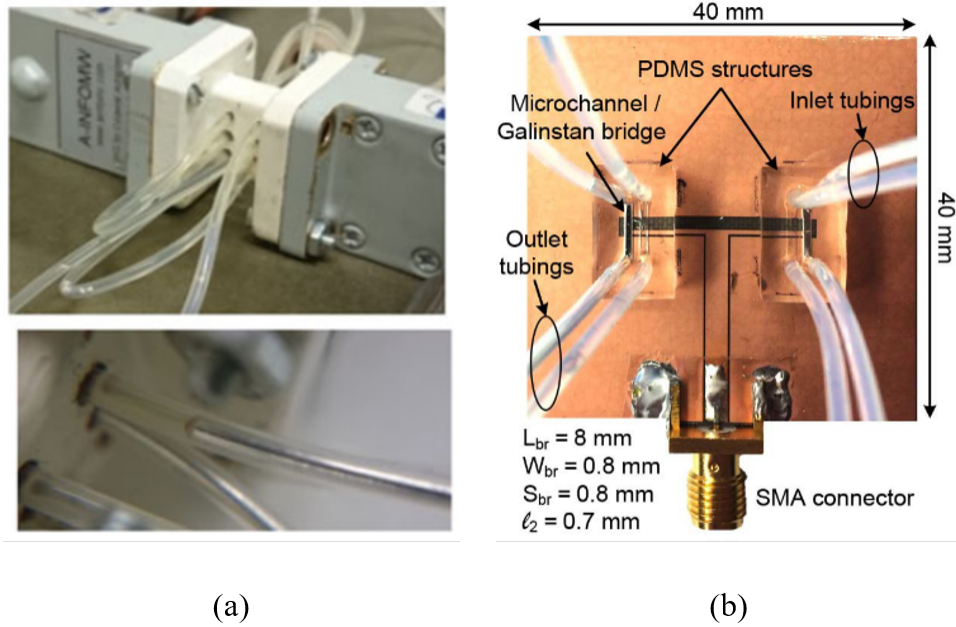


Figure 3.9: Microfluidic based tuning. (a) Implemented prototype of the microfluidic waveguide switch [108], (b) Reconfigurable CPW folded slot antenna [109]. Copyright © 2015 and 2017 IEEE.

was not favorable to improve the RF devices in later days due to its high toxicity. Accordingly, inferable from their high conductivity, non-toxicity, and liquid state at room temperature, commercially available liquid metal alloys, for example, Eutectic Gallium-Indium (EGaIn) and Galinstan (composition of Gallium, Indium and Tin) have pulled in much consideration for microfluidic-based configurability.

While some of the examples of such work include liquid metal as a switch to connect reactive loading elements to the circuit [108, 116, 117], liquid metal itself as a variable reactive load [109, 118], use of liquid metal to connect to short and open microstrip stubs [119]. In Figure 3.9(a), implemented prototype of the microfluidic waveguide switch is shown, which is developed by Vahabisani *et al.* [108]. A slot antenna with a configurable resonant frequency by changing the length of a liquid metal bridge over the waveguide structure is also reported in [109] and the implemented prototype is shown in Figure 3.9(b). This approach did not enable continuous

frequency tuning but operated in multiple fixed modes based on the complete filling or emptying of the liquid metal channels. Frequency tuning over such a wide range can be utilized for frequency selective surfaces, blocking or transmitting signals in a controllable way [120], or developing tunable antennas [112]. A configurable microstrip open stub resonator was developed via liquid metal to change the filter frequency [121]. It is worth mentioning that, unlike the solid-state and most of the MEMS switches that consume power all the time, the liquid metal could retain its position without the need to apply DC power. This could reduce DC power utilization, particularly for the applications that the switch requires to remain in one state for quite a while.

#### 3.3.1 Challenges and limitations of microfluidic based tuning

Microfluidic control over tuning a microwave circuit has its advantages and disadvantages depending on the purpose of use. Since there are challenges of employing fluidic control to achieve tunability, the challenges need to be addressed to better respond to the circuit. The choice of liquid metal is one of the very important selection considering its properties and microwave performance. Upon selection, it is vital to understand its behavior towards the employed fluidic channel and choose a suitable injection method. Below are the three most significant challenges and limitations discussed to ease the use of liquid metal.

##### **Liquid selection:**

Table 3.2 shows the comparison among the physical properties of the available liquid metals with copper [122]. The only naturally available liquid metal mercury has a very low melting temperature. Due to highly toxic and hazardous to the health and environment, the use of mercury has been compromised. On that note, low melting temperature and non-toxic behavior of liquid metal alloy, EGaIn and Galinstan make its place to substitute mercury. These liquid metal alloys not only avail high conductivity but also stays liquid at room temperatures. In this thesis, Galinstan was used as liquid metal to incorporate the fluidic based tuning of the resonant frequency.

##### **Skin and residues:**

EGaIn and Galinstan also avail higher surface tension, which means it shows a high tendency to oxidize with oxygen whenever it comes in con-

### 3.3. Review of Microfluidic Applications

Table 3.2: Comparison of physical properties of Copper, Galinstan, EGaIn and Mercury © 2015 IEEE

Properties	Copper	Galinstan	EGaIn	Mercury
Melting point (°C)	1085	-19	15.5	-38.8
Boiling point (°C)	2562	>1300	2000	357
Density ( $kg/m^3$ )	8960	6440	6280	1353
DC conductivity (S/m)	$5.96 \times 10^7$	$3.45 \times 10^6$	$3.4 \times 10^6$	$1.0 \times 10^6$
Viscosity (Pa.S)	-	$2.4 \times 10^{-3}$	$2.0 \times 10^{-3}$	$1.5 \times 10^{-3}$
Surface tension (N/m)	-	0.718	0.624	0.487

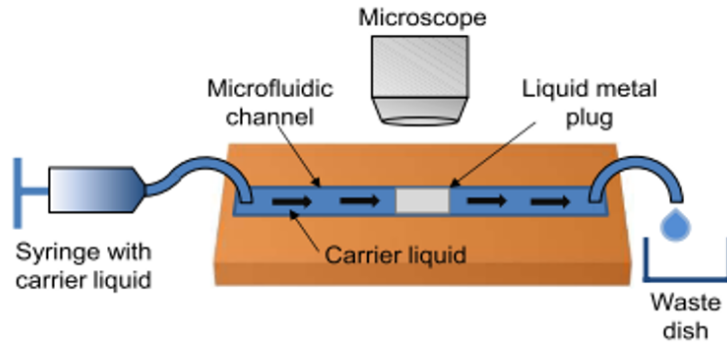


Figure 3.10: A liquid metal plug sandwiched between the carrier fluid inside the microfluidic channel [123]. Copyright © 2014 IEEE.

tact, bringing about the arrangement of a thin oxide film on the metal surface [123]. The surface oxide layer made it regularly stick to the walls of the tubing and the microchannel. While flowing liquid metal inside the microchannel, this tends to leave skin residue and affect the device's performance. Some carrier liquid is needed to eliminate the problem, which would clear the residue of liquid metal and can work as a potential barrier to liquid metal oxidation. The RF property, viscosity, and toxicity of the carrier liquid plays a vital role and have been studied [123, 124]. A strong acid or base used as carrier liquid helps to remove the skin layer of the oxide [125]. However, the use of such strong chemicals for many practical applications is undesirable. A safer alternative approach is to use either naphthenic base

### 3.3. Review of Microfluidic Applications

---

oil, Hydrocal 2400 [123, 126], and a low loss Teflon solution [127, 128]. In [123], the proper orientation of liquid metal inside the microchannel followed by the carrier liquid in both sides of the liquid metal is illustrated and shown here in Figure 3.10. In this thesis, Hydrocal 2400 was used as a lubricator to eliminate skin residue of the oxide layer, and it also benefits as a potential barrier to liquid metal oxidation.

#### **Injection control:**

After the proper choice of liquid metal and the carrier liquid, it comes to pushing the liquid metal inside the microchannel. It is a straightforward process but needs proper implementation following the steps. There are multiple ways of injecting liquid metal through a microchannel. One way is to use a syringe and injecting the liquid metal inside the microchannel by controlling the pressure using hands. Initially, both the channel and tube need to be lubricated using the carrier liquid. The syringe should then be filled with the desired amount of liquid metal and pushed through the tube inside the channel. Once the channel is filled with liquid metal, more carrier fluid should be pushed inside the tube. To encapsulate the liquid metal, one can gently push or withdraw the carrier liquid by pushing in and out from the inlet or outlet side.



(a)



(b)

Figure 3.11: (a) A mm syringe and (b) 11 Pico Plus Elite programmable syringe to control the liquid flow [129]. Copyright © 2020 Darwin Microfluidics.

Another way is to ensure automatic injection and positional control over the liquid metal inside the microchannel is to integrate the micro-pump [112] or electrochemical actuation [130]. In this thesis, liquid metal was pushed through the microchannel using an 11 Pico Plus Elite programmable syringe automated pump from Harvard instruments. The standard infuse/withdraw method controlled the flow rate of liquid metal into the microchannel. In Figure 3.11(a), a mm syringe is shown which can be used manually to control the flow of the liquid metal, and in Figure 3.11(b), an automated programmable syringe from Harvard Instruments is shown to control the liquid metal flow.

#### 3.3.2 Microfluidic Channel

Microfluidic channels are utilized to manipulate and provide a closed environment for the liquid sample exposed to electromagnetic fields. There are different ways to implement microfluidic channels in microwave devices. In different investigations, PDMS (Polydimethylsiloxane) is used to create the microfluidic channel to flow different liquids. The microfluidics community has embraced PDMS for many reasons. It allows simple, planar systems to be replicated and produced easily. Complex 3D structures and microchannel networks can be fabricated easily in PDMS by multilayer prototyping approaches. A 3D printed microchannel embedded in PDMS is reported in [109] and [131] to realize a switchable dual-band slot antenna and reconfigurable CPW folded antenna, respectively. Fluid samples are injected to the PDMS microchannel aligned with the resonator for dielectric characterization of the microfluidic samples [132]. Few more examples of recent work include open stub resonator filter using pressure-responsive fluid inside PDMS [121], PDMS structure including the microchannel is bonded to a filter to ensure reconfigurability of the SIW (substrate integrated waveguide) cavity filter [117], PDMS structure including one microchannel was employed to place the MUT to implement wideband microwave interferometry sensor [133]. Since PDMS does not break but bend, researchers found it more useful compared to glass. There are always cautions trying things with glass as it is sharp and has disposal problems. Experts say that although the material is attractive for quickly testing the fluidics of the new devices, it has problems since there is no perfect material. In Figure 3.12(a), a PDMS microchannel with the embedded tube is shown to transfer the liquid metal EGaIn.

The fact that PDMS absorbs molecules is not a new discovery. The issue with the PDMS includes absorption of organic solvents and small molecules,

### 3.3. Review of Microfluidic Applications

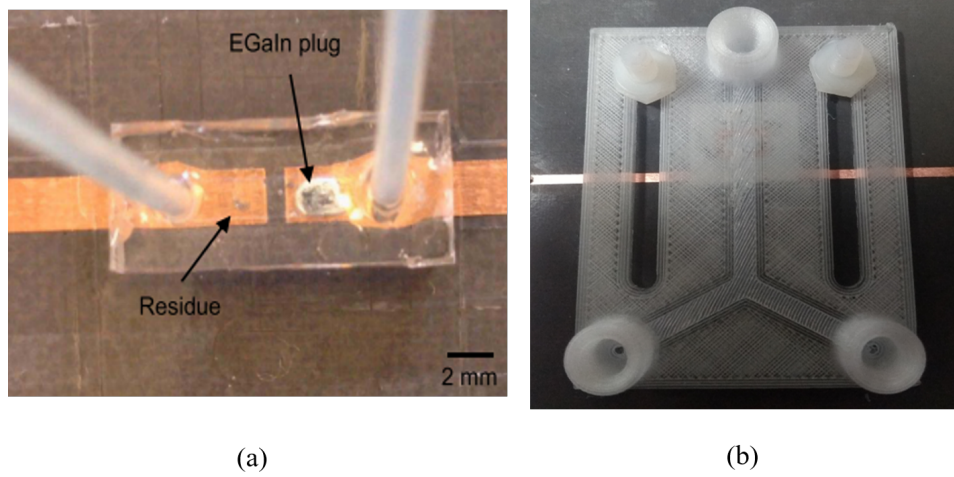


Figure 3.12: (a) EGAIn plug inside a PDMS [123] and (b) 3D printed structure utilized as a microfluidic channel [70]. Copyright © 2014 and 2018 IEEE.

its inherent hydrophobicity, and evaporation of water [134]. In some applications, it is considered useful that PDMS absorbs the solvent and evaporates water [134]. Since microwave devices are very much sensitive, even a small alternation of the electromagnetic field can widely impact the device's performance. PDMS is pressure-sensitive, making it hard to fabricate a large channel using PDMS [134]. While flowing fluids, it needs constant pressure throughout the channel. Pressure inequalities can create bending of the PDMS, which particularly can alter the response of the device. There is always a risk of leakage due to channel-resonator bonding defects [135]. A new approach not to substitute PDMS but can alternatively use for fluid movement is 3D printing to overcome this problem. 3D printing is an emerging technology and can be useful to be utilized as a microfluidic channel. In [70] and [136], a 3D printed microfluidic channel embedded with planar microwave resonator was realized for RFID and liquid detection. In Figure 3.12(b), a 3D printed microchannel is presented [70]. In this thesis, a fluidic channel was 3D printed and utilized to guide the fluids, allowing low cost, non-contact, sensitive, and easily reusable properties.

### 3.4 Microwave Spectroscopy

Microwave spectroscopy is the determination of those frequencies of the microwave spectrum that are selectively absorbed by certain materials, providing information about the atomic, molecular, and crystalline structure. This way, the complex dielectric properties (loss tangent and relative permittivity) of materials can be observed in a frequency spectrum. Since loss tangent and relative permittivity are a function of frequency, the spectrum brings out a clear picture of the material's dielectric properties over a wide range of frequency.

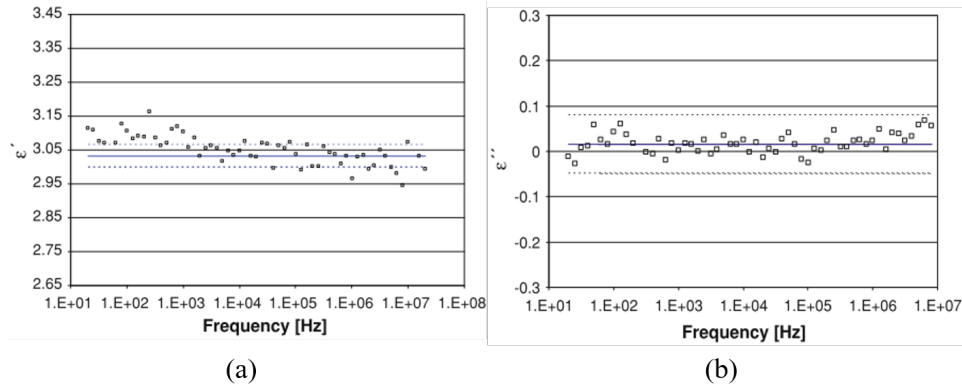


Figure 3.13: Dielectric spectra of soybean oil at 25°C temperature over a broadband where (a) real part and (b) imaginary part. Copyright © Springer-Verlag London Limited 2011. All rights reserved [137].

In microwave technology, dielectric property measurement can be broadly identified in two different methods such as resonant and non-resonant. Resonant methods are more reliable, accurate, and appropriate for characterizing low-loss materials [138]. They can only provide measurement results in one single frequency, or a number of discrete frequencies [139]. The non-resonant methods such as the TR line method, coaxial probe method, and free space method, can enable material characterization over broadband; however, they are less accurate than resonant methods [138]. Calibration errors, connector non-reproducibility limit the accuracy of TR line methods, and mismatching of impedance [140]. In [141], Narayanan *et al.* proposed permittivity measurement of the dielectric substrate over broadband utilizing microstrip transmission line method. The real (Figure 3.13a) and imaginary (Figure

3.13b) part of a dielectric spectra of soybean oil at 25°C temperature is shown in Figure 3.13 where author utilized the coaxial probe method to measure the complex dielectric property of soybean oil in different temperature setting [137]. The free space method limits the measurement of dielectric properties of materials that are large and flat. It is best for flat sheets, powders and high temperature measurements [36, 41, 142].

### Resonant based spectroscopy

In case of a single frequency resonator sensor, the resonant frequency of the dominant mode highly depends on the material properties such that a minute change in the liquid can be monitored. However, in that case, the sensors do not provide any information on the material behavior across the frequency and only act on the dominant mode and thus provide minimal information about the material. Initially, investigations from the researchers found multiple ways to employ a spectrum analysis of the materials. Harmonic based sampling of the permittivity spectrum is realized as a microwave dielectric spectrum to characterize material is reported in [139]. Authors in [143] have considered harmonics to extract the permittivity of dielectric slabs for LTCC (low temperature co-fired ceramic) characterization.

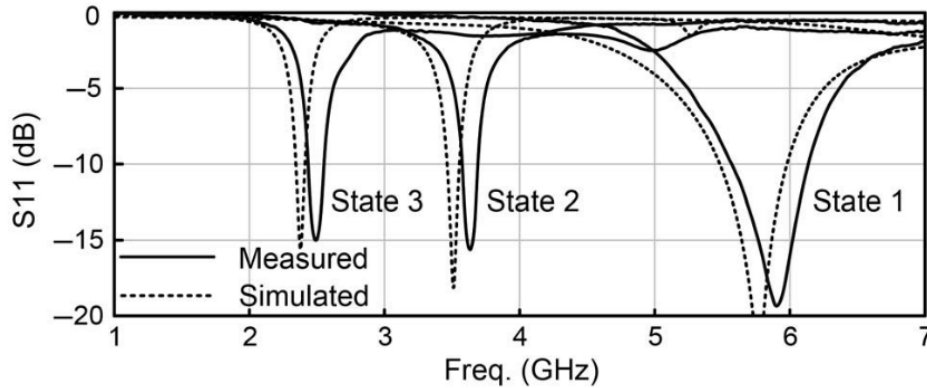


Figure 3.14: CPW folded slot antenna integrated with liquid metal to achieve three different frequency bands of 2.4, 3.5 and 5.8 GHz. Copyright © 2015 IEEE. All rights reserved [109].

Microwave spectroscopy has been used for various purposes. Few examples include the usage of microwave spectroscopy to discriminate between

sub-populations of B lymphoma cell lines with a frequency of 40 MHz to 40 GHz [144] and used a coplanar waveguide (CPW) transmission line for the dielectric characterization of HepG2 cells with a frequency range from 1 to 40 GHz [145]. In [109], CPW folded slot antenna employing liquid-metal as capacitive loading is realized to achieve reconfigurability, and three different frequency bands of 2.4, 3.5, and 5.8 GHz has been achieved by employing liquid metal at different positions. The response is shown in Figure 3.14. All these methods employ a discrete frequency spectrum where only a few resonant points far from each other can be achieved. Frequency spectrum achieved by continuously tuning the resonant frequency enables more resonant points within a narrowband. In chapter 4, a modified planar microstrip split ring resonator structure was designed and integrated with liquid metal, and 3D printed fluidic channel to achieve a continuous tunability of resonant frequency. The continuous tuning of the operating frequency helps achieve more resonant points close to each other within a narrowband and provides a highly accurate resonant-based spectroscopy.

The urgency for accurate identification increases as microwave detection and sensing becomes more common. This is an ongoing challenge, and the unique ability of microwave sensors to sense and identify the dielectric properties of solid, liquid or gaseous materials can be hindered when the material under test (MUT) is present in unknown or uncontrolled conditions. This issue has not been adequately addressed in many previous studies, where liquid detection has been performed in controlled environments where the liquid and concentration are standardized [29, 146–149]. Similarly, selectivity issues arise in other sensing operations. A larger material with a low dielectric constant may affect the resonant response in the same way as a small material with a high dielectric constant, leading to misidentification.

One approach that can take advantage of the frequency dependency of dielectric properties and avoid the overlap of dielectric properties is to take multiple measurements of the same material and conditions at multiple frequencies, generating a unique spectrum of properties rather than a singular data point. In this way, even mixtures that may have identical permittivity and loss tangent at one frequency can be separated by tuning the frequency. This idea of spectroscopy in the microwave frequency regime has been investigated before [150, 151]: Albishi *et al.* [152] developed a multiple resonator system to address the problem, but this required multiple resonators in a larger area, and measurements required a machine learning algorithm due to complex coupling between them. The issue of selectivity has also been dealt with by developing new resonator designs and finding empirical algorithms to detect sample size and chemical makeup combinations. Hosseini

### 3.4. Microwave Spectroscopy

---

*et al.* [153] created a sensor that captures the concentration of mixtures by analyzing multiple higher-order resonant modes, but this still measured at fixed frequencies and required wideband detection from 1.4 to 4.3 GHz.

In this thesis, by combining the benefits of liquid metal, 3D printing, and planar microwave resonators, aiming to improve upon earlier designs to fully characterize the capabilities of a modified split ring resonator with a simple and compact design that enables continuous frequency tunable sensing and high selectivity for many types of materials. The developed resonant based spectroscopy technique is utilized to detect and distinguish between samples that exhibit similar dielectric properties in a frequency and presented in chapter 4.

## Chapter 4

# Adjustable Microwave Resonator

This chapter outlines the design and simulation process of the adjustable microwave resonator using a 3D printed fluidic channel and liquid metal. In order to verify the results from the simulation, a fabricated resonator has been tested, and results have been compared through RF characterization. This work has been accepted for publication [154].

### 4.1 Design and Simulation

Figure 4.1 displays a pictorial diagram that explains the whole process step by step from the design concept to result validation. The comparison of results from structural simulation, equivalent circuit model, and the experiment has verified the assessment of the whole operation.

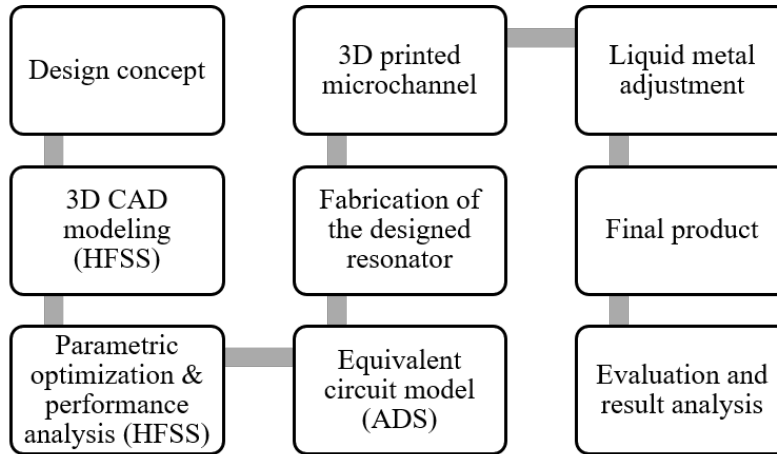


Figure 4.1: Pictorial depiction of the device development process.

### 4.1.1 Design methodology of the resonator structure

SRR's are small metallic rings or square loops with a split placed on top of a dielectric substrate. SRR's are among the first microwave resonators focused primarily on metamaterials whose geometries are smaller than the wavelength of exciting electromagnetic waves [155]. Up to now, extraordinary designs have been delivered within the discipline of metamaterials, and the most traditional ones are circular and rectangular split-ring resonators. These have been investigated concerning distinctive performance parameters, including sensitivity for sensing programs [156]. Rectangular designs are capable of imparting better sensitivity while they may be utilized for sensing applications [156]. Although, circular SRR has improved bandwidth over rectangular SRR, rectangular structures are more suitable for miniaturization and dense packing than circular structures [156, 157].

A simple SRR gives maximum amplitude (resonant amplitude) at a frequency (resonant frequency) which can be determined by the geometry of the patterned microstrip lines on a substrate. The resonant frequency is dictated by the Equation 3.15. The formula itself describes that the higher the resonator's wavelength, the less the resonant frequency. The resonant frequency ( $f_r$ ) can also be estimated in terms of capacitance and inductance by the following formula.

$$f_r = \frac{1}{2\pi\sqrt{LC}}(\text{Hz}) \quad (4.1)$$

Where  $C$  and  $L$  indicate the value of the capacitance and inductance of the overall system, respectively. The reactive elements play a vital role in producing a tunable resonance, as no modification can be made to the microstrip structure after the fabrication of the resonator patch. To tune the resonant frequency, reactive elements need to be changed significantly, which can be done by either external devices such as microfluidics. Many conventional design ideas were simulated, and one of them is presented in Figure 4.2 with results to understand the operating principle.

A simple SRR is presented in this design, and a channel filled with liquid metal is added to the resonator consecutively to introduce a reactive load to the device, as shown in Figure 4.2. It is realized that with each subsequent line of liquid metal added over the resonator, it provides another path for the signal to travel. This causes the resonator to resonate at two separate frequencies, resulting in the Figure 4.2(f) presenting two resonant peaks. One resonance occurs due to the signal transmission through the designed resonator structure and the other one is due to the added liquid

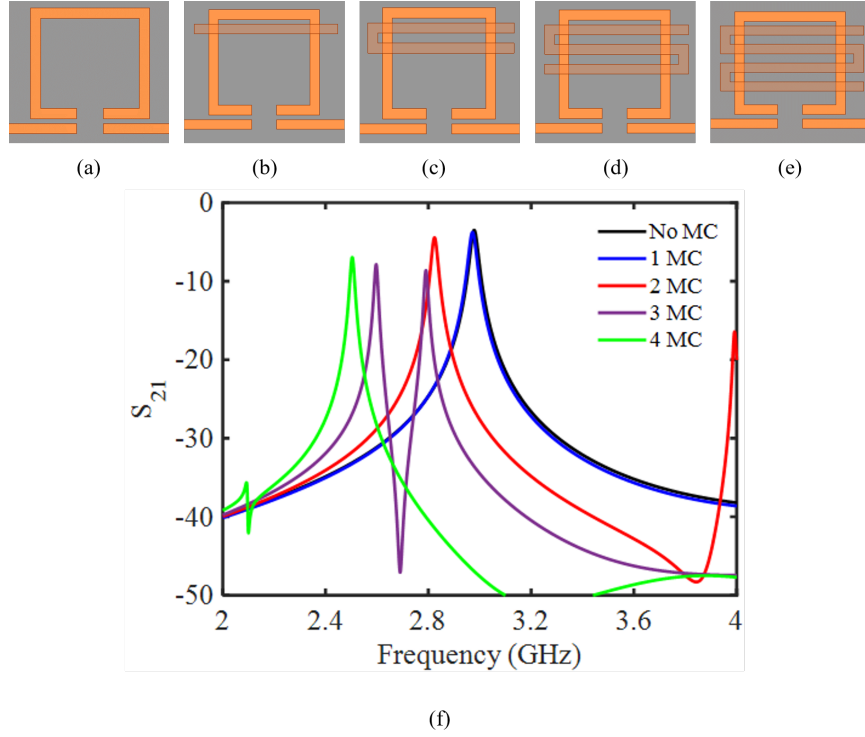


Figure 4.2: Simple SRR integrated with (a) no microfluidic channel (MC), (b) one MC, (c) two MC, (d) three MC and (e) four MC filled with liquid metal, and (f) simulation result of different configurations of MC filled liquid metal.

metal filled channels. The resonant frequency decreases because of external reactive loading added by the introduction of liquid metal filled channels. The discontinuity of the resonant frequency and less control over the frequency bandwidth makes this design not considered for tunable resonance use.

The original intent was to design a single resonator structure. However, in the design and simulation stage, it became clear that this requirement made it significantly more challenging to achieve our goals (specifically the widely tunable bandwidth and consistent resonant amplitude) using a planar resonator's constraints and a 2-port planar microfluidic channel. In fact, there are benefits to using a coupled-resonator design, such as the ability to perform differential sensing with one resonator acting as a reference and the

#### 4.1. Design and Simulation

other as a material sensor [158].

It is also believed that a single resonator approach should permit better linearity, sensitivity and perhaps enable liquid metal length to be extracted from either resonant amplitude or quality factor of the response. One of our first design attempts at a tunable single resonator is shown in Figure 4.3. The below Figure 4.3 shows that the continuity adjustment was not possible for a single resonator structure. The additional length of the liquid metal filled channel impacts on the wavelength of the resonator structure. However, our proposed design enables continuity because of the presence of coupling between the resonator's.

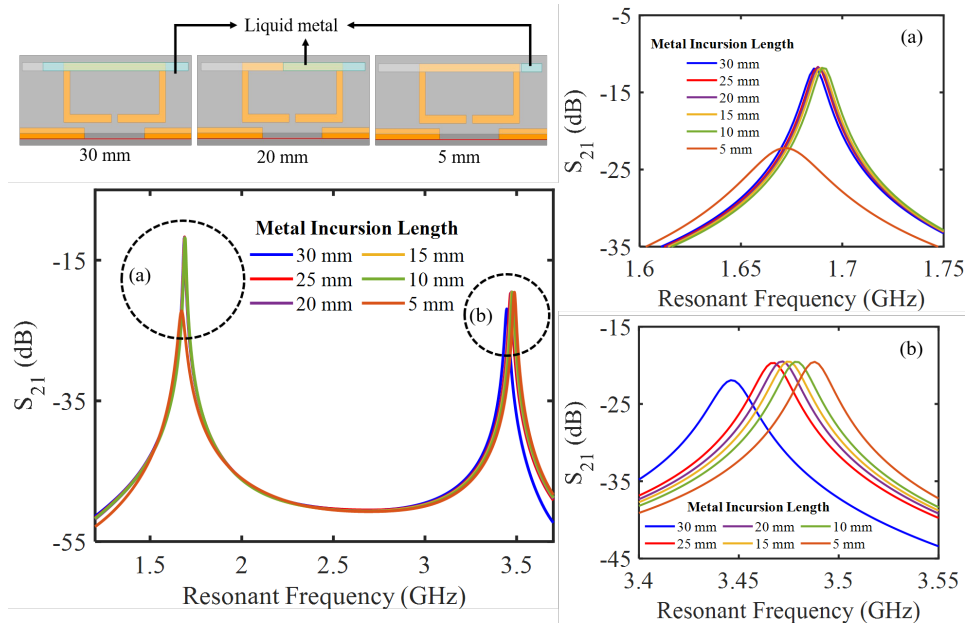


Figure 4.3: Frequency spectra of a simple SRR with varying liquid metal inside the fluidic channel.

Instead of a single resonator, multiple resonators can be used by coupling them electromagnetically [159]. Considering this idea, two resonator structures of similar configurations are designed and coupled with each other. As a result, a highly coupled resonant structure is developed. The initial intent was to design a coupled-resonator structure because the coupling can be affected by the liquid metal to achieve frequency tuning. The geometry of the resonator consists of a half-wavelength, open ring microstrip structure. The

#### 4.1. Design and Simulation

designed structure can be considered as a single resonator with two unequal splits. The designed highly coupled modified resonator structure is shown in Figure 4.4 with dimensions. The corresponding values of the resonator structure are given in the table 4.1. The geometry of the structure was designed primarily through simulation. The structure of the design can be manipulated based on user's interest.

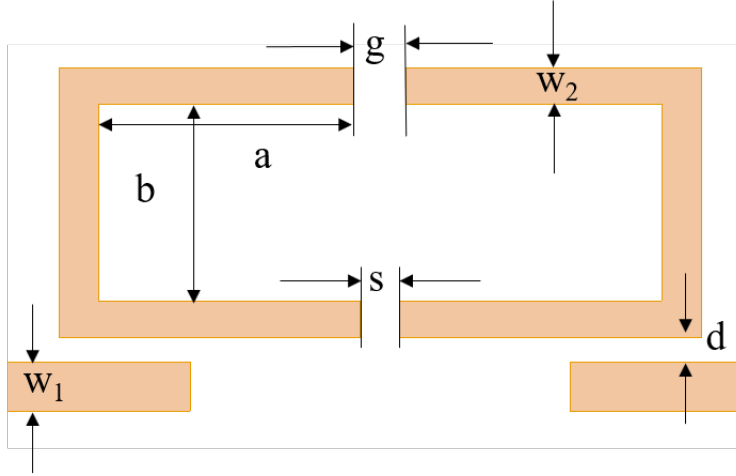


Figure 4.4: Designed highly coupled modified SRR structure with dimensions.

Table 4.1: Design parameters of the designed modified resonator structure

Symbol	a	b	g	s	$W_1$	$W_2$	d
Value (mm)	9.75	8.00	2.00	1.50	2.00	1.50	1.00

The designed resonator structure was coupled with a  $50 \Omega$  transmission line where the width ( $W_1$ ) of the transmission line was calculated using the following equation:

$$W_1 = 7.48 \times h \times e^{-\left(\frac{Z_o \sqrt{\epsilon_r + 1.41}}{87}\right)} \text{ (m)} \quad (4.2)$$

Where  $Z_o$ ,  $h$ , and  $\epsilon_r$  define the characteristic impedance of the transmission line, substrate height and the relative permittivity of the dielectric, respectively. The splits in the structure were chosen and set to ( $s=$ ) 1.5

mm and ( $g=$ ) 2.0 mm based on the simulation results and are presented in section 4.1.3. The simulation dictated that these should be the values selected.

#### 4.1.2 Design methodology of the fluidic channel

As discussed in section 3.3.2, microfluidic channels have become very prominent for guiding fluids in different applications within the microwave technology realm. The appearance of 3D printing has seen a rapid increase in the manufacturing and fabrication technology of 3D structures [160]. It has garnered a high degree of acceptance among researchers as a promising fabrication alternative. One of the most significant advantages of 3D printing technology is rapid prototyping. It is the ability to design, manufacture, and test a customized part in as little time and cost as possible. Additionally, the design can be modified without adversely affecting the speed of the fabrication process. Although it suffers from low resolution and high equipment cost, high-end 3D printing machines can improve the resolution immensely.

The structure, geometry and dimensions of the fluidic channel correspond with the microwave resonator. The design is created in Solidworks design software. The designed microfluidic channel was aligned with the resonator covering the gap ( $g$ ) in the XY plane. In Figure 4.5, the cross-section of the designed channel is presented along with the channel width, length, and height. Channel height ( $h$ ) and width ( $w$ ) are chosen to 1.5 and 2.0 mm, respectively. The length ( $L$ ) of the channel is 3 cm, and the channel interior is separated ( $d_1=$ ) 50  $\mu\text{m}$  from the structure to allow non-contact measurement. Threaded connectors were designed in both the inlet and outlet ports to ensure leak proof connection with the tubes.

The width and height of the microchannel play a vital role in achieving a wideband tuning. The longer length ( $L$ ) of the channel filled with liquid metal introduces more loss by allowing the signal to transmit to the ground and resulting in attenuation of the signal. Therefore, the length of the microchannel was chosen to be 3 cm depending on the arm length of the designed resonator structure.

The microchannel dimensions were optimized through structural simulation. It is realized from the structural simulation that increasing the height of the microchannel did not impact the resonant profile of the designed resonator significantly as it does not impact the width or the distance between the two parallel plates (liquid metal filled channel and the resonator). Simulations were performed with different values of  $w$  (width) for liquid metal

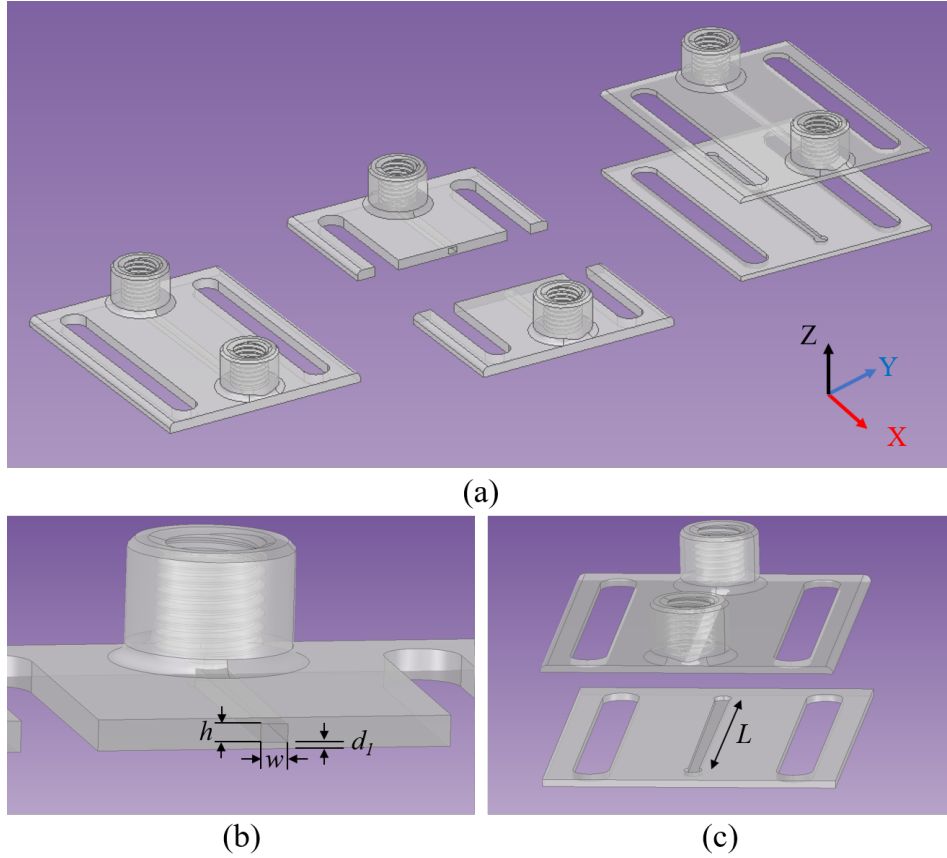


Figure 4.5: (a) The cross-section of the designed fluidic channel, (b) channel height ( $h=$ ) 1.5 mm, width ( $w=$ ) 2.0 mm and channel separation ( $d_1=$ ) 50  $\mu\text{m}$  and (c) channel length ( $L=$ ) 3 cm.

amount of 20 mm, 26 mm and 32 mm; the results are included here within Figure 4.6. Increasing the width of the channel slightly varies the frequency and impacts the quality factor. By varying the width of the microchannel, it affects the wavelength and enables a shorter path to the signal to transmit. Hence, lower wavelengths increase the frequency and decreases the quality factor.

Figure 4.6 shows the variation of resonant frequency in different widths when the liquid metal has filled the channel by 32 mm, 26 mm, and 20 mm. The widths are chosen to simulate 1.5mm, 2.5mm, 3.5mm, and 4.5mm.

#### 4.1. Design and Simulation

It can be depicted from the simulation result that the higher the width, the more space it covers, and it creates an additional capacitance to the ground, which allows more signal to transmit to the ground. In summary, the microchannel dimensions ( $L, w, h$ ) may vary depending on the resonator structure and the application. Based on the simulation results, the length, width and height of the fluidic channel are set to 3 cm, 2  $\mu\text{m}$  and 1.5  $\mu\text{m}$ , respectively.

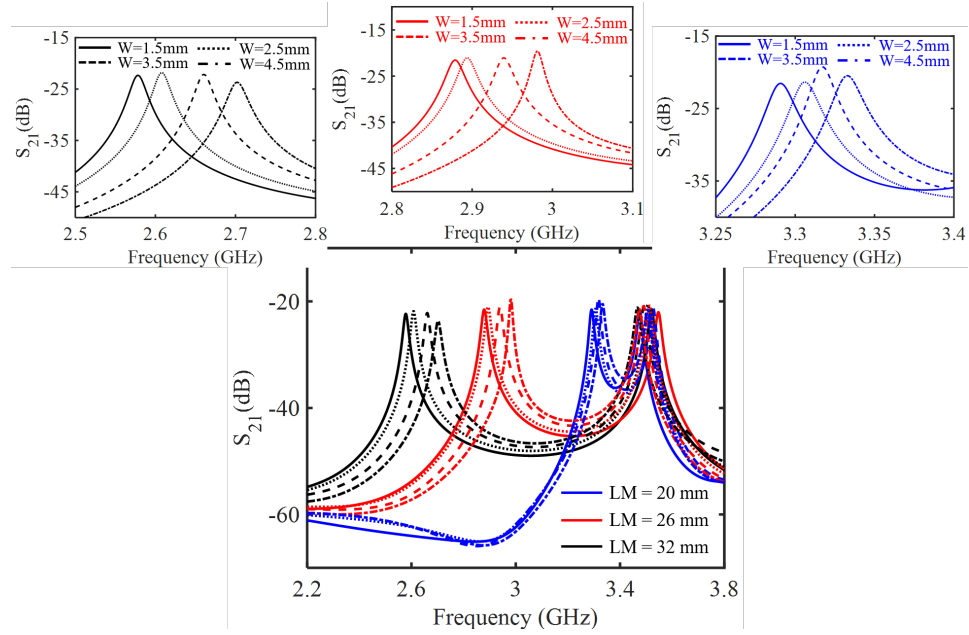


Figure 4.6: Resonant frequency shift at different widths when liquid metal length is 32mm, 26mm and 20mm.

#### 4.1.3 Structural simulation

For simulation and design purposes, Ansys HFSS (High Frequency Structure Simulation) is used. The resonator patch is made of a layer of copper that is 35  $\mu\text{m}$  in thickness. The structure is coupled to the input and output signal ports using microstrip feedlines. The resonator structure is implemented on an RT/duroid 5880 dielectric substrate from Rogers, which has a dielectric constant and loss tangent of  $2.20 \pm 0.02$  and 0.0009, respectively. The dielectric substrate has a thickness of 0.79 mm. The substrate's bottom

#### 4.1. Design and Simulation

layer is covered with 35  $\mu\text{m}$  thick copper as the ground layer. The designed fluidic channel is integrated with the resonator structure.

To replicate a realistic scenario, a co-polyester with a permittivity of 2.1 and loss tangent 0.008 represents the channel. The material that symbolizes liquid metal in the simulation is made of the actual characteristics of liquid metal in real. Simulations used the HFSS software program with a mesh size of  $\lambda/10$ ; the whole layout is covered with a vacuum airbox with radiating boundary conditions. The input-output feedlines are connected to ports with a full port impedance of 50  $\Omega$ . A parametric analysis was performed to analyze the frequency response for a different amount of liquid metal inside the microchannel. Frequency sweep from 2 GHz to 4 GHz with 2001 points was performed initially.

Figure 4.7 shows the layout of the designed resonator integrated with the designed fluidic channel. The resonator patch and the co-polyester channel are separated by 0.1 mm to replicate a realistic scenario. There will always be a negligible airgap between any bonding. The microchannel is also separated by 0.6 mm from the resonator patch to allow for non-contact resonance. Figure 4.8 shows different levels of separations to reflect a practical scenario.

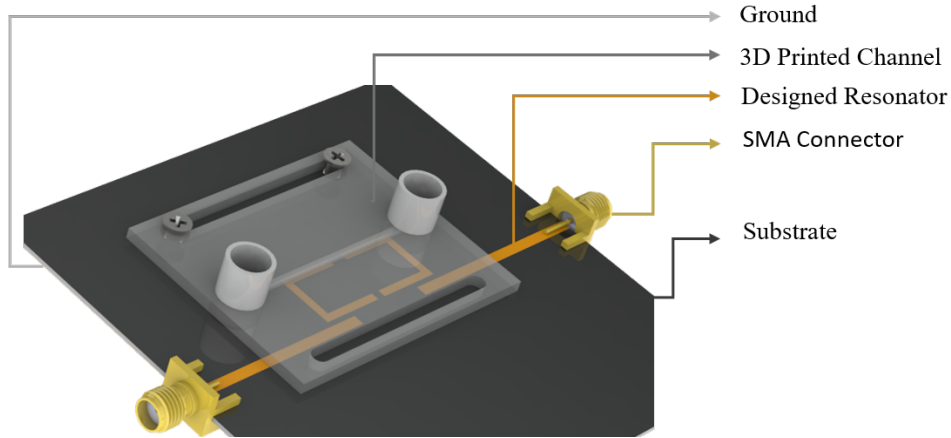


Figure 4.7: Layout of the designed resonator integrated with fluidic channel.

Initially, the simulation was performed for different gap sizes to understand the impact of gap size on the designed resonator structure. In order to do that, the split, “s” was kept 1.5 mm, and the gap, “g” was varied from 1.5 to 4.0 mm. The transmission spectra ( $S_{21}$ ) for different gap sizes

#### 4.1. Design and Simulation

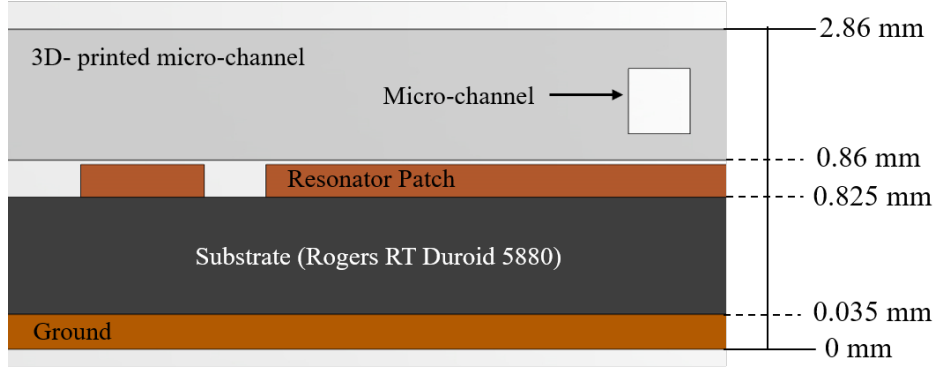


Figure 4.8: Cross-sectional sideview of the designed resonator integrated with fluidic channel.

is presented in Figure 4.9(a). The result displays one resonant frequency when the gap sizes are equal. However, the structure exhibits two resonant peaks close to each other for unequal sizes of gaps. It is realized from further investigation that equal gap sizes limit the range of frequency tuning. As a result, the final structure was designed with a gap size of 2 mm to allow a sufficient coupling gap between two resonant structures.

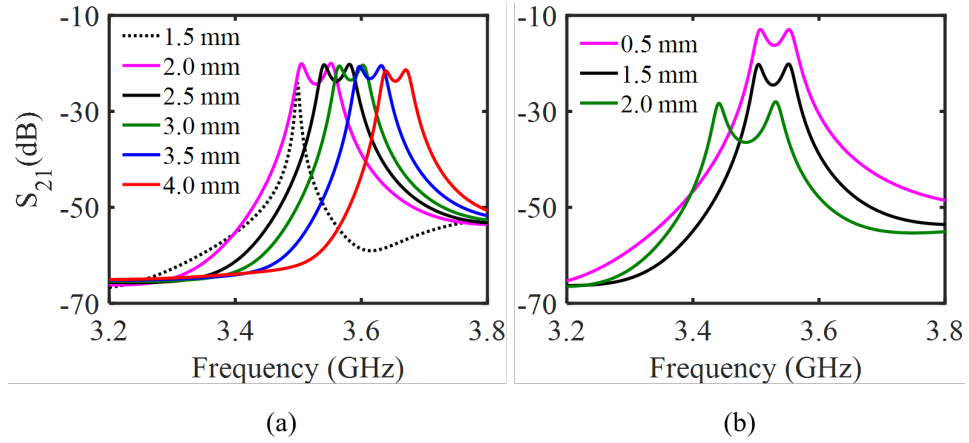


Figure 4.9: Transmission spectra ( $S_{21}$ ) of the designed resonator structure for (a) different gap sizes,  $g$  and (b) different coupling distances,  $d$ .

Another critical parameter that contributes to the performance of the resonator is the coupling distance ( $d$ ) between the ring and the transmission line. The losses would be smaller if a relatively small gap is used, but the fields in the resonant system will also be more greatly affected. A wider gap results in less field interference but greater losses [79]. The impact of different coupling distances were analyzed through structural simulation presented in Figure 4.9(b) and realized that the greater the coupling distance, the greater the effect on the resolution (quality factor) of the ring's performance. Considering the effect on the resolution, the effective coupling area was increased, and the coupling distance was kept at 1 mm for optimum performance of the designed structure.

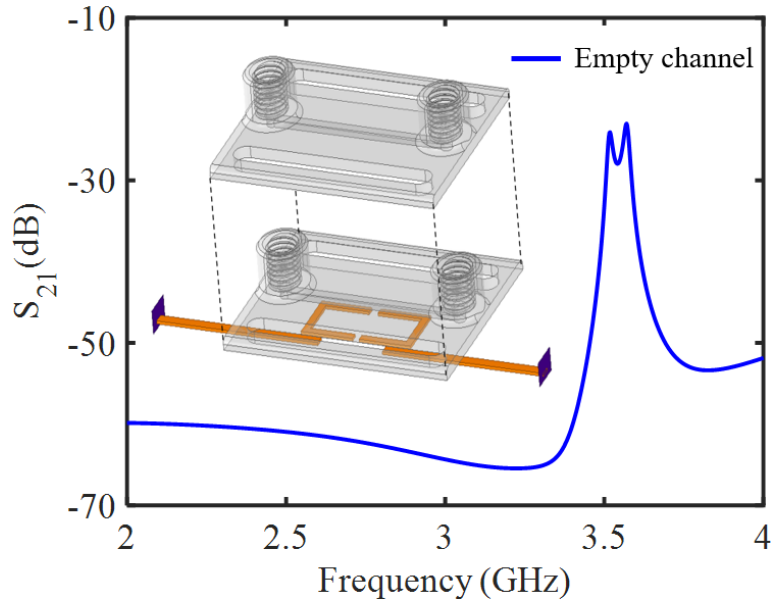


Figure 4.10: Transmission spectra ( $S_{21}$ ) of the designed resonator structure.

The final design contains two unequal splits of 1.5 mm and 2.0 mm in an SRR, and the coupling gap between the feedlines and the resonator structure was chosen to be 1 mm. The transmission spectra ( $S_{21}$ ) of the designed modified resonator structure with an empty fluidic channel is presented in the Figure 4.10. It exhibits two resonant frequencies of 3.52 and 3.57 GHz with a resonant amplitude of -24.06 and -23.00 dB, respectively. The proposed resonant structure consists of two rings electromagnetically coupled with each other. Electromagnetic coupling utilizes both the electric

#### 4.1. Design and Simulation

and magnetic coupling between the rings. At one resonance, the electric coupling is dominant, and at another peak, magnetic coupling is dominant. The overall response utilizes a superposition of both the couplings, which reflects in the transmission spectra having two resonant peaks close to each other.

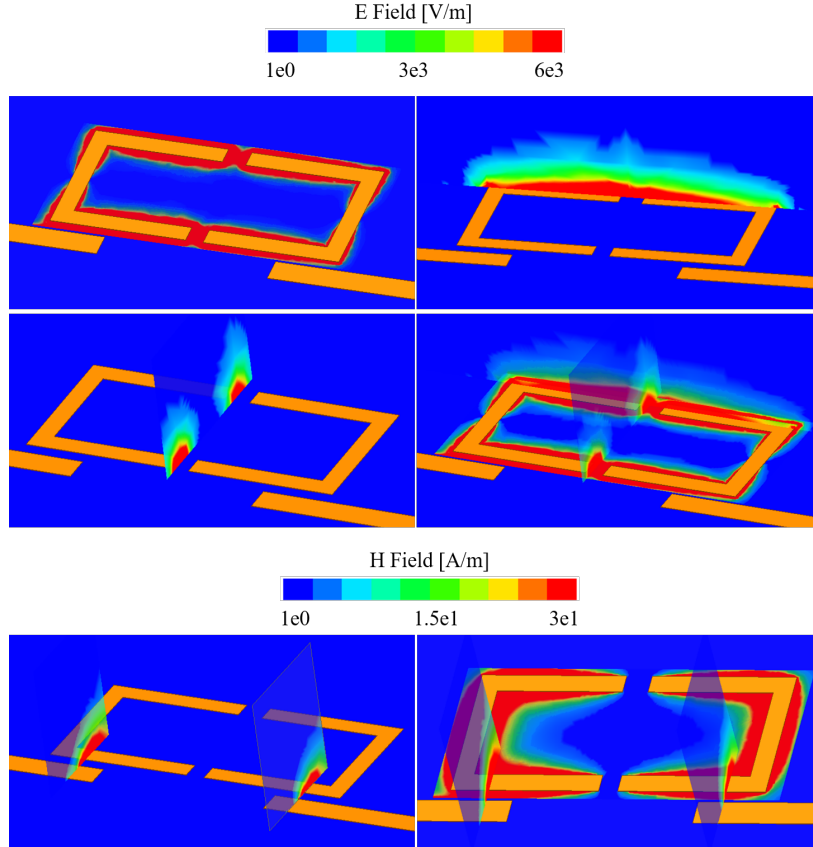


Figure 4.11: EM field distribution plot of the designed resonator structure from HFSS at a resonance of 3.52 GHz.

The EM field distribution is a necessary investigation when dealing with microwave circuits. It helps to observe the electric and magnetic field intensity in different areas of the structure. EM field distribution of the designed structure was performed in HFSS at one resonance (3.52 GHz) and presented in Figure 4.11. The electric field distribution was performed in different planes of the structure. It is realized from the field distribution

plot that there is a high electric field intensity in the gaps of the designed structure, and the intensity is not only limited to the XY plane, but also contributes to XZ and YZ plane.

From Figure 4.11, transmission feedlines and the resonator structure are magnetically coupled with each other. The magnetic coupling between the resonator and the feedlines are observed to be strongest when the coupling distance is 1 mm. There is no contribution of the magnetic field between the ring structures, which means only the electric field contributes to achieving the resonance of 3.52 GHz. It is evident that any material in the ring gap would affect the structure's overall permittivity, and a change in the resonant frequency will be observed.

## 4.2 Fabrication and Experimental Setup

This section will describe fabrication of the microwave setup as well as how it was utilized in the experimental setup. The measured results are compared with the structure simulation afterward to validate the idea and concept. The designed resonator structure was fabricated using an in-house fabrication process, and the designed fluidic channel was 3D printed and outsourced. After the fabrication, elements were needed to connect accordingly to perform the experiment and collect the datasets.

### 4.2.1 Fabrication of highly coupled resonator structure

Figure 4.12 shows the fabricated resonator on top of a high-frequency substrate whose surface was covered with a thin layer of copper as the grounding material. In this thesis, Rogers RT/duroid 5880 high-frequency substrate was used to fabricate the designed highly coupled resonator structure and the input-output lines. The thickness and dielectric constant of the high-frequency substrate were 0.79 mm and  $2.20 \pm 0.02$ , respectively, with a loss tangent of 0.0009.

Rogers 5880 substrate has the advantages of low electrical signal loss, effective-cost, lower dielectric loss, better thermal management and improved impedance control. A layer of copper was covered the surface of the substrate with a thickness of 35  $\mu\text{m}$ . The copper was selectively patterned to layout the micro-strip lines for the resonator. SMA (SubMiniature version A) connectors are soldered with the input-output line to facilitate the connections with the measurement device.



Figure 4.12: Fabricated resonator structure on Rogers RT/duroid 5880 high-frequency substrate and SMA connectors are soldered with the feedlines.

#### 4.2.2 3D printed fluidic channel

Figure 4.13(a) shows the fabricated PDMS microchannel and Figure 4.13(b) shows the fabricated PDMS channel integrated with the designed resonator structure. A PDMS microchannel was initially designed based on the fabricated resonator structure to guide the liquid metal. Due to the high viscosity of liquid metal, the fabricated PDMS channel suffered mechanical expansion and shifting, and the resonant response was affected. The high pressure of liquid metal also consistently created leakages in the PDMS channels, specifically at the inlets and outlets of the fluidic channel. As a result, an alternative approach of 3D printed microchannel was considered to facilitate the liquid metal flow.

The designed fluidic channel was outsourced, and a co-polyester NGEN colorFabb was 3D printed, which has the permittivity and loss tangent of 2.1 and 0.008, respectively. The channel was mechanically fixed with the resonator using plastic nuts and bolts. This allows more electrical stability to attain higher precision and improved sensitivity. The channel was separated from the resonator by  $50\ \mu\text{m}$  to allow no contact with the resonator.

## 4.2. Fabrication and Experimental Setup

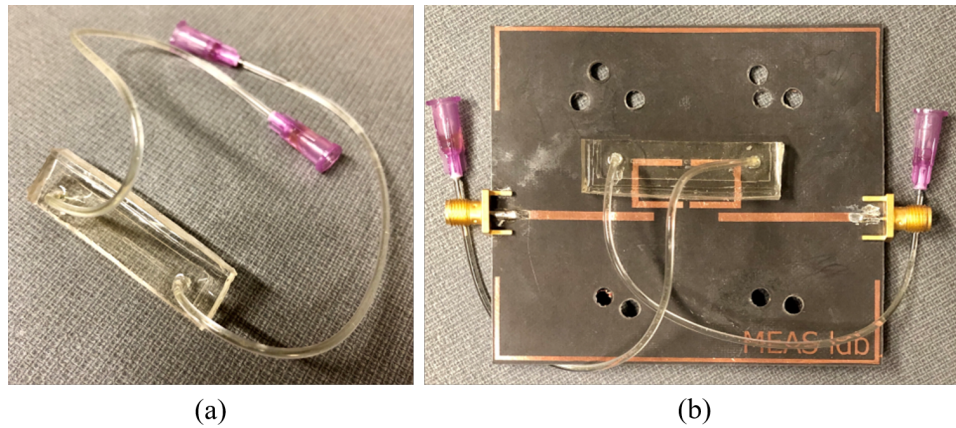


Figure 4.13: (a) Fabricated PDMS microchannel and (b) the designed resonator structure integrated with the PDMS microchannel.

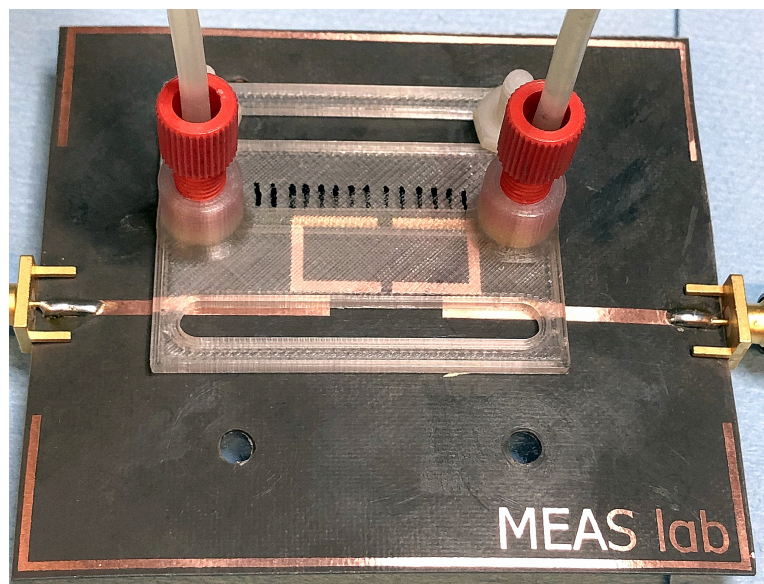


Figure 4.14: Fabricated resonator integrated with 3D printed fluidic channel.

Inlet and outlet tubes were attached to the microchannel to allow the liquid metal to transfer. Figure 4.14 shows the fabricated resonator integrated with the 3D printed fluidic channel. The length of the channel is chosen

## 4.2. Fabrication and Experimental Setup

3 cm based on the designed resonator structure. Microchannel width and height are chosen 2 mm and 1.5 mm, respectively. The 3D printed channel was cross-sectioned, and the surface profile of the embedded channel was tested through a profilometry experiment.

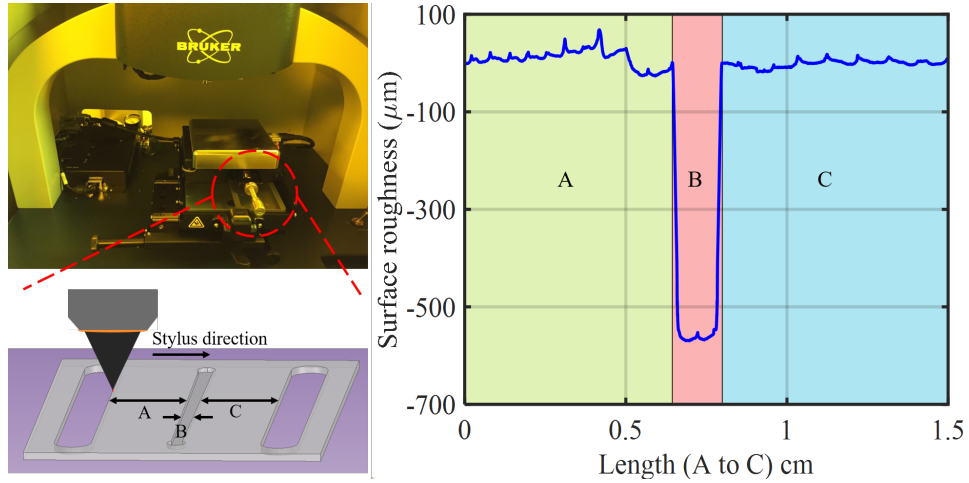


Figure 4.15: Surface profile of the 3D printed fluidic channel along the length A to C.

The surface profile of the 3D printed fluidic channel was inspected through a Dektak XT Bruker Stylus Profiler. Initially, the experiment was performed to measure the surface profile along the length A to C as indicated in Figure 4.15, and the measured result is presented in Figure 4.15. The displayed result indicated three different color-coded regions where “B” represents the embedded channel profile with an average surface roughness of  $\approx 2$  microns. Additionally, the measured average surface roughness along the length A and C were  $\approx 9.58$  and  $\approx 0.5$  microns, respectively. The surface profile across the embedded fluidic channel was also tested, and the result is shown in Figure 4.16. The result shows an average surface roughness of  $\approx 7$  microns. Irregularity on the surface can create surface friction resulting in liquid metal residues on the surface. This can immensely affect the performance of the resonator. During the experiment, the presence of some liquid metal residues was found inside the fluidic channel. To eliminate this issue, liquid metal was injected and moved back and forth to collect the residues. Hence, the fluidic channel shows excellent performance and perfectly performs fluid movement without adversely affecting the resonator’s performance.

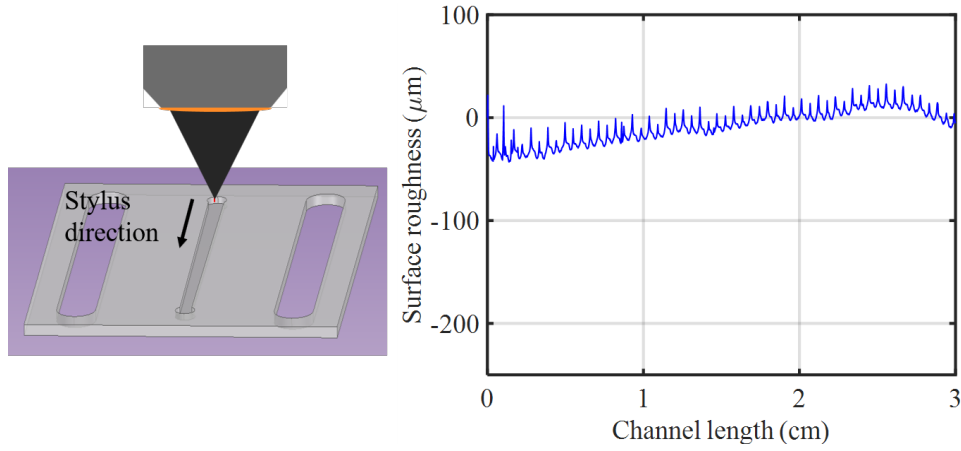


Figure 4.16: Surface profile of the embedded channel inside the 3D printed structure.

### 4.2.3 Experimental setup

The fabricated highly coupled resonator structure and the 3D-printed channel are integrated using plastic nuts and bolts for mechanical stability. Inlet and outlet tubes are used for the injection and subsequent withdrawal of liquid metal. In order to have control over the injection of liquid metal, 11 Pico Plus Elite programmable syringe pump from Harvard instruments was used. The standard infuse/withdraw method controlled the flow rate of liquid metal into the microchannel. The input and output ports were connected to port 1 and port 2 of the vector network analyzer (VNA) to allow the signal transmission. The experimental setup was surrounded by microwave absorbing foam (AN79) to limit mechanical and electromagnetic noise from entering the system. The experimental setup is shown in Figure 4.17 to understand the overall setup.

## 4.3 RF Characterization

In this section, results from different platforms such as HFSS, ADS, and experiments are analyzed and compared. Structure simulation results and measured results were found in very good agreement. Few other parameters are also analyzed and will be presented in this section.

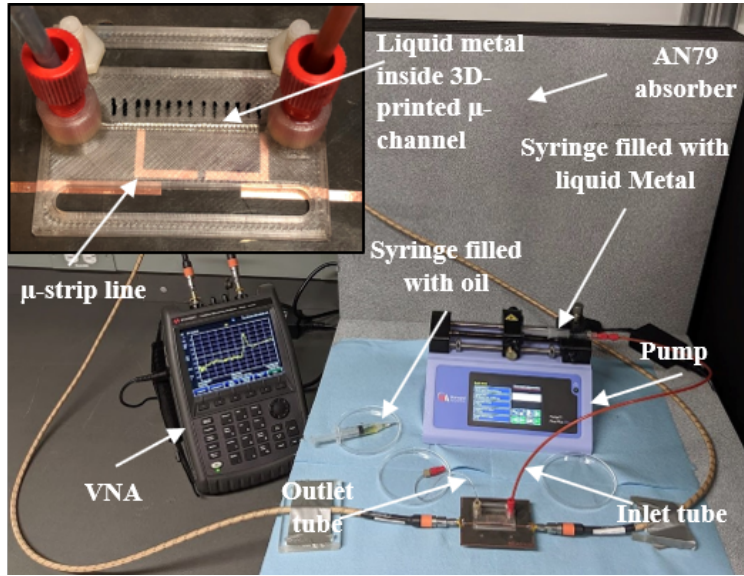


Figure 4.17: Experimental setup used to measure the  $S_{21}$  response of the tunable resonator. The fabricated resonator filled with liquid metal and microchannel implementation is shown in the top-left inset.

### 4.3.1 Scattering (s) parameter measurement

The scattering parameters of the structure simulation were performed using a parametric sweep for the length of liquid metal from 10 mm to 28 mm, which covers the whole microchannel. The simulation was performed for a linear count of frequency from 2 GHz to 4 GHz with 2001 equivalent points. The result showed in Figure 4.18 describes the change in resonant frequency ( $f$ ) in GHz and the amplitude ( $S_{21}$ ) in dB. When the liquid metal started to cross the gap (12 mm), it was found that the resonant frequency decreases with a fairly constant amplitude and quality factor. When the liquid metal length is less than 12 mm, it does not impact the resonant frequency because it does not alter the resonator's coupling until it crosses the gap. The Figure displays the resonant frequency decrease with the incursion of liquid metal.

The transmitted signal ( $S_{21}$ ) was measured with a Fieldfox Vector Network Analyzer (VNA). The VNA's output power and intermediate frequency bandwidth were set to 0 dB and 100 kHz, respectively, and the measurements were accrued over 2001 evenly distributed frequency points. Each

### 4.3. RF Characterization

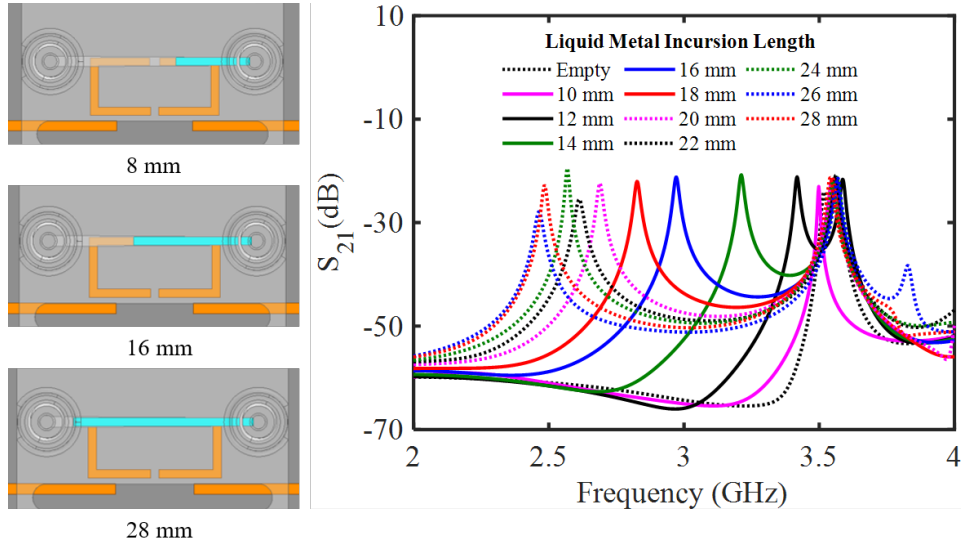


Figure 4.18: Frequency spectra from structure simulation for different liquid metal amounts. Few of the instances of liquid metal inside the channel is shown on the left side.

dataset has been collected a minimum of five times for consistent data and a better understanding of system errors. The unloaded resonator had center frequencies at 3.57 GHz and 3.52 GHz with resonant amplitudes of -23.00 and -24.06 dB, respectively. These resonant responses are highly dependent on the length of liquid metal present in the microfluidic channel.

To tune the resonator, Galinstan (liquid metal) was pushed using the pump from Harvard instruments. The standard infuse/withdraw method controlled the flow rate of liquid metal into the micro-channel. One issue was that Galinstan's high surface tension made it regularly stick to the walls of the tubing and the microchannel. To eliminate this problem, Hydrocal 2400 oil initially flowed through the tube and the microchannel as a lubricant, and it also benefited as a potential barrier to liquid metal oxidation. The microfluidic channel was filled to varying levels with liquid metal to tune the circuit's resonant response subsequently. This technique utilized the reactive loading effect of the liquid metal on the ring resonator structure. As a result of merely increasing the overall circuit's reactive loading, the frequency of resonator decreases in all simulations and was also recorded in experiments.



to act as a sensor for dielectric materials.

### 4.3.2 Equivalent circuit modeling

The  $LC$  circuit modeling is observed to be very useful to analyze and control the behavior of the EM structure for final assessment. The equivalent circuit model is designed based on the results of the simulation. Agilent Advanced design simulation (ADS) software was used to design and evaluate the equivalent circuit model results.

Considering the modified SRR to be mutually coupled with the input and output (i/o) microstrip line, the i/o lines were modeled by mutual inductance between the resonator patch and the i/o line. Each of the resonators are represented by a  $R-L-C$  combination where  $R$ ,  $L$  and  $C$  refers resistance, inductance and capacitance respectively. Both the resonators are electrically coupled with each other. The liquid metal acts as a single stub and enhances the reactive loading by coupling with the resonator patch.

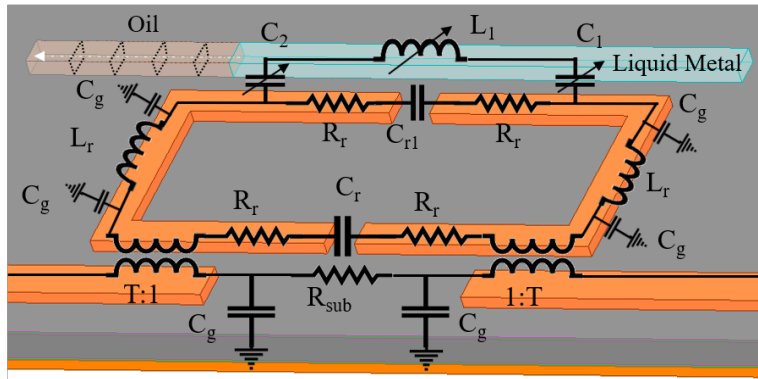


Figure 4.20: Equivalent circuit model overlaying the substrate, resonator and liquid metal.

In Figure 4.20, the lumped element equivalent circuit model overlaying the substrate, resonator, and liquid metal is presented.  $L_r$ ,  $C_g$  and  $R_r$  represents the inductance of the line, the capacitance between resonator patch and ground, and resistance of the line, respectively. To consider the loss in line and substrate,  $R_{sub}$  and  $R_r$  are modeled. The electrical coupling between the resonators was modeled by capacitance  $C_r$  and  $C_{r1}$ . The liquid metal stub is modeled by a series  $LC$  circuit connection, which is represented by  $C_1$ ,  $L_1$  and  $C_2$ . In this case, the values are variable for  $LC$  combination

### 4.3. RF Characterization

because the liquid metal length defines these reactive elements' values. In table 4.2, the calculated values of the corresponding elements are presented.

Table 4.2: Defining the values of the parameters of the equivalent circuit model based on the simulation results.

Symbol	Value	Unit	Symbol	Value	Unit
$R_r$	5.0	$\Omega$	$C_1$	5- $C_2$	pF
$L_r$	31.485	nH	$C_2$	0.28-2.90	pF
$C_r$	0.0357	pF	$L_1$	9.60-30.21	nH
$C_{r1}$	0.031	pF	$C_g$	0.02	pF
T	7.66		$R_{sub}$	54.3	$\Omega$

Without the liquid metal stub, the calculated values are fixed for the resonator. Incursion of liquid metal enables external reactive elements  $C_1$ ,  $L_1$  and  $C_2$  to contribute to the resonator profile. Increasing the liquid metal volume increases the capacitances and inductance. When liquid metal is very close to the gap, the resonant profile begins to be impacted. Since liquid metal before the gap does not impact the coupling between the resonators, the resonant frequency change is negligible. Liquid metal acts like a bridge that connects both the resonators and impacts the coupling. When liquid metal starts crossing the gap, the resonant frequency starts to decrease with a consistent amplitude and quality factor as characterized in the previous section.

#### 4.3.3 Results comparison

The designed resonator structure had a tuning range of 1.04 GHz, adjusting between 2.48 to 3.52 GHz. Structure simulation and equivalent circuit modeling of the designed channel with and without liquid metal in the channel were performed, and results were compared with the experiment in Figure 4.21. Figure 4.21(a) shows the empty channel results and Figure 4.21(b) shows the filled channel results. The results are similar but varied slightly, possibly due to the lack of a standard liquid metal in the literature or oxidation of the Galinstan upon exposure to oxygen in the channel during the experiments.

### 4.3. RF Characterization

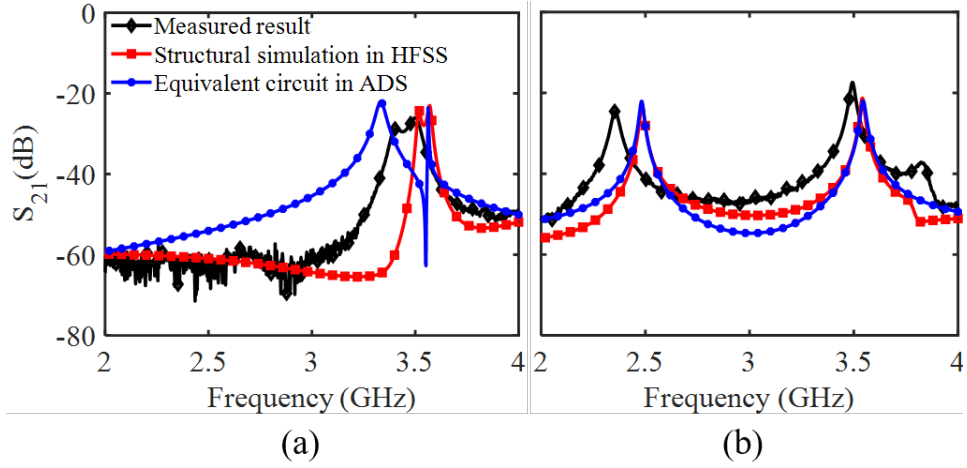


Figure 4.21: Comparison between the simulated (HFSS and ADS) and measured  $S_{21}$  frequency spectra for the resonator with the fluidic channel in (a) empty state and (b) filled state.

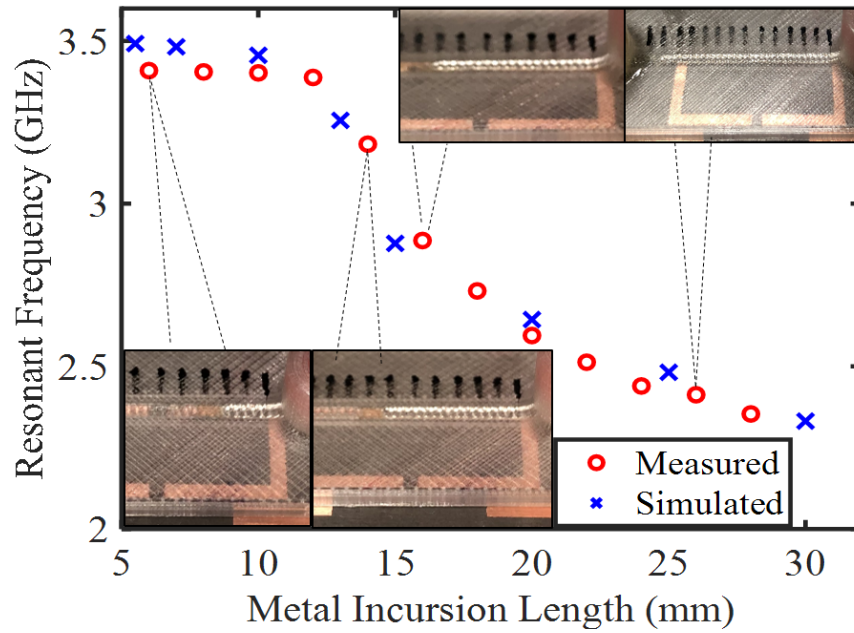


Figure 4.22: Resonant frequencies recorded for different metal lengths with selected images included.

Figure 4.22 presents the trend between liquid metal length and resonant frequency shift found from both experiment and simulations. The blue cross defines the values from the structure simulation, and the red circle defines the measured responses from the experiment. Resonant frequency is dropping with liquid metal length because of additional reactive loading added to the resonator profile. The measured value confirms simulation as both are in good agreement. Therefore simulation is validated.

#### 4.4 Chapter summary

A tunable microwave resonant structure was created with a resonant frequency that could be adjusted between 2.35 and 3.40 GHz by using the logical capability of liquid metal as an adjustable capacitive source. Control of the resonant frequency was conceivable by pushing various volumes of Galinstan through a 3D printed microchannel situated over the resonator. A resonant frequency shift of 1.05 GHz with a quality factor of 70 ( $\pm 5$ ) was experimentally measured with insignificant ( $< 3$  dB) variety in resonant amplitude. The designed structure has a tunable frequency, empowering frequency-specific connections between resonator and sample using a single resonator. This plan can be effectively executed to many frequency ranges as a microwave filter or sensor and holds potential in the field of microwave frequency spectroscopy.

## Chapter 5

# Resonant Based Spectroscopy for multi-phase material detection

In this chapter, resonant based spectroscopy has been utilized to differentiate between the samples of similar dielectric properties. The discussion starts by stating the problem through the Debye model, followed by the design and simulation process of the microwave resonant sensor. The designed sensor utilizes liquid metal to generate spectroscopic data for multi-phase material detection. Experiments have been performed to characterize and validate the designed sensor. The presented results are the collective presentation of more than adequate simulations and measurement efforts that have sometimes been unsuccessful due to proper presentation and experimental clarification.

### 5.1 Problem statement

Many studies have focused on sensing materials using microwave resonator technology, and by using these resonator sensors, materials with dissimilar properties can easily be identified, and distinguished [26, 161]. The problem arises when the resonant properties of different materials are the same at specific frequencies due to a combination of their size, shape, or composition. Introducing a continuously tunable frequency spectrum using a resonant-based structure could be a possible solution to eliminate this issue because of the many factors in a material's response are affected differently by frequency variation.

To understand this problem in a microwave resonator sensor, two generic materials, A and B, were created, and the dielectric properties of these materials were analyzed with the Debye model. Debye model is used for the MUT's to consider the frequency dependence of the dielectric properties. According to the Debye model, the real ( $\epsilon'$ ) and imaginary part ( $\epsilon''$ ) of the

### 5.1. Problem statement

complex dielectric permittivity are calculated using the following equation:

$$\epsilon' = \epsilon_{\infty} + \frac{\epsilon_s - \epsilon_{\infty}}{1 + \omega^2\tau^2} \quad (5.1)$$

$$\epsilon'' = \frac{(\epsilon_s - \epsilon_{\infty})\omega\tau}{1 + \omega^2\tau^2} \quad (5.2)$$

Where  $\epsilon_s$  and  $\epsilon_{\infty}$  define the permittivity at low frequency and high frequency, respectively. Operating angular frequency and the dielectric relaxation time are defined by  $\omega$  and  $\tau$ , respectively.

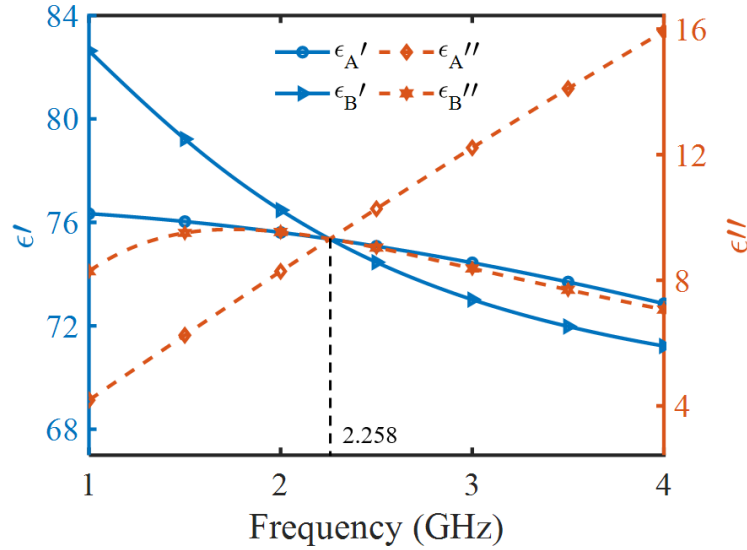


Figure 5.1: The calculated dielectric complex permittivity of material A and material B at 23.7°C modelled by Debye method. The parameters for material A were set to match water:  $\epsilon_s=76.58$   $\epsilon_{\infty}=4.73$   $\tau=9.3$  ps. Material B was defined by  $\epsilon_s=87.37$   $\epsilon_{\infty}=68.13$   $\tau=90.9$  ps.

The designed materials are modeled using the Debye formulation, and the real and imaginary part of the permittivity was calculated and presented in Figure 5.1. As shown in Figure 5.1, the dielectric permittivity and loss factor for both materials (A and B) were found to intersect at 2.258 GHz frequency, which means both materials exhibit identical dielectric behavior at that frequency. This generates a critical problem for resonant based methods in terms of sensing and characterizing the materials using

resonant-based structure. Any microwave resonator sensor operating at this frequency is unable to distinguish between the materials. However, upon referencing the Debye model, deviating from the intercept point introduces the possibility of detecting different values of dielectric permittivity of the materials. Therefore, a resonator is demanded whose resonant frequency could be adjusted to avoid the intercept.

## 5.2 Operating principle of the designed resonator sensor

The previous design of the resonator structure presented in chapter 4 was modified by integrating an interdigitated capacitive sensor. Many different types of sensors structure are available in microwave technology, and most of the sensors often work on sensing dielectric properties. The resistive and the capacitive techniques are immensely used for the fabrication of the microwave sensors. The capacitive sensor provides low-temperature dependence, miniaturization potential, small power consumption with possibilities of sensing a minimal variation in the materials properties [162–166]. Different capacitive structures are possible for the fabrication of the sensor, such as parallel plates, co-axial cylinders, fringing fields [162]. However, among them the co-planar interdigitated capacitive sensor is most widely used in the microwave technology. Interdigitated capacitive sensors are a non-destructive method of studying material properties such as conductivity, permittivity, and permeability [167].

The interdigitated capacitive sensor is implemented in this design to sense the MUT within a large, highly sensitive area [167]. The impact of the MUT in the sensitive region can be monitored via the effective dielectric property variation in that sensitive region [168]. The large sensitive region attained by the interdigitated structure enabled sensitive monitoring of permittivity and conductivity variation over a larger area [169]. The operation of the interdigitated capacitive sensor is similar to a parallel plate capacitor [162]. The interdigitated capacitive structure is designed to provide high capacitance when coupled to the resonator, increasing frequency tunability. The design also provides a large region with a high electromagnetic field to help identify the MUT. The electric field travels around the resonator and across the capacitor by penetrating the MUT, which changes the impedance of the sensor. Therefore, by measuring the changing  $S_{21}$  transmission of the sensor, the MUT properties can be evaluated over time. The relation between the effective dielectric permittivity and the resonant frequency is

presented in equation 3.15.

Tuning of the resonant frequency follows the similar principle of operation discussed in chapter 4. Liquid metal inside the fluidic channel contributes to the resonant frequency tuning by impacting the coupling between the ring structures. The change in the relative permittivity of the resonant profile due to the presence of the MUT alters the resonant frequency of the resonator, and by calculating the frequency shift, materials can be characterized [26].

### 5.3 Design methodology and simulation

#### 5.3.1 Structure design and tunable operation

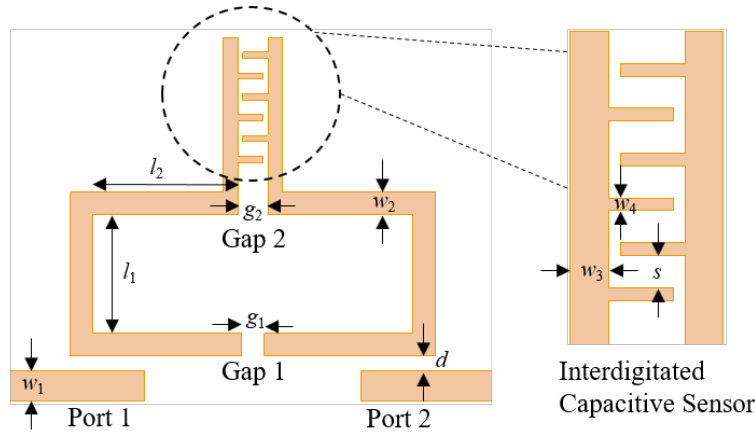


Figure 5.2: Structural design of the proposed resonator sensor with dimensions.

The sensor structure consists of a highly coupled modified split ring resonator integrated with an interdigitated capacitive sensor presented in Figure 5.2. The resonator loop consists of two gaps (gap 1 and gap 2), which made the rings highly electromagnetically coupled. This was further improved by an interdigitated capacitive sensor region for material sensing. The planar structure has resonant frequencies determined by the size and shape of the designed microstrip lines. The modified structure allows the resonator to exhibit two resonant peaks close to each other due to two unequal gaps in the ring structure. This was optimized in the previous channel.

### 5.3. Design methodology and simulation

The dimensions of the sensor structure are shown in table 5.1.

Table 5.1: Defining the values of the parameters of the designed sensor

Symbol	Value (mm)	Symbol	Value (mm)
$l_1$	8.00	$w_2$	1.50
$l_2$	9.75	$w_3$	1.00
$g_1$	1.50	$w_4$	0.40
$g_2$	2.00	s	1.00
$w_1$	2.00	d	1.00

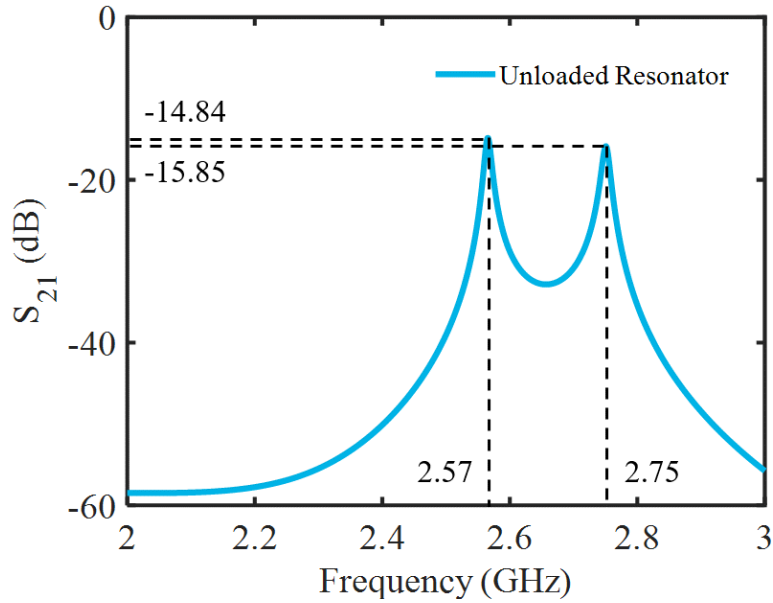


Figure 5.3:  $S_{21}$  response of the unloaded resonator from the HFSS simulation software.

The resonator sensor structure was implemented in ANSYS High Frequency Structure Simulation (HFSS) software to study the liquid metal impact on the resonator and material testing. The  $S_{21}$  transmission of the unloaded resonator from the HFSS simulation is presented in Figure 5.3. The unloaded resonator resonates at 2.57 GHz with -14.84 dB and 2.75 GHz with -15.85 dB of amplitude based on the simulation result. The field distribution of the designed structure is also analyzed in the HFSS platform.

### 5.3. Design methodology and simulation

According to the field distribution plot, the higher resonance ( $f_H$ ) occurs at 2.75 GHz due to the magnetic field coupling between the resonator and the sensor, and the lower resonance ( $f_L$ ) occurs at 2.57 GHz due to the electrical field coupling between the resonators. The field distribution plot from the HFSS simulation is presented in Figure 5.4. Due to high electric field intensity in the interdigitated capacitive area shown in Fig. 5.4, this region is used in this design to sense the MUT over a large, highly sensitive area.

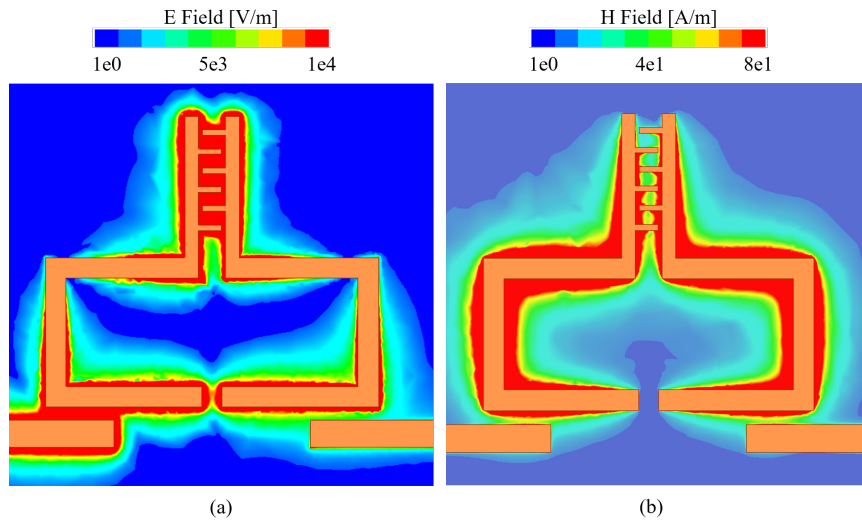


Figure 5.4: Field distribution plot (a) Electric field distribution at 2.57 GHz and (b) Magnetic field distribution at 2.75 GHz.

The designed resonator structure shown in Figure 5.2 was integrated with liquid metal controlled microfluidic channel placed above gap 2. The gap location and size relate strongly to the resonant frequency supported and can be covered with liquid metal to increase the capacitive loading of the resonator and decrease the resonant frequency [154]. Liquid metal was injected in different volumes inside the microchannel to perform the frequency tuning. To manage the controlled flow of liquid metal, the length of the channel was measured at regular 3.5 mm intervals from 18-32 mm. In practice, tuning could be done with any amount of liquid metal to target any specific frequency. According to the simulation results, a frequency tuning of 250 MHz with constant amplitude and quality factor was achieved. The

### 5.3. Design methodology and simulation

layout of the sensor structure and the simulated result from HFSS when the channel is filled with liquid metal in the length of 18-32 mm of the fluidic channel are presented in Figure 5.5a and Figure 5.5b, respectively. Additionally, the change in resonant frequency and resonant amplitude with varying liquid metal length are presented in Figure 5.5c and Figure 5.5d, respectively.

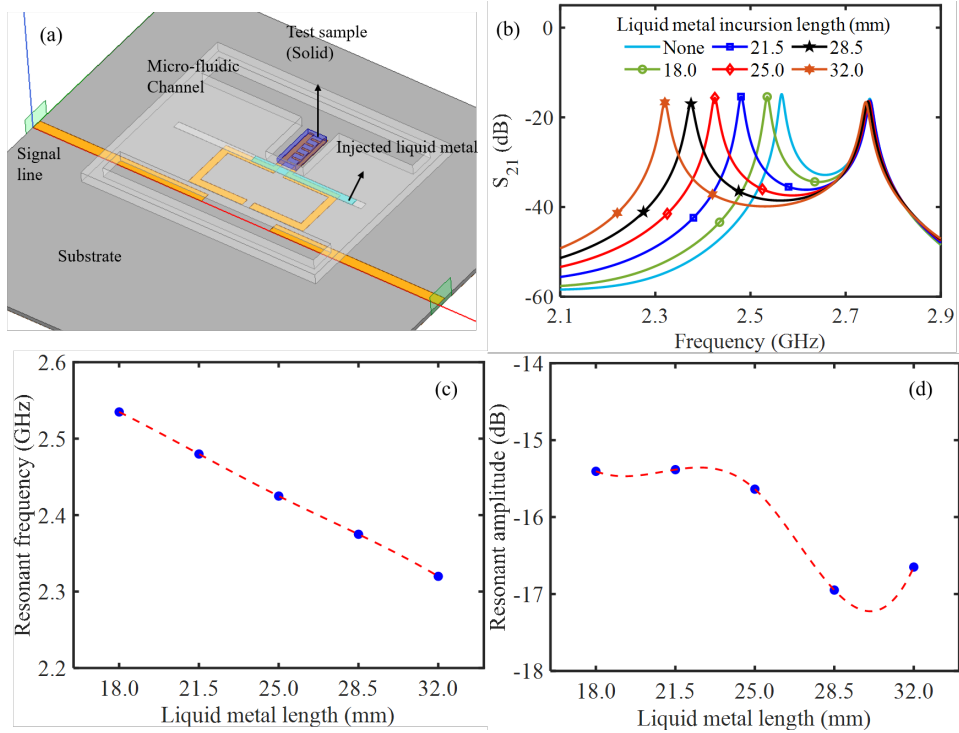


Figure 5.5: (a) Layout of the sensor structure from the HFSS software, (b) simulations results from HFSS when the channel is filled with liquid metal in the length of 18-32 mm of microfluidic channel referenced with unloaded resonator response, (c) change in resonant frequency and (d) resonant amplitude with varying length of liquid metal.

### 5.3.2 Sensitivity analysis of the designed sensor

#### Different permittivity standard solid materials

The sensitivity of the adjustable sensor was investigated through HFSS simulation by changing the amount of liquid metal volume inside the microchannel and placing materials with different permittivity on the sensing area. The testing material was placed over the microstrip lines due to high electric field intensity in the interdigitated capacitance region. MUTs of permittivity 4.3, 5.7, 6.8, 8.3, 10.0, 12.9, and 16.5 were used to analyze the sensing capability for different amounts of liquid metal inside the microchannel. To perform this operation, the microfluidic channel was filled 25mm in length with liquid metal, and standard materials with different permittivity were placed individually in the sensing area. Each material demonstrates a unique response based on its permittivity. The higher permittivity materials have higher frequency shifts, and the lower permittivity materials have lower frequency shifts due to their expected interaction with the penetrating electromagnetic field. Materials with higher permittivity interact more strongly with the electric field compared to the material with lower permittivity [170].

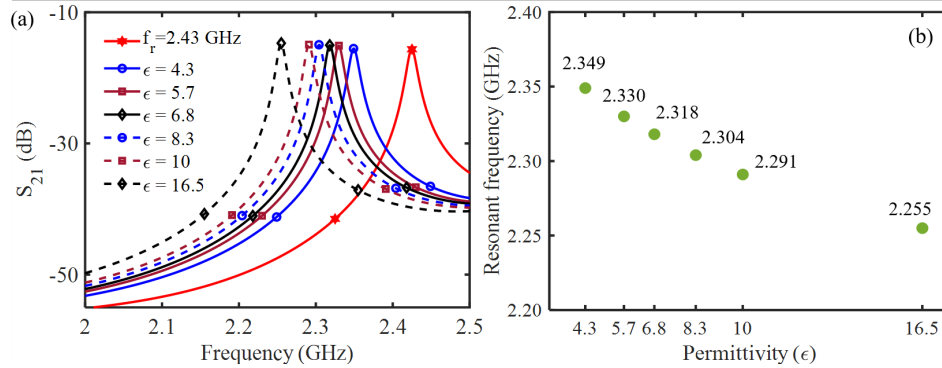


Figure 5.6: (a) Simulations results from HFSS when liquid metal is filled in the length of 25 mm of the microfluidic channel, and different solid materials are tested and (b) scatter plot indicating the achieved resonant frequencies over materials with different permittivity.

According to Figure 5.6(a), when the resonant frequency was adjusted to 2.43 GHz, which corresponds to 25 mm amount of liquid metal, materials with different permittivity exhibited different frequency shifts, and that

happens due to the change in the effective dielectric permittivity in the local sensor environment. As shown in Figure 5.6(b), a material with a permittivity of 4.3 shifted to 2.349 GHz from 2.43 GHz and another material with a permittivity of 16.5 moved the resonant frequency to 2.255 GHz.

Furthermore, the sensitivity was studied for various amounts of liquid metal volume inside the microchannel to extract the sensitivity curve for different settings, which has been demonstrated in Figure 5.7. The highest frequency difference of 224 MHz was attained for material with permittivity 16.5 at the 18 mm liquid metal location. The lowest frequency difference, 49 MHz, was attained for material with permittivity 4.3 at the 32 mm liquid metal location. According to the simulated results, lower resonant frequency corresponded to a higher amount of liquid metal, demonstrating less sensitivity to the same MUT, as expected based on equation 4.1. Thus, liquid metal enables characterizing the materials at different frequencies so that materials properties can be understood over a frequency band, much like modern spectroscopic characterization techniques.

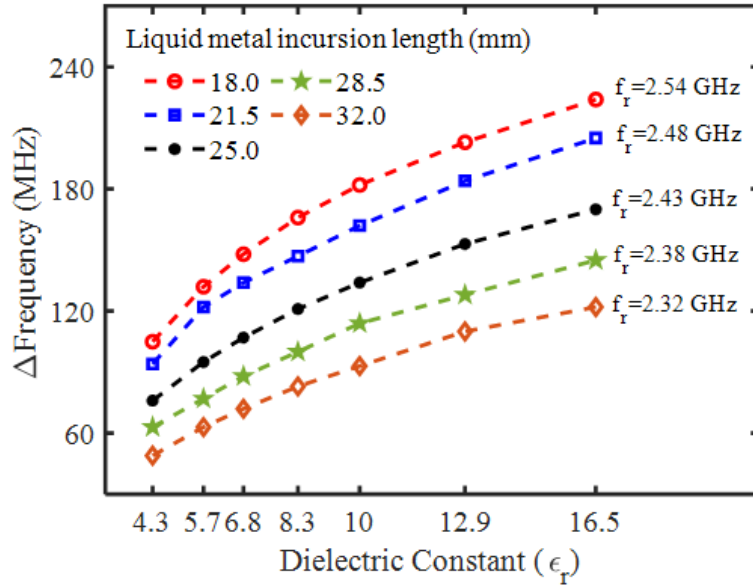


Figure 5.7: Frequency difference over different dielectric constant materials when liquid metal is in different locations inside the microfluidic channel.

Different loss tangent standard solid materials

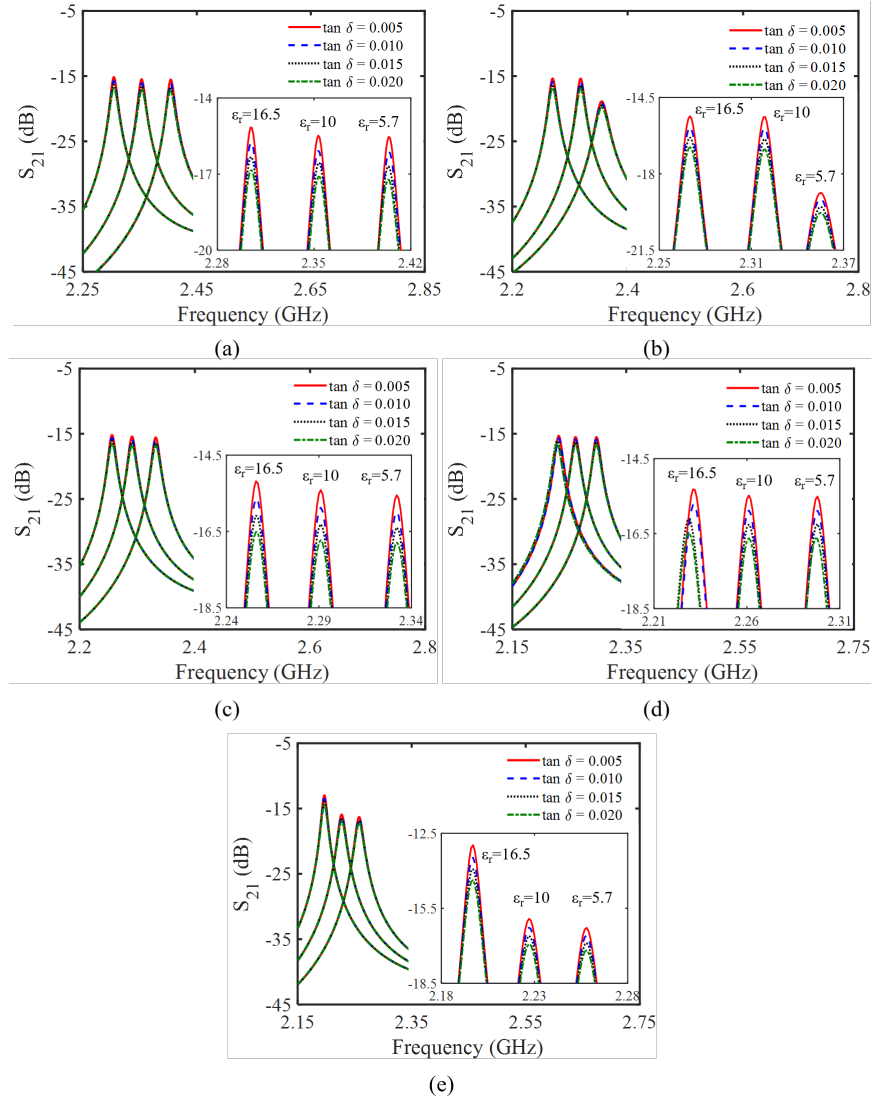


Figure 5.8: Simulation results from HFSS while varying loss tangent of test samples of permittivity 16.5, 10.0, and 5.7 at different liquid metal settings inside the microchannel. Varying loss tangent of test samples varies the amplitude of the sensor response while liquid metal is at (a) 18 mm, (b) 21.5 mm, (c) 25 mm, (d) 28.5 mm, and (e) 32 mm location. The magnification of the amplitude difference is shown in the bottom right inset at every liquid metal setting.

To characterize the designed sensor structure, the impact of different dielectric loss tangent for MUTs with the same real permittivity was studied with different amounts of liquid metal. MUT's with  $\epsilon_r = 16.5$ , 10 and 5.7 were placed on top of the interdigitated capacitive region and simulated with different values of loss tangents ( $\tan \delta = 0.005$ , 0.01, 0.015 and 0.02) at different liquid metal configurations (18 mm, 21.5 mm, 25 mm, 28.5 mm and 32 mm). With different loss tangents, the transmission amplitude response corresponds to the loss property of the MUT at resonance, while the frequency remains unchanged. The  $S_{21}$  amplitudes of the sensor with varying MUT loss tangents are shown in Figure 5.8 under various liquid metal conditions. Based on simulation results, a material with a permittivity of 10 and a varying dielectric loss tangent is reported in Figure 5.9 at different liquid metal levels. The result shows a very stable linear response in terms of amplitude and dielectric loss tangent sensitivity. As shown in Figure 5.9, the sensor had less sensitivity at higher amounts of liquid metal, reflected in the slope of the lines.

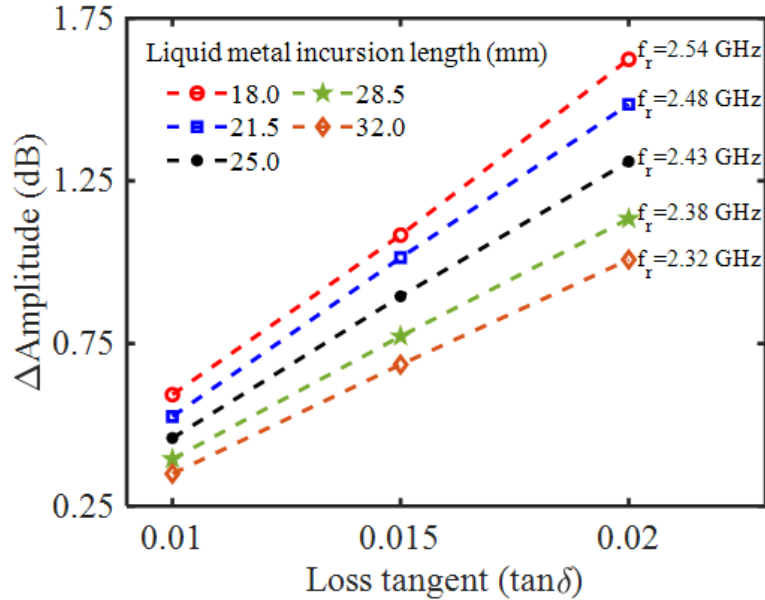


Figure 5.9: Amplitude difference compared against the loss tangent for a MUT of permittivity 10 at different locations of liquid metal.

## 5.3.3 Sensor performance analysis

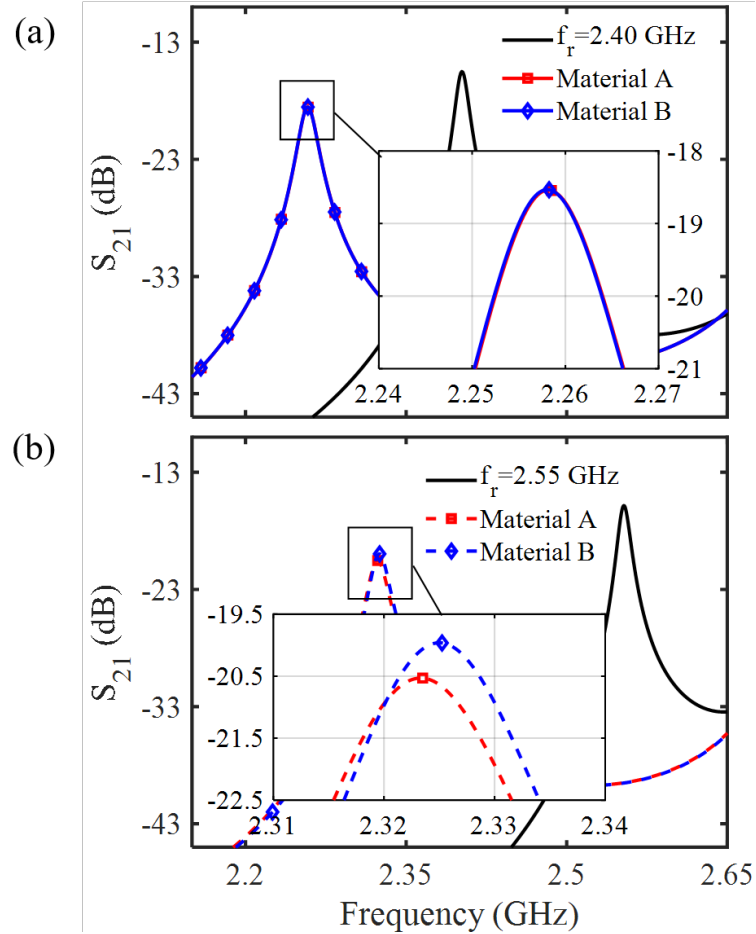


Figure 5.10: Simulated result from HFSS while testing the materials at (a) 2.258 GHz and (b) 2.55 GHz of frequency.

The dielectric data was extracted from Fig.5.1 and imported into simulation software HFSS. The designed resonator with liquid metal was then used to characterize the materials at a frequency of 2.258 GHz. The simulated result is presented in Figure 5.10a. As shown in Fig.5.10a, both materials have the same frequency response around 2.258 GHz because they have identical dielectric properties at the resonant frequency (Figure 5.1). Looking at the material's response, the resonant profile of both the materials is nearly

identical, and as a result, the two materials cannot be distinguished. By adjusting the liquid metal, the resonant frequency of the designed resonator is moved to 2.55 GHz, and the same materials were simulated with the result displayed in Figure 5.10b. The material properties no longer match identically at this frequency, and the sensor can accurately distinguish between the two materials. Testing the materials at multiple frequencies can fully characterize MUTs. Based on the presented results, a tunable resonator with an adjustable resonant profile shows promising potential in enhancing microwave resonator sensors' selectivity compared to sensors with a fixed resonant frequency.

## 5.4 Experimental setup and measurement discussion

Several sensors were fabricated with different sizes and structures, and the presented one was selected based on its performance. At first, the presented resonator sensor was characterized by measuring the sensitivity towards solid samples in the presence of the liquid metal. As explained in chapter 4, different volumes of liquid metal were used to control and adjust the sensor's resonant profile with a focus on the resonant frequency parameter. Finding samples/mixtures with similar dielectric properties is one of the essential parts of validating sensor performance. This has been done by measuring the dielectric properties of liquid samples/mixtures through the coaxial probe. Experiments were performed in three steps to achieve and prove the benefits of resonant based microwave spectroscopy. The steps are explained at length in the next sections to understand the overall measurement procedure.

### 5.4.1 Characterizing the designed resonator sensor

#### Fabrication of the sensor structure

To fabricate the designed resonator sensor and the input-output transmission line, a Rogers RT/duroid 5880 high-frequency substrate was used with a permittivity of  $2.20 \pm 0.02$ . The thickness and the loss tangent of the dielectric substrate were 0.79 mm and 0.0009, respectively. The substrate surface was covered with a coating of 35  $\mu\text{m}$  thick copper, and copper was specifically designed to model the microstrip lines of the resonator sensor and the input-output transmission lines. Copolyester was used in 3D printing technology in a particular pattern to construct the microchannel

#### 5.4. Experimental setup and measurement discussion

for liquid metal transfer and solid sensing. The permittivity and the loss tangent of the copolyester were 2.1 and 0.008, respectively.

Using plastic nuts and bolts, the channel was fixed to the resonator to avoid instability and attain higher accuracy and sensitivity. The 3D-printed microchannel was detached by 50  $\mu\text{m}$  from the resonator structure to ensure non-contact characterization. Inlet-outlet tubes were attached to the microchannel to transfer the liquid metal to achieve frequency tuning. To record the transmitted signal strength ( $S_{21}$ ), an N5222B vector network analyzer (VNA) was used by setting the output power and intermediate frequency bandwidth to 0 dBm and 300 Hz, respectively. The experimental setup for this experiment is shown and labeled in Figure 5.11.

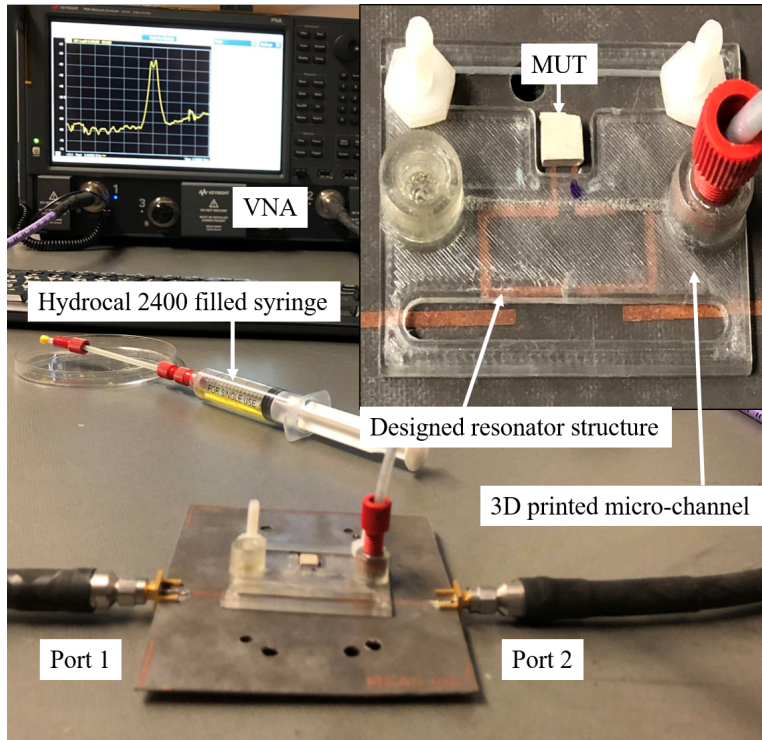


Figure 5.11: Experimental setup of the designed resonator used for testing standard samples (solid) at different resonant frequencies. The magnification of the sensor with MUT is inset in the top right corner.

**Measured results of standard solid samples detecting in different resonant frequencies**

Initially, the experiment was designed to tune the resonator to achieve different resonant frequencies using only liquid metal and to introduce solid materials in the sensing region for each resonant frequency to understand the sensor's behavior. Solid samples of permittivity 2.20, 6.15, and 10.02 and sizes of  $0.79 \times 10 \times 10$  mm were chosen for this experiment. Galinstan, a liquid metal alloy of gallium, indium, and tin, were moved through the microchannel to tune the resonant frequency. Since liquid metal requires substantial pressure to move through the channel because of its high surface tension, Hydrocal 2400 oil was initially passed through the microchannel as a lubricator and anti-oxidation layer.

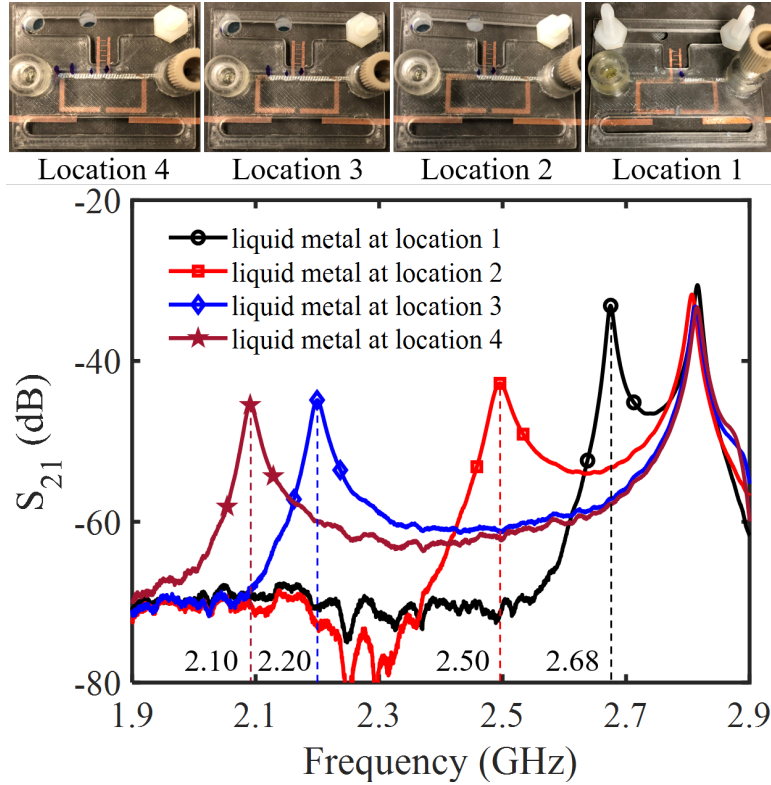


Figure 5.12: Measured response of liquid metal being at different locations inside the microchannel resulting in tunable resonant frequencies.

Different amounts of liquid metal were pushed through the microchannel, indicated as location 1 through location 4. Each of the locations was characterized by the length of microchannel filled with liquid metal; with location 1, 2, 3, and 4 containing liquid metal lengths of 18 mm, 21 mm, 24 mm, and 27 mm of liquid metal as shown in Figure 5.12. The measured resonant frequencies with liquid metal in location 1 to location 4 were 2.68, 2.50, 2.20, and 2.10 GHz, respectively. Figure 5.12 shows the different locations and their responses regarding resonant frequency and amplitude. The amplitude of the responses shown in Fig.5.12 decreased with the increased volume of liquid metal because the increased capacitive coupling introduced loss mechanisms through the ground layer of the substrate. At every recorded resonant frequency, solid samples were placed above the interdigitated capacitor, and the measured results are recorded.

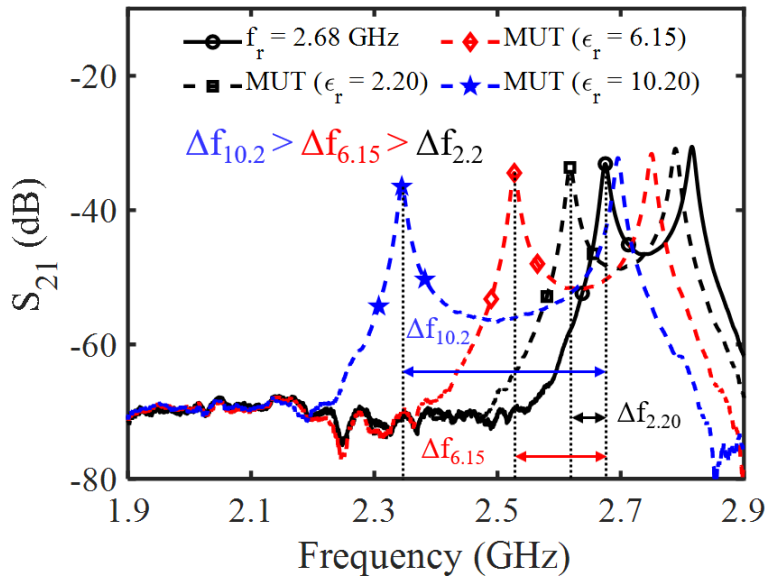


Figure 5.13: Measured response of standard materials ( $\epsilon_r=2.20$ , 6.15 and 10.20) influencing resonant frequency of 2.68 GHz.

Different materials affect the resonant profile because of their varying dielectric properties. To understand the behavior of different materials on the resonant response, Figure 5.13 presents measured results recorded for different test samples ( $\epsilon_r = 2.20$ , 6.15 and 10.20) while keeping the liquid metal at location 1 corresponding to the resonant frequency of  $f_r = 2.68$  GHz.

#### 5.4. Experimental setup and measurement discussion

As expected, the higher permittivity materials result in a larger resonant frequency change, and at location 1, the sensitivity was found to be 35.91 MHz / unit  $\epsilon$ . As shown in Fig. 5.13, the sensor structure demonstrated different sensitivity at different resonant frequencies, adjusted by the length of the liquid metal over the ring. Resonant frequency-dependent sensitivity can be attributed to the sensor's inherent behavior, which originated from the sensor's initial capacitance. At low frequency, the sensor's initial capacitance is larger than high-frequency capacitance leading to lower sensitivity at low-frequencies. The measured response of the test sample ( $\epsilon_r = 6.15$ ) in the presence of liquid metal at different locations is presented in Figure 5.14.

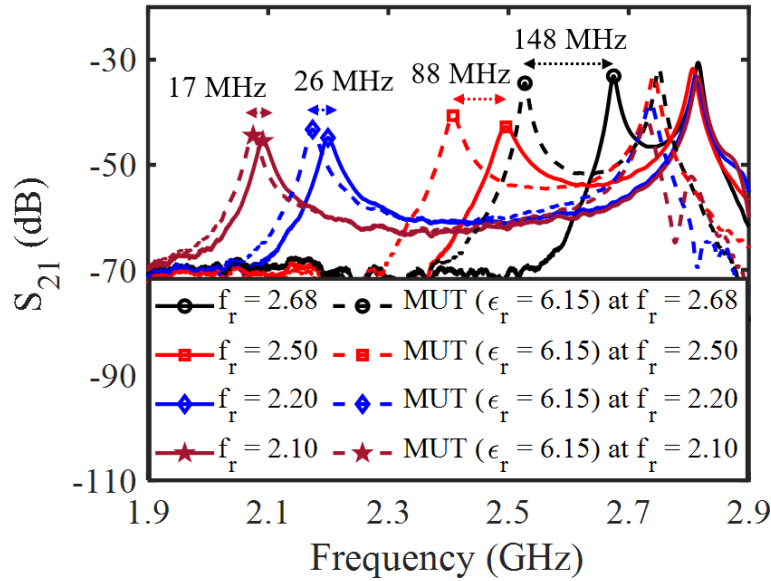


Figure 5.14: Measured response of standard material ( $\epsilon_r=6.15$ ) influencing different resonant frequencies.

The material response presented illustrates that a lower volume of liquid metal has a higher sensitivity to the material than a high volume of liquid metal inside the microchannel. The results are recorded and analyzed for the other samples at different resonant frequencies. The measured frequency shift in different test samples' presence was compared to the resonant frequency achieved by adding the liquid metal to the microchannel, as presented in Figure 5.15. Considering frequency difference,  $\Delta F = f_H -$

$f_L$ , where  $f_H$  is the resonant frequencies achieved by adding liquid metal with no material under test and  $f_L$  is the frequency measured in the presence of test samples in those resonant frequencies. It was realized from the measured results that when the resonant frequency was 2.68 GHz (liquid metal at location 1), the test sample of permittivity 10.20 had the highest frequency difference of 330.4 MHz. The frequency difference gradually decreases at the lower resonant frequencies as expected, due to their lower relative capacitance. The effect of liquid metal on sensitivity was characterized, and the sensitivities were found to be 35.91, 24.66, 9.09, and 5.93 MHz / unit  $\epsilon$  in location 1, location 2, location 3, and location 4, respectively.

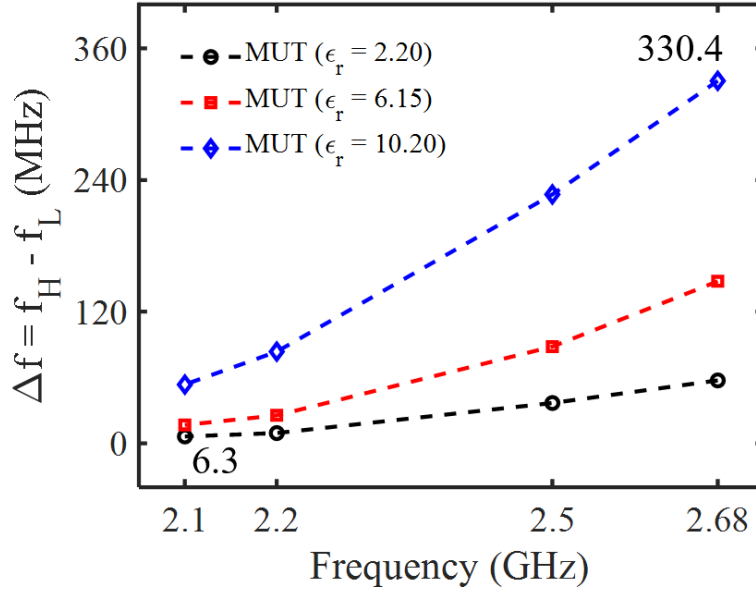


Figure 5.15: Sensitivity of the designed resonator sensor by testing samples of permittivity 2.20, 6.15 and 10.20 in different resonant frequency.

#### 5.4.2 Standard probe measurement

##### Measurement setup

The dielectric properties of a material are essential to know before they can be accurately sensed and understood with a microwave resonator sensor such as the one designed. It also adds a greater scientific value to the work presented. Dispersion ( $\epsilon'$ ) and absorption ( $\epsilon''$ ) parameters of materi-

#### 5.4. Experimental setup and measurement discussion

---

als display material characteristics over a range of frequency and can help to understand the material behavior. There are several techniques capable of measuring the dielectric properties of a material. The standard coaxial probe method is best suited for liquids and semi-liquid materials in this context [42]. It is simple, convenient, and non-destructive [42]. In this experiment, samples of similar dielectric properties are extracted experimentally by measuring the dielectric properties of pure and diluted alcohols.

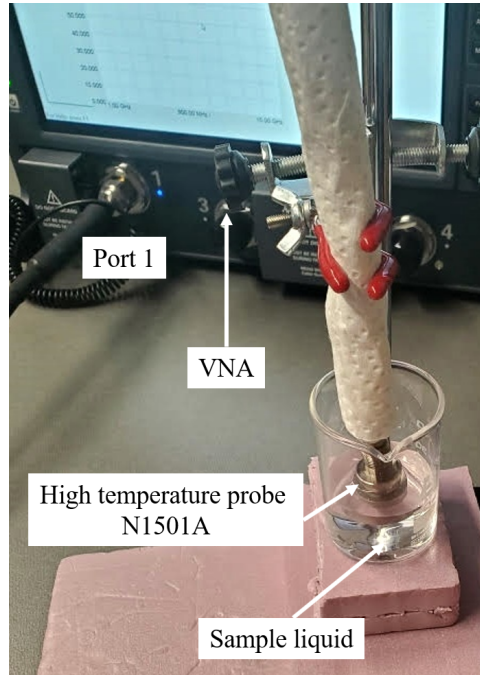


Figure 5.16: Experimental setup of the coaxial probe measurement.

A high-temperature probe N1501A shown in Figure 5.16 was used for the experiment, which can output and detect a wideband frequency of 10 MHz to 20 GHz. The VNA was connected to the probe for input reflection co-efficient ( $S_{11}$ ) measurements. The frequency range, power, and IF bandwidth of the high-temperature probe was set to 2-4 GHz, 0 dBm, and 300 Hz, respectively. Each of the readings was taken with 201 evenly distributed data points. Coaxial probe measurements used a three-load standard calibration procedure: open circuit, short circuit, and a broadband load. Deionized water was used as the broadband load, and the temperature was recorded at 23°C during the calibration. After the calibration was performed, the

dielectric properties of liquid samples, ethanol, methanol, and isopropanol (IPA) were measured.

### Measurement results of the dielectric probe experiment

The dielectric properties of the materials can easily be extracted from the literature available in scientific journals. However, in this case, the liquid samples were tested and compared for every concentration to determine the intersection point of their dielectric property. Referencing the data from the literature will not help find the same dielectric permittivity of two different samples. The presented approach here to perform the dielectric probe measurement helps identify the intersection of two different liquids in a particular frequency. The intersection point shows that two different liquid samples exhibit the same dielectric permittivity in a particular frequency.

Different concentrations of liquid samples were made and tested using the dielectric probe. After measuring the pure liquids, mixed solutions were made with volumetric concentration differences of 5%, and the results were recorded. This was done to find two different mixtures, or a mixture and a pure substance, which have the same dielectric permittivity at a particular frequency. The collected measured data from this experiment is shown in Table 5.2.

Table 5.2: Measured effective permittivity of the sample liquid solutions

Concentrations(%)		Frequency	Effective permittivity
Ethanol-water	IPA-water	(GHz)	( $\epsilon_{eff}$ )
15	10	3.13	68.72
30	25	3.94	52.59
40	35	3.70	45.97
65	55	3.22	26.49
95	80	3.49	10.48

The measured real ( $\epsilon'$ ) and imaginary part ( $\epsilon''$ ) of the complex permittivity is presented in Figure 5.17. There are samples and mixtures that showed equivalent properties, making it impossible to distinguish between such solutions looking at their dispersion property. However, it is possible to distinguish between samples and mixtures by seeing the absorption property using the coaxial probe method. Nevertheless, the readout circuitry is expensive and probably would not be used in everyday sensors.

5.4. Experimental setup and measurement discussion

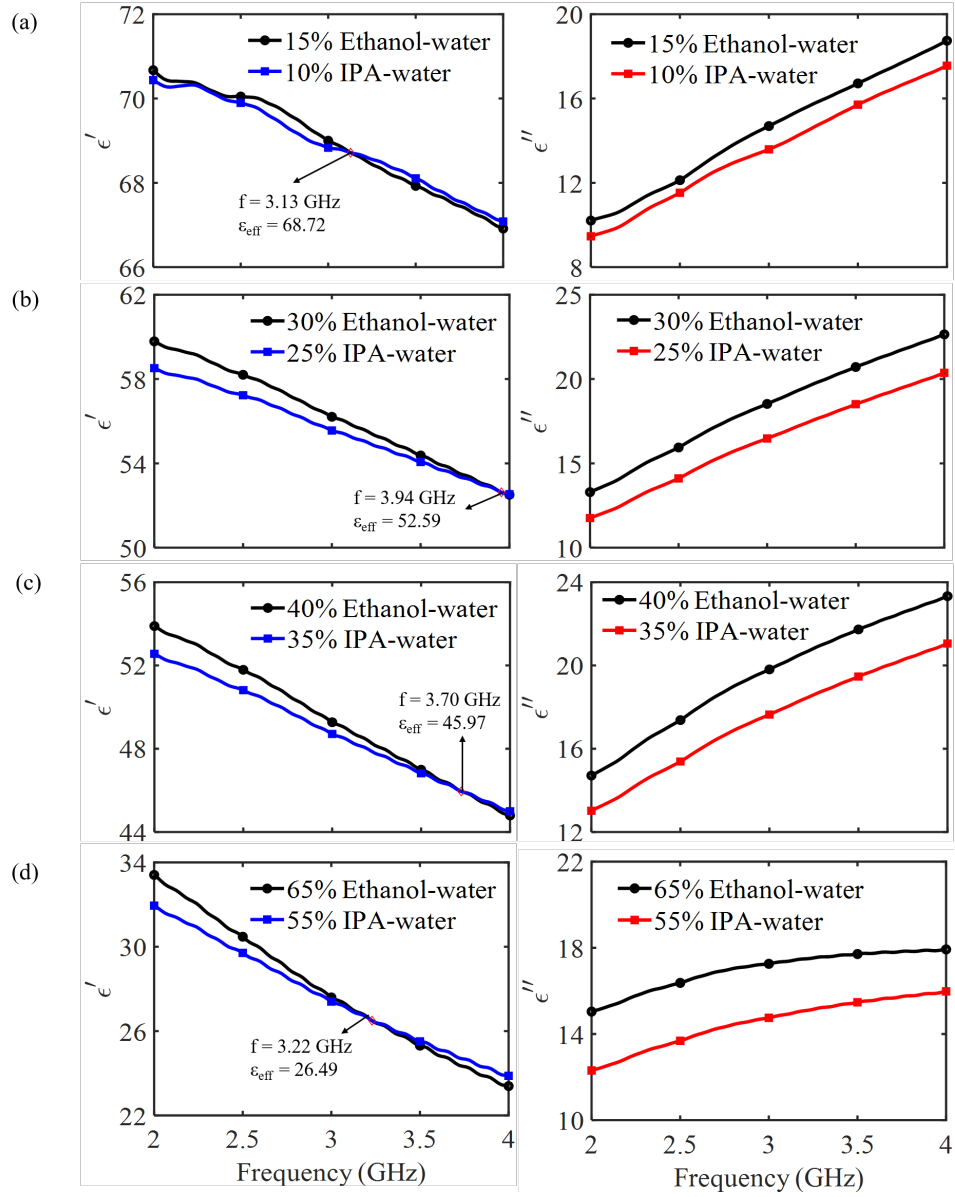


Figure 5.17: Measured real ( $\epsilon'$ ) and imaginary part ( $\epsilon''$ ) of the complex permittivity of different solutions where (a) 15% ethanol-water and 10% IPA-water, (b) 30% ethanol-water and 25% IPA-water, (c) 40% ethanol-water and 35% IPA-water and (d) 65% ethanol-water and 55% IPA-water.

Less complex readout circuitry like oscilloscope or frequency demodulator can only operate with a single frequency input or only interpret a resonant frequency as its data collection [171]. Based on these limitations, loss tangent would not be detected at all. The intersect points highlighted in the relative permittivity over the frequency spectrum in Figure 5.17 create the problem while distinguishing between the samples using a resonant-based sensor. The collected measured data from the standard probe measurement shown in table 5.2 is visualized in Figure 5.17.

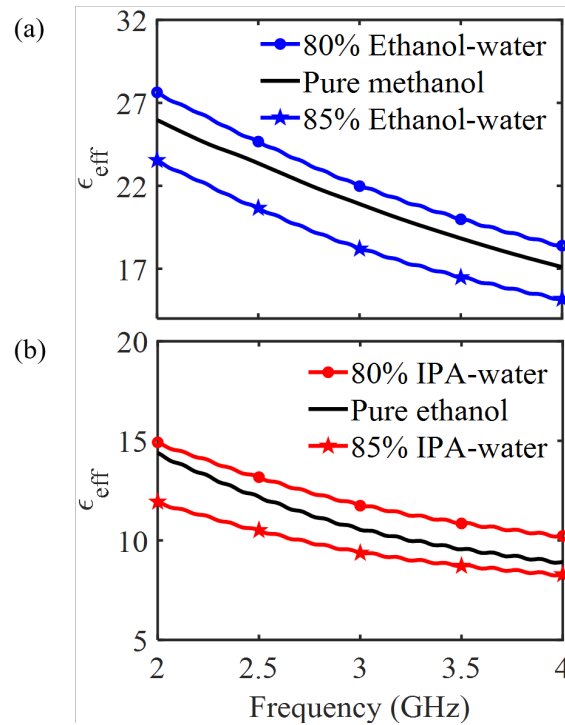


Figure 5.18: Dielectric response of (a) 80% and 85% ethanol-water compared with pure methanol and (b) 80% and 85% IPA-water compared with pure ethanol.

For experimental simplicity, the effective permittivity of pure methanol was compared with the effective permittivity of an ethanol-water solution. The measured results are presented in Figure 5.18. It is found from Figure 5.18(a) that the effective permittivity of pure methanol lies between 80% - 85% ethanol in a water solution. Such a solution highlights the inability

to distinguish between pure methanol and concentrated ethanol (81%) for the frequency range using only frequency-based methods. Similarly, Figure 5.18(b) describes equivalent behavior in comparing the effective permittivity of pure ethanol and an IPA-water solution. Considering the measured results from the standard probe experiment shown in Fig.5.18 and the achieved resonant frequencies, 81% ethanol-water solution and 83% IPA-water solution was chosen by data interpolation method to compare with pure methanol and pure ethanol, respectively.

The significance of dielectric probe measurements is very crucial to address the benefits of resonant based spectroscopy. By identifying the concentrations and their referenced frequency where different samples display similar behavior from the probe measurement, the final step to address the solution using a resonant-based spectroscopy sensor can be explained. Two unlike liquids showed the same dielectric response at a specific frequency. While specific solutions and frequencies were required to demonstrate the problem, it could fit many real-world examples as microwave sensors strive to fit more and more applications. Effectively, it is difficult to characterize and identify such liquids with a simple system. A frequency selective microwave sensor provides the flexibility to measure a frequency selective material's dielectric properties in an effective manner. It is also beneficial to understand the dielectric behavior of a material in different frequencies. This allows us to identify the like materials using a simple microwave planar resonator sensor.

#### 5.4.3 Validation of the designed resonator sensor

In this section of the experiment, the performance of the designed resonator sensor will be validated experimentally. The designed microwave sensor used for sensing solid samples to characterize the sensor has been used for this experiment. A new microchannel was 3D-printed to sense liquid samples where two different paths have been designed. A straight path was considered to flow the liquid metal through, and the U-shaped path was made for the liquid samples to flow. Inlet and outlet tubes were connected to the U-shaped path to allow the liquid samples to pass. The channel was correctly aligned with the microwave sensor. A VNA was connected to the resonator ports to record the transmitted power ( $S_{21}$ ). The experimental setup and the 3D printed microchannel for this experiment are presented in Figure 5.19.

Initially, four different positions have been marked in the microchannel using a black marker to limit the liquid metal position. Hydrocal 2400 oil

#### 5.4. Experimental setup and measurement discussion

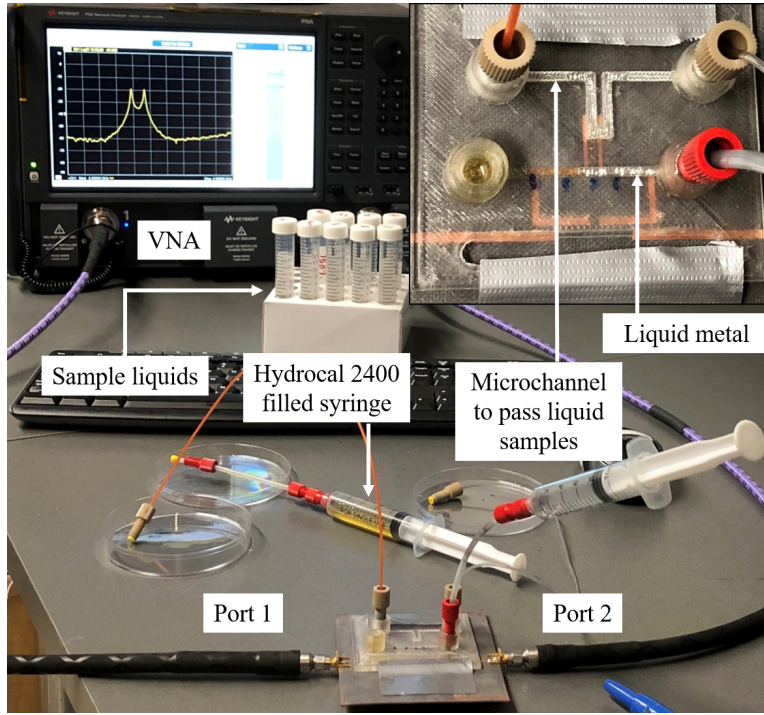


Figure 5.19: Experimental setup of the designed sensor used for sensing liquid samples of pure methanol, pure ethanol, 81% ethanol-water and 83% IPA-water solutions at different resonant frequencies.

was initially pushed through the microchannel to lubricate the tube and the channel using an mm syringe. Galinstan was pushed next through the microchannel till the second mark, which covers half of the gap and indicates a resonant frequency of 2.817 GHz. Each of the sample liquids has been pushed through the inlet tube through the channel, and the responses are recorded through the VNA. The channel and the tube were cleaned properly by flowing water each time before testing different liquid samples. Each sample reading has been taken three times to validate the response. Following the same procedure, Galinstan was pushed to two other marked locations, which indicate a resonant frequency of 2.719 GHz and 2.685 GHz, respectively. The sample liquids have been tested about both the resonant frequencies, and the results were recorded.

5.4. Experimental setup and measurement discussion

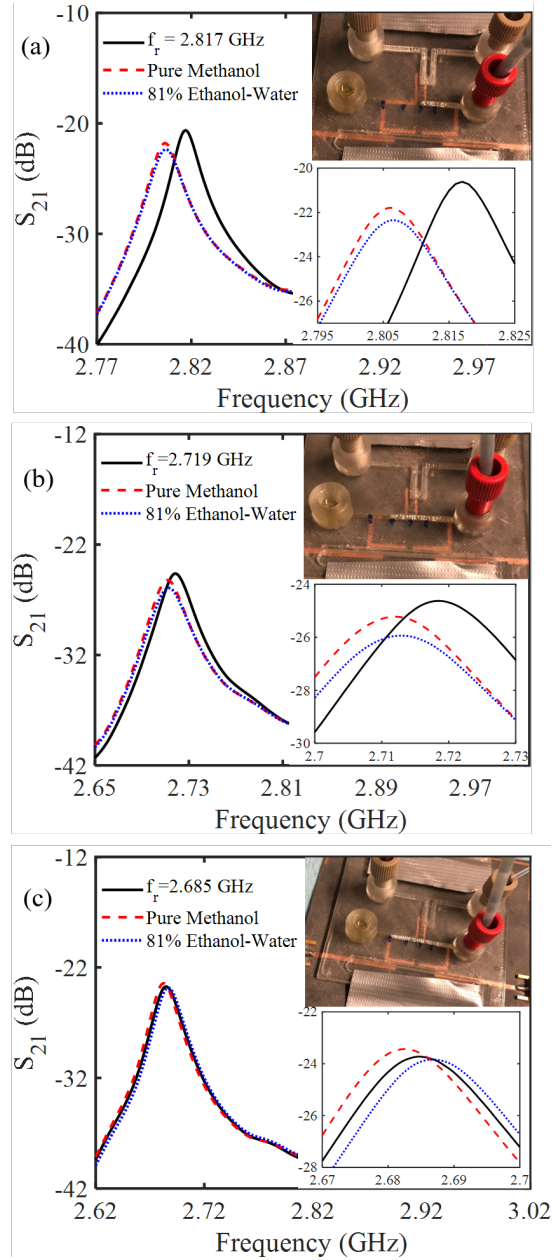


Figure 5.20: Measured frequency shift due to the presence of pure methanol and 81% ethanol-water at resonant frequencies of (a) 2.817 GHz, (b) 2.719 GHz, and (c) 2.685 GHz. The corresponding liquid metal position and frequency shifts are shown in the top right inset and bottom right inset, respectively.

5.4. Experimental setup and measurement discussion

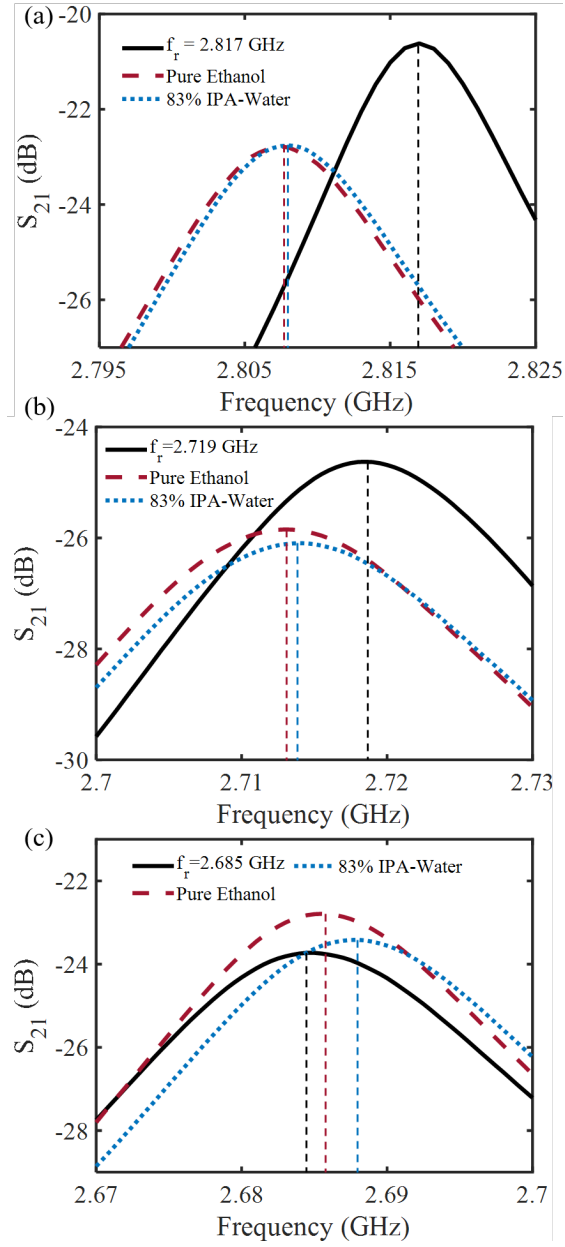


Figure 5.21: Measured frequency shift due to the presence of pure ethanol and 83% ethanol-water at resonant frequencies of (a) 2.817 GHz, (b) 2.719 GHz and (c) 2.685 GHz.

#### 5.4. Experimental setup and measurement discussion

Sample liquids of pure methanol, pure ethanol, 81% ethanol-water, and 83% IPA-water solutions were prepared for testing. Each of the sample liquids were moved into the channel in reference to the new liquid metal locations and resonant frequencies, and the  $S_{21}$  responses are recorded in the VNA. The channel and the tube were cleaned by forcing air through the channel and then allowing 5 minutes of drying before testing the next liquid samples. Each sample reading was taken three times to validate the response.

The measured response of pure methanol was compared with the response of 81% ethanol-water. In contrast, pure ethanol was compared with 83% IPA-water. The measured resonant frequencies achieved by positioning different amounts of liquid metal and the impact of sample liquids (pure methanol and 81% ethanol-water) at those resonant frequencies have been presented in Figure 5.20. The measured resonant frequencies are 2.817 GHz, 2.719 GHz, and 2.685 GHz. The resonant frequency shifts due to the presence of sample liquids (pure methanol and 81% ethanol-water) inside the microchannel are presented in Figure 5.20(a), 5.20(b) and 5.20(c), respectively. The liquid metal position has been shown in the top right inset, and magnification of the frequency shifts has been presented in the bottom right inset of Figure 5.20. Similarly, in Figure 5.21, the transmitted power ( $S_{21}$ ) due to the presence of sample liquids of pure ethanol and 83% IPA-water at different resonant frequencies have been presented. Figure 5.21(a), 5.21(b) and 5.21(c) indicates the response at resonant frequency of 2.817, 2.719 and 2.685 GHz, respectively. From Figure 5.20 and 5.21, it is evident that the liquid samples have higher sensitivity at the higher resonant frequency (2.817 GHz) compared to the lower resonant frequency of 2.685 GHz, just like in the solid sample tests presented in section 5.4.1.

The frequency differences due to the presence of liquid samples in different resonant frequencies were calculated and presented in TABLE 5.3.

Table 5.3: Measured frequency difference due to sample liquids presence in microfluidic channel in different resonant frequencies.

Test sample liquids	Frequency differences, $\Delta f$ (MHz), when		
	$f_r=2.817$ GHz	$f_r=2.719$ GHz	$f_r=2.685$ GHz
Pure Methanol	11.0	6.5	3.0
81% Ethanol-water	11.0	5.5	2.0
Pure Ethanol	9.0	5.5	0.5
83% IPA-water	9.0	4.5	3.0

The measured frequency difference of pure methanol and 81% ethanol-water was found 11 MHz when the resonant frequency was set to 2.817 GHz. So, at 2.817 GHz frequency, the sample liquids cannot be distinguished since both samples provide the same frequency difference. The resonant frequency was tuned to 2.719 GHz by adjusting the volume of liquid metal inside the microchannel. The tested samples, pure methanol, and 81% ethanol-water, provide frequency differences of 6.5 MHz and 5.5 MHz, respectively when sensing at 2.719 GHz of frequency. The samples can be identified by looking at their presented frequency difference. Similarly, the resonant frequency was shifted to 2.685 GHz, and the provided sample response helped to distinguish between the samples.

Moreover, in pure ethanol and 83% IPA-water solution, the measured frequency differences are similar at the frequency 2.817 GHz, and frequency differences are dissimilar in other frequencies like 2.719 GHz and 2.685 GHz. Other resonant frequencies can also be set for interest by adjusting the amount of liquid metal volume inside the microchannel to achieve the required selectivity. Therefore, measuring the frequency difference at multiple, easily tuned resonant frequencies can be effectively used to distinguish between similar permittivity samples. The presented approach successfully demonstrated a potential solution to address this issue by combining high resolution and sensitive resonant-based solutions with a spectroscopy method of sweeping the resonant frequency.

## 5.5 Chapter summary

Sensing materials over a continuous wideband frequency enables studying materials in more detail or investigating attractive surface or high-frequency properties. A microwave resonator sensor with a matching microfluidic channel was designed with sensitivities ranging from 36 to 6 MHz per unit  $\epsilon$  depending on the state of the resonator. Additionally, while permittivity is a unique material property, mixtures and compounds may combine to have a non-unique permittivity at certain frequencies. The development of a frequency-tunable microwave resonator sensor has overcome this by utilizing liquid metal to allow the resonator to operate at multiple frequencies between 2.1 and 2.8 GHz. The presented dielectric probe measurements specified the intercept points of the relative permittivity of two different liquid samples. The intercept points from the probe measurement explained the identical dielectric permittivity of liquid samples at a frequency. Sensing these materials using a resonator sensor operating at that

frequency will not help distinguish between the samples, and this clearly demonstrated the challenges in microwave resonator sensors.

The sensor operated with a microfluidic channel that could introduce a controlled amount of liquid metal to increase the overall capacitive loading of the resonator circuit, adjusting the resonant frequency accordingly. With HFSS simulations and dielectric probe measurements, the sensor was developed to selectively identify specific standard liquid mixtures of ethanol, methanol, isopropanol, and water. Experimental results confirmed that sensing at 2.817 GHz was unable to differentiate the two materials, but selectivity was achieved by tuning the sensor to 2.719 and 2.685 GHz. Identical dielectric properties of mixtures could be challenging to predict and untangle in industrial or technical sensing. However, with tunable frequencies, it becomes possible to quickly and easily obtain spectroscopic microwave data to selectively identify materials. The presented results in table 5.3 demonstrate a successful approach towards a potential solution to address this issue challenge by combining high resolution and sensitive resonant-based solutions with a spectroscopy method of sweeping the resonant frequency.

## Chapter 6

# Conclusion and Future Investigations

### 6.1 Thesis outcome and conclusion

The main intention of this thesis is to design and develop a planar resonant-based spectroscopy technique that can be employed in sensing materials in microwave sensor technology. The previously reported spectroscopy-based methods perform well towards detecting and characterizing materials in multiple frequencies. However, due to wideband performance and less accuracy of the spectroscopy method, the application scope is limited. The combination of resonant-based microwave sensors and the presented wideband continuous tunability technique based on liquid metal made it possible to achieve highly accurate and wideband frequency tuning in a compact design. The operating theory behind this work was investigated, and a successful potential approach to developing resonant-based spectroscopy was presented in this thesis.

A wideband continuously tunable planar microwave resonator over a frequency spectrum was developed by integrating microwave planar resonator and liquid metal with a 3D printed microfluidic channel. The developed tunable resonator was utilized as a tool towards an approach to detect materials of similar dielectric properties in planar sensor technology. The conventional split ring resonator was modified into a highly coupled resonator structure to create higher electromagnetic interaction. Among all the readily available liquid metals, Galinstan was chosen to use for this investigation because of its non-toxicity, high electrical conductivity, and environmental compatibility. A 3D printed microchannel lowers the cost and reduces the complexity of design techniques and rapid access to the product. The designed resonator structure's performance for a different amount of liquid metal volume inside the fluidic channel was validated by comparing the measured results with the structure simulation result and presented in subsection 4.3.1. The study shows the great potential of designing SRR sensors with a tunable

frequency, making a microwave frequency spectroscopy moving forward to solve the selectivity challenge in microwave planar resonator sensors.

In order to enable material sensing, traces of interdigitated capacitive structure was integrated with the designed structure. The designed sensor structure's performance was characterized by testing the standard solid samples of different permittivity and loss tangent. A clear concept of the problem was addressed in subsection 5.1 by using the Debye model, and pure liquids and mixtures that show similar dielectric behavior were determined by standard probe measurements. The sample liquids of similar dielectric properties were tested in different frequencies, and the measured results presented in table 5.3 shows multi-phase material identification. Finally, the investigation throughout this thesis successfully demonstrated the presented approach as a potential solution to distinguish between samples of identical dielectric properties in microwave sensor technology.

The outcomes throughout the investigation of this thesis are as follows:

- A wideband continuous frequency tuning of 1.05 GHz with a fairly constant amplitude and a quality factor of 70 ( $\pm 5$ ) was achieved.
- While characterizing the designed resonant structure, the resonator's sensitivity ranging from 36 to 6 MHz per unit  $\epsilon$  was observed depending on the state of the resonator. The sensor structure demonstrates different sensitivity at different resonant frequencies, adjusted by the liquid metal length inside the microfluidic channel.
- The coaxial probe experiment identifies that 81% ethanol-water solution and pure methanol exhibit the same frequency difference of 11 MHz at 2.817 GHz of frequency and 83% IPA-water and pure ethanol exhibits the same frequency difference of 9 MHz at 2.817 GHz of frequency, indicating that the samples could not be distinguished using a resonator operating at 2.817 GHz.
- A multi-phase material detection was achieved by using the resonant based spectroscopy technique of sweeping the resonant frequency.

## 6.2 Future work

The presented thesis utilizes the concept of wideband frequency tunability of the designed resonant structure based on liquid metal as a tool to develop planar resonant-based spectroscopy. Moreover, several topics have

been highlighted as potential future work during the thesis investigation. The suggestions for extending this research are as follows:

- In this thesis, frequency tunability using a liquid metal enabled microwave ring resonator is implied in a passive microwave resonator. A potential future work can be an investigation of the concept in active microwave resonators.
- The wideband and low-loss tuning performance of the liquid metal integrated planar microwave resonator sensors encourages the further expansion of liquid metal adaptation to the development of tunable antenna sensors.
- Two highly coupled resonators have been designed for achieving tunability in this research, and the achieved frequency tuning was 1.05 GHz. Different resonant structures can be explored in the future to achieve a broader range of frequency tuning.
- The mathematical model that can calculate the amount of liquid metal volume to achieve a specific resonant frequency is not developed here since the primary goal of this thesis is to develop the concept of a continuously tunable microwave resonator. In that case, developing a mathematical model to calculate the amount of liquid metal volume to obtain a particular frequency can be a potential future study.
- During an investigation of this thesis, a higher volume of liquid metal over the trace increases the capacitive coupling through the substrate's ground layer, introducing a loss mechanism that results in signal loss. In the future, it can be investigated to eliminate this issue of signal loss and can achieve a consistent signal strength.

# Bibliography

- [1] Elprocus, “Microwaves Technology Basics — Effects — Applications and Advantages.” [Online]. Available: <https://www.elprocus.com/microwaves-basics-applications-effects/> → pages 5
- [2] W. excellence limited, “Microwave Technology - CableFree,” 2020. [Online]. Available: <https://www.cablefree.net/wirelesstechnology/microwave/> → pages 6
- [3] M. Golio and J. Golio, *RF and Microwave Circuits, Measurements, and Modeling*, M. Golio and J. Golio, Eds. Taylor & Francis Group, LLC, 2008. → pages 6
- [4] S. Ullah, C. Ruan, M. S. Sadiq, T. Ul Haq, and W. He, “High efficient and ultra wide band monopole antenna for microwave imaging and communication applications,” *Sensors (Switzerland)*, vol. 20, no. 1, pp. 1–11, 2020. → pages 6
- [5] Y. Sun, F. Dang, C. Yuan, J. He, Q. Zhang, and X. Zhao, “A Beam-Steerable Lens Antenna for Ku -Band High-Power Microwave Applications,” *IEEE Transactions on Antennas and Propagation*, vol. 68, no. 11, pp. 7580–7583, 2020. → pages 6
- [6] L. Gil-Flores, M. D. Salvador, F. L. Penaranda-Foix, A. Dalmau, A. Fernández, and A. Borrell, “Tribological and wear behaviour of alumina toughened zirconia nanocomposites obtained by pressureless rapid microwave sintering,” *Journal of the Mechanical Behavior of Biomedical Materials*, vol. 101, no. August 2019, p. 103415, 2020. [Online]. Available: <https://doi.org/10.1016/j.jmbbm.2019.103415> → pages 6
- [7] D. Belamri, A. Harabi, N. Karbouaa, and N. Benyahia, “The effect of KF on the structural evolution of natural hydroxyapatite during conventional and microwave sintering,” *Ceramics International*, vol. 46, no. 1, pp. 1189–1194, 2020. [Online]. Available: <https://doi.org/10.1016/j.ceramint.2019.09.091> → pages

- [8] E. A. Anli, "Possibilities for using microwave-vacuum drying in Lor cheese production," *International Dairy Journal*, vol. 102, p. 104618, 2020. [Online]. Available: <https://doi.org/10.1016/j.idairyj.2019.104618> → pages
- [9] M. Nadeem, E. Ul Haq, F. Ahmed, M. Asif Rafiq, G. Hameed Awan, and M. Zain-ul Abdein, "Effect of microwave curing on the construction properties of natural soil based geopolymer foam," *Construction and Building Materials*, vol. 230, p. 117074, 2020. [Online]. Available: <https://doi.org/10.1016/j.conbuildmat.2019.117074> → pages
- [10] D. Agrawal, "Microwave sintering of metal powders," *Advances in Powder Metallurgy: Properties, Processing and Applications*, pp. 361–379, 2013. → pages 6
- [11] X. Lin, Y. Chen, Z. Gong, B. C. Seet, L. Huang, and Y. Lu, "Ultrawideband Textile Antenna for Wearable Microwave Medical Imaging Applications," *IEEE Transactions on Antennas and Propagation*, vol. 68, no. 6, pp. 4238–4249, 2020. → pages 6
- [12] F. Fiore, V. Stoia, and F. Somma, "Surgical recurrence of solitary fibrous tumor of the pleura treated with microwave (MW) thermoablation: A case report," *Thoracic Cancer*, vol. 11, no. 2, pp. 443–446, 2020. → pages
- [13] K. Imajo, Y. Ogawa, M. Yoneda, S. Saito, and A. Nakajima, "A review of conventional and newer generation microwave ablation systems for hepatocellular carcinoma," *Journal of Medical Ultrasonics*, vol. 47, no. 2, pp. 265–277, 2020. [Online]. Available: <https://doi.org/10.1007/s10396-019-00997-5> → pages 6
- [14] Y. Wang, Z. Ye, C. Si, and Y. Ying, "Monitoring of Escherichia coli O157:H7 in food samples using lectin based surface plasmon resonance biosensor," *Food Chemistry*, vol. 136, no. 3-4, pp. 1303–1308, 2013. [Online]. Available: <http://dx.doi.org/10.1016/j.foodchem.2012.09.069> → pages 6
- [15] S. Taleb, L. Merad, S. M. Meriah, S. M. Chouiti, and M. Boussahla, "Tumor detection by microwave radar imaging system," *2017 Seminar on Detection Systems Architectures and Technologies, DAT 2017*, pp. 0–4, 2017. → pages 6

- [16] M. E. Bialkowski, "Ultra wideband microwave system with novel image reconstruction strategies for breast cancer detection," *European Microwave Week 2010, EuMW2010: Connecting the World, Conference Proceedings - European Microwave Conference, EuMC 2010*, no. September, pp. 537–540, 2010. → pages 6
- [17] X. Wan, D. Yang, M. Cai, S. Han, S. Wu, and W. Hao, "The latest research status and prospect on microwave technology for monitoring concerned brain activity," *2015 IEEE International Conference on Mechatronics and Automation, ICMA 2015*, pp. 297–302, 2015. → pages 6
- [18] R. McMillan, N. Currie, D. Ferris, and M. Wicks, "Concealed weapon detection using microwave and millimeter wave sensors," in *ICMMT'98. 1998 International Conference on Microwave and Millimeter Wave Technology. Proceedings (Cat. No.98EX106)*. Publishing House of Electron. Ind, 1998, pp. 1–4. [Online]. Available: <http://ieeexplore.ieee.org/document/768213/> → pages 6
- [19] P. Singh, S. K. Chaulya, V. K. Singh, and T. N. Ghosh, "Sensor for Eliminating Illegal Mine Activities," *2018 3rd International Conference on Microwave and Photonics (ICMAP)*, no. Icmaph, pp. 1–5, 2018. → pages 6
- [20] D. Pozar, *Microwave Engineering*. John Wiley & Sons, Inc., 2012, no. 1. → pages 7, 8, 9, 20, 21, 22, 23
- [21] F. Martín, *Artificial Transmission Lines for RF and Microwave Applications*. John Wiley & Sons, Inc., 2015. → pages 7, 8, 9
- [22] Michael Steer, *Microwave and RF Design: Transmission Lines*, 3rd ed. NC State University, 2019, vol. 2. → pages 7, 8, 9
- [23] The Altium Team, "Stripline vs Microstrip: PCB Routing Differences and Guidelines," p. 1, 2017. → pages 9
- [24] Z. T. Bergstedt, "Differential Launch Structures and Common Mode Filters for Planar Transmission Lines," Ph.D. dissertation, Rose-Hulman Institute of Technology, 2018. → pages 9
- [25] A. Maleki Gargari, M. H. Zarifi, and L. Markley, "Passive Matched Mushroom Structure for a High Sensitivity Low Profile Antenna-Based Material Detection System," *IEEE Sensors Journal*, vol. 19, no. 15, pp. 6154–6162, 2019. → pages 10

- 
- [26] M. H. Zarifi and M. Daneshmand, “High-Resolution RFID Liquid Sensing Using a Chipless Tag,” *IEEE Microwave and Wireless Components Letters*, vol. 27, no. 3, pp. 311–313, 2017. → pages 10, 68, 71
- [27] —, “Monitoring Solid Particle Deposition in Lossy Medium Using Planar Resonator Sensor,” *IEEE Sensors Journal*, vol. 17, no. 23, pp. 7981–7989, 2017. → pages
- [28] M. H. Zarifi, H. Sadabadi, S. H. Hejazi, M. Daneshmand, and A. Sanati-Nezhad, “Noncontact and Nonintrusive Microwave-Microfluidic Flow Sensor for Energy and Biomedical Engineering,” *Scientific Reports*, vol. 8, no. 1, pp. 1–10, 2018. [Online]. Available: <http://dx.doi.org/10.1038/s41598-017-18621-2> → pages 10
- [29] B. Wiltshire, K. Mirshahidi, K. Golovin, and M. H. Zarifi, “Robust and sensitive frost and ice detection via planar microwave resonator sensor,” *Sensors and Actuators, B: Chemical*, vol. 301, no. August, pp. 2–6, 2019. → pages 10, 42
- [30] A. Rydosz, E. Maciak, K. Wincza, and S. Gruszczynski, “Microwave-based sensors with phthalocyanine films for acetone, ethanol and methanol detection,” *Sensors and Actuators, B: Chemical*, vol. 237, pp. 876–886, 2016. [Online]. Available: <http://dx.doi.org/10.1016/j.snb.2016.06.168> → pages 10
- [31] C. H. N. Reimann, B. Bazrafshan, M. Schubler, S. Schmidt, C. Schuster, F. Hubner, T. J. Vogl, and R. Jakoby, “A dual-mode coaxial slot applicator for microwave ablation treatment,” *IEEE Transactions on Microwave Theory and Techniques*, vol. 67, no. 3, pp. 1255–1264, 2019. → pages 10
- [32] R. V. Haro-Báez, J. Córcoles, J. A. Ruiz-Cruz, J. R. Montejo-Garai, and J. M. Rebollar, “Higher-Order Mode Electromagnetic Analysis of a Material Sample between Two Flanged Coaxial Probes for Broadband Modelling of Dielectric Measurement Setups,” *Advances in Mathematical Physics*, vol. 2019, no. i, 2019. → pages 10
- [33] Samuel J.Ling, Jeff Sanny, and William Moebs, *University physics*. Openstax, 2018, vol. 2. → pages 10, 11

- [34] L.F.Chen, C. Ong, C.P.Neo, V.V.Varadan, and V.K. Varadan, *Microwave electronics*. John Wiley & Sons Ltd., 2004. → pages 11, 12
- [35] B. Lambert, “Mauritz - Dielectric Spectroscopy.” [Online]. Available: <http://www.psrc.usm.edu/mauritz/dilect.html> → pages 12
- [36] Kuek Chee Yaw, “Measurement of Dielectric Material Properties,” 2012. → pages 13, 14, 15, 16, 17, 18, 41
- [37] F. Costa, M. Borgese, M. Degiorgi, and A. Monorchio, “Electromagnetic characterisation of materials by using transmission/reflection (T/R) devices,” *Electronics (Switzerland)*, vol. 6, no. 4, 2017. → pages 14
- [38] M. Maleki, S. H. Mohseni Armaki, and E. Hamidi, “Study of ferrite material characterization using transmission line model,” *Microwave and Optical Technology Letters*, vol. 60, no. 12, pp. 2876–2880, 2018. → pages 14
- [39] A. Tamer, F. Karadağ, E. Ünal, Y. I. Abdulkarim, L. Deng, O. Altintas, M. Bakır, and M. Karaaslan, “Metamaterial based sensor integrating transmission line for detection of branded and unbranded diesel fuel,” *Chemical Physics Letters*, vol. 742, no. February, p. 137169, 2020. [Online]. Available: <https://doi.org/10.1016/j.cplett.2020.137169> → pages 14
- [40] C. K. Lee, S. Zhang, S. S. Bukhari, D. Cadman, J. C. Vardaxoglou, and W. G. Whittow, “Complex Permittivity Measurement System for Solid Materials Using Complementary Frequency Selective Surfaces,” *IEEE Access*, vol. 8, pp. 7628–7640, 2020. → pages 14
- [41] M. S. Venkatesh and G. S. Raghavan, “An overview of dielectric properties measuring techniques,” *Canadian Biosystems Engineering / Le Genie des biosystems au Canada*, vol. 47, 2005. → pages 14, 15, 17, 41
- [42] Keysight Technologies, “Basics of Measuring the Dielectric Properties of Materials.” → pages 14, 15, 16, 17, 86
- [43] J. C. Santos, M. H. Dias, A. P. Aguiar, I. Borges, and L. E. Borges, “Using the Coaxial Probe Method for permittivity measurements of liquids at high temperatures,” *Journal of Microwaves and Optoelectronics*, vol. 8, no. 1, pp. 78–91, 2009. → pages 15

- [44] A. Mavrovic, J. B. Madore, A. Langlois, A. Royer, and A. Roy, “Snow liquid water content measurement using an open-ended coaxial probe (OECF),” *Cold Regions Science and Technology*, vol. 171, p. 102958, 2020. [Online]. Available: <https://doi.org/10.1016/j.coldregions.2019.102958> → pages 15
- [45] G. Maenhout, T. Markovic, I. Ocket, and B. Nauwelaers, “Effect of open-ended coaxial probe-to-tissue contact pressure on dielectric measurements,” *Sensors (Switzerland)*, vol. 20, no. 7, pp. 1–13, 2020. → pages 15
- [46] A. Kraszewski, “Microwave Aquametry—A Review,” *Journal of Microwave Power*, vol. 15, no. 4, pp. 209–220, 1980. → pages 16
- [47] N. Vohra, L. R. Rodriguez-Aguilar, J. S. Batista, and M. El-Shenawee, “Free-Space Characterization of Radar Absorbing Non-Magnetic Materials in the W-Band,” *2020 94th ARFTG Microwave Measurement Conference: RF to Millimeter-Wave Measurement Techniques for 5G and Beyond, ARFTG 2020*, pp. 0–3, 2020. → pages 17
- [48] D. K. Ghodgaonkar, V. V. Varadan, and V. K. Varadan, “A Free-Space Method for Measurement of Dielectric Constants and Loss Tangents at Microwave Frequencies,” *IEEE Transactions on Instrumentation and Measurement*, vol. 38, no. 3, pp. 789–793, 1989. → pages
- [49] —, “Free-Space Measurement of Complex Permittivity and Complex Permeability of Magnetic Materials at Microwave Frequencies,” *IEEE Transactions on Instrumentation and Measurement*, vol. 39, no. 2, pp. 387–394, 1990. → pages
- [50] S. Trabelsi and S. O. Nelson, “Free-space measurement of dielectric properties of moist granular materials at microwave frequencies,” *Conference Record - IEEE Instrumentation and Measurement Technology Conference*, vol. 1, pp. 518–523, 2003. → pages
- [51] F. H. Wee, P. J. Soh, A. H. Suhaizal, H. Nornikman, and A. A. Ezzanudin, “Free space measurement technique on dielectric properties of agricultural residues at microwave frequencies,” *SBMO/IEEE MTT-S International Microwave and Optoelectronics Conference Proceedings*, no. I, pp. 183–187, 2009. → pages 17
- [52] E. Håkansson, A. Amiet, and A. Kaynak, “Dielectric characterization of conducting textiles using free space transmission measurements:

- Accuracy and methods for improvement,” *Synthetic Metals*, vol. 157, no. 24, pp. 1054–1063, 2007. → pages 17
- [53] T. R. Jones, M. H. Zarifi, and M. Daneshmand, “Miniaturized Quarter-Mode Substrate Integrated Cavity Resonators for Humidity Sensing,” *IEEE Microwave and Wireless Components Letters*, vol. 27, no. 7, pp. 612–614, 2017. → pages 17
- [54] K. Saeed, R. D. Pollard, and I. C. Hunter, “Substrate integrated waveguide cavity resonators for complex permittivity characterization of materials,” *IEEE Transactions on Microwave Theory and Techniques*, vol. 56, no. 10, pp. 2340–2347, 2008. → pages 18, 19
- [55] W. Tian, J. Sun, L. Xu, S. Sun, H. Che, D. Li, W. Yang, and F. R. D. Sousa, “Investigation of granule moisture measurement by a microwave resonant cavity sensor,” *I2MTC 2019 - 2019 IEEE International Instrumentation and Measurement Technology Conference, Proceedings*, vol. 2019-May, 2019. → pages 18
- [56] J. Baker-jarvis, R. G. Geyer, J. H. Grosvenor, M. D. Janezic, C. A. Jones, B. Riddle, and C. M. Weil, “Dielectric Characterization of Low-loss Materials,” *IEEE Transactions on Dielectrics and Electrical Insulation*, vol. 5, no. 4, pp. 571–577, 1998. → pages 18
- [57] M. H. Zarifi, S. Deif, M. Abdolrazzaghi, B. Chen, D. Ramsawak, M. Amyotte, N. Vahabisani, Z. Hashisho, W. Chen, and M. Daneshmand, “A Microwave Ring Resonator Sensor for Early Detection of Breaches in Pipeline Coatings,” *IEEE Transactions on Industrial Electronics*, vol. 65, no. 2, pp. 1626–1635, feb 2018. [Online]. Available: <http://ieeexplore.ieee.org/document/7997779/> → pages 19, 20, 28
- [58] M. Abdolrazzaghi, M. H. Zarifi, and M. Daneshmand, “Sensitivity enhancement of split ring resonator based liquid sensors,” *Proceedings of IEEE Sensors*, pp. 1–3, 2017. → pages
- [59] M. H. Zarifi, P. Shariaty, M. Abdolrazzaghi, Z. Hashisho, and M. Daneshmand, “Particle size characterization using a high resolution planar resonator sensor in a lossy medium,” *Sensors and Actuators, B: Chemical*, vol. 234, pp. 332–337, 2016. [Online]. Available: <http://dx.doi.org/10.1016/j.snb.2016.04.130> → pages

- [60] M. Hossein, M. Rahimi, and M. Daneshmand, “Microwave ring resonator-based non-contact interface sensor for oil sands applications,” *Sensors and Actuators B : Chemical*, vol. 224, pp. 632–639, 2016. → pages
- [61] K. Grenier, D. Dubuc, P. E. Poleni, M. Kumemura, H. Toshiyoshi, T. Fujii, and H. Fujita, “Integrated broadband microwave and microfluidic sensor dedicated to bioengineering,” *IEEE Transactions on Microwave Theory and Techniques*, vol. 57, no. 12, pp. 3246–3253, 2009. → pages
- [62] M. H. Zarifi, T. Thundat, and M. Daneshmand, “High resolution microwave microstrip resonator for sensing applications,” *Sensors and Actuators, A: Physical*, vol. 233, pp. 224–230, 2015. → pages 19, 20
- [63] M. Krawczyk, “Microstrip resonators for circuit quantum electrodynamics,” Ph.D. dissertation, Technische Universität München, 2011. [Online]. Available: <https://www.wmi.badw.de/publications/theses/Krawczyk{-}Master{-}Thesis{-}2011.pdf> → pages 20, 21, 23
- [64] T. P. Orlando, K. A. Delin, and C. J. Lobb, “Foundations of Applied Superconductivity ,” *Physics Today*, vol. 44, no. 6, pp. 109–109, 1991. → pages 21
- [65] Frank Gustrau, *RF and Microwave Engineering: Fundamentals of Wireless Communications*. John Wiley & Sons Ltd, 2012, vol. 66. → pages 22, 23
- [66] T. Niemczyk, F. Deppe, H. Huebl, E. P. Menzel, F. Hocke, M. J. Schwarz, J. J. Garcia-Ripoll, D. Zueco, T. Hümmer, E. Solano, A. Marx, and R. Gross, “Circuit quantum electrodynamics in the ultrastrong-coupling regime,” *Nature Physics*, vol. 6, no. 10, pp. 772–776, 2010. → pages 23
- [67] M. Göppl, A. Fragner, M. Baur, R. Bianchetti, S. Filipp, J. M. Fink, P. J. Leek, G. Puebla, L. Steffen, and A. Wallraff, “Coplanar waveguide resonators for circuit quantum electrodynamics,” *Journal of Applied Physics*, vol. 104, no. 11, pp. 1–8, 2008. → pages 23, 24
- [68] P. Clarricoats, *Foundations for Microwave Engineering*. IEEE Press, 1967, vol. 13, no. 1. [Online]. Available: <https://digital-library.theiet.org/content/journals/10.1049/ep.1967.0023> → pages 23

- [69] T. Niemczyk, “From strong to ultrastrong coupling in circuit QED architectures,” *WMI PhD thesis*, 2011. → pages 23
- [70] B. D. Wiltshire and M. H. Zarifi, “3-D Printing Microfluidic Channels With Embedded Planar Microwave Resonators for RFID and Liquid Detection,” *IEEE Microwave and Wireless Components Letters*, vol. 29, no. 1, pp. 65–67, jan 2019. → pages 25, 39
- [71] D. G. Rabus, *Integrated Ring Resonators*, ser. Springer Series in Optical Sciences. Berlin, Heidelberg: Springer Berlin Heidelberg, 2007, vol. 127. [Online]. Available: <http://link.springer.com/10.1007/978-3-540-68788-7> → pages 25
- [72] E. Iannone, *Microwave and RF Engineering*. A John Wiley and Sons, Ltd, Publication, 2010. → pages 25
- [73] E. Notes, “Quality Factor — Q Factor Formula — Electronics Notes.” [Online]. Available: <https://www.electronics-notes.com/articles/basic{-}concepts/q-quality-factor/basics-tutorial-formula.php> → pages 26
- [74] N. Pekçokgüler, G. Dündar, H. Torun, and A. D. Yalçinkaya, “A novel equivalent circuit model for split ring resonator with an application of low phase noise reference oscillator,” *Integration*, vol. 61, no. December, pp. 160–166, 2018. → pages 26
- [75] T. Weiland, R. Schuhmann, R. B. Greigor, C. G. Parazzoli, A. M. Vetter, D. R. Smith, D. C. Vier, and S. Schultz, “Ab initio numerical simulation of left-handed metamaterials: Comparison of calculations and experiments,” *Journal of Applied Physics*, vol. 90, no. 10, pp. 5419–5424, 2001. → pages 27
- [76] C. C. Chen, A. Ishikawa, Y. H. Tang, M. H. Shiao, D. P. Tsai, and T. Tanaka, “Uniaxial-isotropic Metamaterials by Three-Dimensional Split-Ring Resonators,” *Advanced Optical Materials*, vol. 3, no. 1, pp. 44–48, 2015. → pages
- [77] B. Vasić, M. M. Jakovljević, G. Isić, and R. Gajić, “Tunable metamaterials based on split ring resonators and doped graphene,” *Applied Physics Letters*, vol. 103, no. 1, pp. 1–5, 2013. → pages 27
- [78] J. B. Pendry, A. J. Holden, D. J. Robbins, and W. J. Stewart, “Magnetism from conductors and enhanced nonlinear phenomena,” *IEEE*

- Transactions on Microwave Theory and Techniques*, vol. 47, no. 11, pp. 2075–2084, 1999. → pages 27
- [79] K. Chang and L. H. Hsieh, *Microwave ring circuits and related structures*, 2nd ed. A JOHN WILEY & SONS, INC., PUBLICATION, 2004, vol. 2. → pages 28, 54
- [80] S. S. Karthikeyan and M. Arulvani, “Double negative metamaterial design using open split ring resonator,” *TechSym 2010 - Proceedings of the 2010 IEEE Students’ Technology Symposium*, no. April, pp. 142–145, 2010. → pages 28
- [81] S. Mohammadi, A. V. Nadaraja, D. J. Roberts, and M. H. Zarifi, “Real-time and hazard-free water quality monitoring based on microwave planar resonator sensor,” *Sensors and Actuators, A: Physical*, vol. 303, no. October, 2020. → pages 28
- [82] M. Abdolrazzaghi, S. Khan, and M. Daneshmand, “A Dual-Mode Split-Ring Resonator to Eliminate Relative Humidity Impact,” *IEEE Microwave and Wireless Components Letters*, vol. 28, no. 10, pp. 939–941, 2018. → pages 29
- [83] A. Kabiri, “Artificial Magnetic Materials : Limitations , Synthesis and Possibilities by,” Ph.D. dissertation, University of Waterloo, 2010. → pages 29
- [84] R. A. Awang, “Flexible and Tunable Split Ring Resonators,” Ph.D. dissertation, RMIT University, 2016. → pages 30, 31, 32
- [85] K. Aydin and E. Ozbay, “Capacitor-loaded split ring resonators as tunable metamaterial components,” *Journal of Applied Physics*, vol. 101, no. 2, pp. 1–5, 2007. → pages 30, 31
- [86] T. Hand and S. Cummer, “Characterization of tunable metamaterial elements using MEMS switches,” *IEEE Antennas and Wireless Propagation Letters*, vol. 6, pp. 401–404, 2007. → pages 30
- [87] T. Nesimoglu and C. Sabah, “A frequency tunable metamaterial resonator using varactor diodes,” *Mediterranean Microwave Symposium*, vol. 0, pp. 0–3, 2016. → pages 30, 31
- [88] E. Erdil, K. Topalli, M. Unlu, O. A. Civi, and T. Akin, “Frequency tunable microstrip patch antenna using RF MEMS technology,” *IEEE*

- Transactions on Antennas and Propagation*, vol. 55, no. 4, pp. 1193–1196, 2007. → pages 31
- [89] Somarith Sam and S. Lim, “Tunable band-pass filters based on varactor-loaded complementary split-ring resonators on half-mode substrate integrated waveguide,” *Microwave and Optical Technology Letters*, vol. 55, no. 11, pp. 2562–2568, 2013. → pages 30
- [90] I. Gil, J. Bonache, J. García-García, and F. Martín, “Tunable metamaterial transmission lines based on varactor-loaded split-ring resonators,” *IEEE Transactions on Microwave Theory and Techniques*, vol. 54, no. 6, pp. 2665–2674, 2006. → pages
- [91] A. Velez, J. Bonache, and F. Martin, “Varactor-loaded complementary split ring resonators (VLCSSR) and their application to tunable metamaterial transmission lines,” *IEEE Microwave and Wireless Components Letters*, vol. 18, no. 1, pp. 28–30, 2008. → pages
- [92] S. Zhu, D. G. Holtby, K. L. Ford, A. Tennant, and R. J. Langley, “Compact low frequency varactor loaded tunable SRR antenna,” *IEEE Transactions on Antennas and Propagation*, vol. 61, no. 4, pp. 2301–2304, 2013. → pages 30
- [93] H. Trabelsi and C. Cruchon, “A Varactor-Tuned Active Microwave Bandpass Filter,” pp. 231–232, 1992. → pages 31
- [94] S. R. Chandler, I. C. Hunter, and J. G. Gardiner, “Active Varactor Tunable Bandpass Filter,” *IEEE Microwave and Guided Wave Letters*, vol. 3, no. 3, pp. 70–71, 1993. → pages
- [95] C. Y. Chang and T. Itoh, “Microwave active filters based on coupled negative resistance method,” *IEEE Transactions on Microwave Theory and Techniques*, vol. 38, no. 12, pp. 1879–1884, 1990. → pages 31
- [96] D. Bouyge, A. Crunteanu, A. Pothier, P. O. Martin, P. Blondy, A. Velez, J. Bonache, J. C. Orlianges, and F. Martin, “Reconfigurable 4 pole bandstop filter based on RF-MEMS-loaded split ring resonators,” *IEEE MTT-S International Microwave Symposium Digest*, pp. 588–591, 2010. → pages 31, 32
- [97] B. Pradhan and B. Gupta, “Ka-Band Tunable Filter Using Metamaterials and RF MEMS Varactors,” *Journal of Microelectromechanical*

- Systems*, vol. 24, no. 5, pp. 1453–1461, oct 2015. [Online]. Available: <http://ieeexplore.ieee.org/document/7064731/> → pages 32
- [98] Y. Luo, Z. Han, K. Kikuta, T. Takahashi, A. Hirose, H. Fujita, and H. Toshiyoshi, “An active metamaterials antenna controlled by RF-MEMS switches,” *2015 Transducers - 2015 18th International Conference on Solid-State Sensors, Actuators and Microsystems, TRANSDUCERS 2015*, pp. 303–306, 2015. → pages
- [99] Z. Chen, X. Kan, Q. Yuan, T. Wang, J. Yang, and F. Yang, “A Switchable High-Performance RF-MEMS Resonator with Flexible Frequency Generations,” *Scientific Reports*, vol. 10, no. 1, pp. 1–15, 2020. [Online]. Available: <http://dx.doi.org/10.1038/s41598-020-61744-2> → pages 31
- [100] G. M. Rebeiz, I. C. Reines, M. A. El-Tanani, A. Grichener, K. Entesari, S. J. Park, and A. R. Brown, “Tuning in to RF MEMS,” *IEEE Microwave Magazine*, vol. 10, no. 6, pp. 55–72, 2009. → pages 32
- [101] P. W. Wong and I. Hunter, “Electronically Tunable Filters,” *IEEE Microwave Magazine*, vol. 10, no. 6, pp. 46–54, 2009. → pages 32
- [102] H. Maune, M. Jost, A. Wiens, C. Weickhmann, R. Reese, M. Nikfalazar, C. Schuster, T. Franke, W. Hu, M. Nickel, D. Kiene-mund, A. E. Prasetyadi, and R. Jakoby, “Tunable Microwave Component Technologies for SatCom-Platforms,” *Frequenz*, vol. 71, no. 3-4, pp. 129–142, 2017. → pages 32
- [103] I. Lockerbie and S. Kumar, “A Broadband Tunable Combline Filter Using Active Devices,” in *IEEE WESCANEX 93 Communications, Computers and Power in the Modern Environment - Conference Proceedings*, 1993, pp. 196–200. → pages 32
- [104] I. C. Hunter and S. R. Chandler, “Intermodulation distortion in active microwave filters,” *IEE Proceedings: Microwaves, Antennas and Propagation*, vol. 145, no. 1, pp. 7–12, 1998. → pages
- [105] C. Rauscher, “Varactor-tuned active notch filter with low passband noise and signal distortion,” *IEEE Transactions on Microwave Theory and Techniques*, vol. 49, no. 8, pp. 1431–1437, 2001. → pages 32
- [106] C.-h. Chen, S. Member, and D. Peroulis, “Liquid RF MEMS Wideband Reflective,” *IEEE Transactions on Microwave Theory and Techniques*, vol. 55, no. 12, pp. 2919–2929, 2007. → pages 33

- [107] Chung-Hao Chen and D. Peroulis, “A Ka-band waveguide water-based absorptive switch with an integrated micropump,” in *2008 IEEE MTT-S International Microwave Symposium Digest*. IEEE, jun 2008, pp. 185–188. [Online]. Available: <http://ieeexplore.ieee.org/document/4633134/> → pages 33
- [108] N. Vahabisani, S. Khan, and M. Daneshmand, “A K -Band Reflective Waveguide Switch Using,” *IEEE Antennas and Wireless Propagation Letters*, vol. 16, pp. 1788–1791, 2017. → pages 34
- [109] A. Pourghorban Saghati, J. Singh Batra, J. Kameoka, and K. Entesari, “Miniature and reconfigurable CPW folded slot antennas employing liquid-metal capacitive loading,” *IEEE Transactions on Antennas and Propagation*, vol. 63, no. 9, pp. 3798–3807, 2015. → pages 34, 38, 41, 42
- [110] H. K. Kim, D. Lee, and S. Lim, “Wideband-switchable metamaterial absorber using injected liquid metal,” *Scientific Reports*, vol. 6, no. July, pp. 1–11, 2016. [Online]. Available: <http://dx.doi.org/10.1038/srep31823> → pages 33
- [111] X. Huang, H. Yang, Z. Shen, J. Chen, H. Lin, and Z. Yu, “Water-injected all-dielectric ultra-wideband and prominent oblique incidence metamaterial absorber in microwave regime,” *Journal of Physics D: Applied Physics*, vol. 50, no. 38, 2017. → pages 33
- [112] D. Rodrigo, L. Jofre, and B. A. Cetiner, “Circular beam-steering reconfigurable antenna with liquid metal parasitics,” *IEEE Transactions on Antennas and Propagation*, vol. 60, no. 4, pp. 1796–1802, 2012. → pages 33, 35, 38
- [113] M. Li, B. Yu, and N. Behdad, “Liquid-tunable frequency selective surfaces,” *IEEE Microwave and Wireless Components Letters*, vol. 20, no. 8, pp. 423–425, 2010. → pages 33
- [114] K. J. Morton, K. Loutherbach, D. W. Inglis, O. K. Tsui, J. C. Sturm, S. Y. Chou, and R. H. Austin, “Hydrodynamic metamaterials: Micro-fabricated arrays to steer, refract, and focus streams of biomaterials,” *Proceedings of the National Academy of Sciences of the United States of America*, vol. 105, no. 21, pp. 7434–7438, 2008. → pages

- [115] T. S. Kasirga, Y. N. Ertas, and M. Bayindir, "Microfluidics for reconfigurable electromagnetic metamaterials," *Applied Physics Letters*, vol. 95, no. 21, pp. 2–5, 2009. → pages 33
- [116] S. Khan, N. Vahabisani, and M. Daneshmand, "A Fully 3-D Printed Waveguide and Its Application as Microfluidically Controlled Waveguide Switch," *IEEE Transactions on Components, Packaging and Manufacturing Technology*, vol. 7, no. 1, pp. 70–80, jan 2017. → pages 34
- [117] A. P. Saghati, Sina Baghbani Kordmahale, J. Kameoka, and K. Entesari, "A reconfigurable quarter-mode substrate integrated waveguide cavity filter employing liquid-metal capacitive loading," in *2015 IEEE MTT-S International Microwave Symposium*. IEEE, may 2015, pp. 1–3. → pages 34, 38
- [118] W. Su, R. Bahr, S. A. Nauroze, and M. M. Tentzeris, "3D printed reconfigurable helical antenna based on microfluidics and liquid metal alloy," in *2016 IEEE International Symposium on Antennas and Propagation (APSURSI)*. IEEE, jun 2016, pp. 469–470. [Online]. Available: <http://ieeexplore.ieee.org/document/7695943/> → pages 34
- [119] E. Park, M. Lee, and S. Lim, "Switchable Bandpass/Bandstop Filter Using Liquid Metal Alloy as Fluidic Switch." *Sensors (Basel, Switzerland)*, vol. 19, no. 5, mar 2019. [Online]. Available: <http://www.ncbi.nlm.nih.gov/pubmed/30832422><http://www.pubmedcentral.nih.gov/articlerender.fcgi?artid=PMC6427611> → pages 34
- [120] M. Li and N. Behdad, "Fluidically tunable frequency selective/phase shifting surfaces for high-power microwave applications," *IEEE Transactions on Antennas and Propagation*, vol. 60, no. 6, pp. 2748–2759, 2012. → pages 35
- [121] M. R. Khan, G. J. Hayes, S. Zhang, M. D. Dickey, and G. Lazzi, "A pressure responsive fluidic microstrip open stub resonator using a liquid metal alloy," *IEEE Microwave and Wireless Components Letters*, vol. 22, no. 11, pp. 577–579, 2012. → pages 35, 38
- [122] Z. Wu, K. Hjort, and S. H. Jeong, "Microfluidic stretchable radio-frequency devices," *Proceedings of the IEEE*, vol. 103, no. 7, pp. 1211–1225, 2015. → pages 35

- [123] C. Koo, B. E. Leblanc, M. Kelley, H. E. Fitzgerald, G. H. Huff, and A. Han, "Manipulating Liquid Metal Droplets in Microfluidic Channels with Minimized Skin Residues Toward Tunable RF Applications," *Journal of Microelectromechanical Systems*, vol. 24, no. 4, pp. 1069–1076, 2015. → pages 36, 37, 39
- [124] M. R. Khan, C. Trlica, J. H. So, M. Valeri, and M. D. Dickey, "Influence of water on the interfacial behavior of gallium liquid metal alloys," *ACS Applied Materials and Interfaces*, vol. 6, no. 24, pp. 22 467–22 473, 2014. → pages 36
- [125] M. D. Dickey, R. C. Chiechi, R. J. Larsen, E. A. Weiss, D. A. Weitz, and G. M. Whitesides, "Eutectic gallium-indium (EGaIn): A liquid metal alloy for the formation of stable structures in microchannels at room temperature," *Advanced Functional Materials*, vol. 18, no. 7, pp. 1097–1104, 2008. → pages 36
- [126] M. Kelley, C. Koo, H. McQuilken, B. Lawrence, S. Li, A. Han, and G. Huff, "Frequency reconfigurable patch antenna using liquid metal as switching mechanism," *Electronics Letters*, vol. 49, no. 22, pp. 1370–1371, 2013. → pages 37
- [127] A. P. Saghati, J. Batra, J. Kameoka, and K. Entesari, "Microfluidically-tuned miniaturized planar microwave resonators," in *WAMICON 2014*. IEEE, jun 2014, pp. 1–3. [Online]. Available: <http://ieeexplore.ieee.org/document/6857750/> → pages 37
- [128] A. Dey, R. Guldiken, and G. Mumcu, "Wideband frequency tunable liquid metal monopole antenna," *IEEE Antennas and Propagation Society, AP-S International Symposium (Digest)*, no. 1, pp. 392–393, 2013. → pages 37
- [129] Darwin Microfluidics, "Microfluidic Dual Programmable Syringe Pump 11 Pico Plus Elite," 2019. → pages 37
- [130] R. C. Gough, A. M. Morishita, J. H. Dang, M. R. Moorefield, W. A. Shiroma, and A. T. Ohta, "Rapid electrocapillary deformation of liquid metal with reversible shape retention," *Micro and Nano Systems Letters*, vol. 3, no. 1, 2015. → pages 38
- [131] A. Pourghorban Saghati, J. Singh Batra, J. Kameoka, and K. Entesari, "A Microfluidically Reconfigurable Dual-Band Slot Antenna with

- a Frequency Coverage Ratio of 3:1,” *IEEE Antennas and Wireless Propagation Letters*, vol. 15, pp. 122–125, 2016. → pages 38
- [132] A. Ebrahimi, J. Scott, and K. Ghorbani, “Microwave Microfluidic Sensor Using Microstrip Line Terminated with LC Resonators,” in *2019 International Conference on Electromagnetics in Advanced Applications (ICEAA)*. IEEE, sep 2019, pp. 548–551. [Online]. Available: <https://ieeexplore.ieee.org/document/8879099/> → pages 38
- [133] A. P. Saghati, J. S. Batra, J. Kameoka, and K. Entesari, “A metamaterial-inspired miniaturized wide-band microwave interferometry sensor for liquid chemical detection,” *IEEE MTT-S International Microwave Symposium Digest*, vol. 2016-Augus, pp. 1–3, 2016. → pages 38
- [134] M. Lee, H. Son, D. Lim, S. Lee, and S. Lim, “Liquid-metal-fluidically polarization reconfigurable microstrip patch antenna,” *Microwave and Optical Technology Letters*, vol. 61, no. 10, pp. 2306–2314, 2019. → pages 39
- [135] Y. Temiz, R. D. Lovchik, G. V. Kaigala, and E. Delamarche, “Microelectronic Engineering Lab-on-a-chip devices : How to close and plug the lab ?” *MICROELECTRONIC ENGINEERING*, vol. 132, pp. 156–175, 2015. [Online]. Available: <http://dx.doi.org/10.1016/j.mee.2014.10.013> → pages 39
- [136] B. D. Wiltshire, S. Mohammadi, and M. H. Zarifi, “Integrating 3D Printed Microfluidic Channels with Planar Resonator Sensors for Low Cost and Sensitive Liquid Detection,” *Proceedings - ANTEM 2018: 2018 18th International Symposium on Antenna Technology and Applied Electromagnetics*, vol. 2018-Augus, pp. 1–2, 2018. → pages 39
- [137] S. D. Romano and P. A. Sorichetti, *Dielectric Spectroscopy in Biodiesel Production and Characterization*, ser. Green Energy and Technology, H. Machrafi, Ed. London: Springer London, aug 2011. [Online]. Available: <http://www.eurekaselect.com/102081/volume/1http://link.springer.com/10.1007/978-1-84996-519-4> → pages 40, 41
- [138] S. I. Y. Al-Mously, “A Modified Complex Permittivity Measurement Technique at Microwave Frequency,” *International Journal on New Computer Architectures and Their Applications*, vol. 2, no. 2, pp. 389–401, 2012. → pages 40

- [139] N. Hosseini, M. Baghelani, and M. Daneshmand, "Discrete Microwave Spectroscopy using Planar Resonator," *2019 IEEE Canadian Conference of Electrical and Computer Engineering, CCECE 2019*, pp. 1–4, 2019. → pages 40, 41
- [140] J. Baker-Jarvis, E. J. Vanzura, and W. A. Kissick, "Improved technique for determining complex permittivity with the transmission/reflection method," *IEEE Transactions on Microwave Theory and Techniques*, vol. 38, no. 8, pp. 1096–1103, 1990. → pages 40
- [141] P. M. Narayanan, "Microstrip transmission line method for broadband permittivity measurement of dielectric substrates," *IEEE Transactions on Microwave Theory and Techniques*, vol. 62, no. 11, pp. 2784–2790, 2014. → pages 40
- [142] Agilent Technologies, "Basics of Measuring the Dielectric Properties of Materials," *Measurement Techniques*, p. 33, 2013. [Online]. Available: [#](http://scholar.google.com/scholar?hl=en&btnG=Search&q=intitle:Basics+of+Measuring+the+Dielectric+Properties+of+Materials)2 → pages 41
- [143] A. Talai, F. Steinheusser, A. Bittner, U. Schmid, R. Weigel, and A. Koelpin, "A permittivity characterization method by detuned ring-resonators for bulk materials up to 110 GHz," in *2014 44th European Microwave Conference*, vol. 2, no. c. IEEE, oct 2014, pp. 124–127. [Online]. Available: <http://ieeexplore.ieee.org/document/6986385/> → pages 41
- [144] K. Grenier, F. Artis, M. Poupot, J.-J. Fournie, and D. Dubuc, "Label-free discrimination of human lymphoma cell sub-populations with microwave dielectric spectroscopy," in *2018 IEEE/MTT-S International Microwave Symposium - IMS*. IEEE, jun 2018, pp. 907–910. [Online]. Available: <https://ieeexplore.ieee.org/document/8439472/> → pages 42
- [145] Y.-f. Chen, H.-w. Wu, Y.-h. Hong, H.-y. Lee, and H.-y. Lee, "Author 's Accepted Manuscript 40 GHz RF Biosensor Based on Microwave Coplanar Waveguide Transmission Line for Cancer Cells ( HepG2 ) Dielectric Characterization \* Corresponding Author : Prof . Hung-Wei Wu," *Biosensors and Bioelectronic*, 2014. [Online]. Available: <http://dx.doi.org/10.1016/j.bios.2014.05.060> → pages 42

- [146] P. Velez, L. Su, K. Grenier, J. Mata-Contreras, D. Dubuc, and F. Martin, “Microwave Microfluidic Sensor Based on a Microstrip Splitter/Combiner Configuration and Split Ring Resonators (SRRs) for Dielectric Characterization of Liquids,” *IEEE Sensors Journal*, vol. 17, no. 20, pp. 6589–6598, 2017. → pages 42
- [147] A. A. Abduljabar, N. Clark, J. Lees, and A. Porch, “Dual Mode Microwave Microfluidic Sensor for Temperature Variant Liquid Characterization,” *IEEE Transactions on Microwave Theory and Techniques*, vol. 65, no. 7, pp. 2572–2582, 2017. → pages
- [148] A. A. Abduljabar, D. J. Rowe, A. Porch, and D. A. Barrow, “Novel microwave microfluidic sensor using a microstrip split-ring resonator,” *IEEE Transactions on Microwave Theory and Techniques*, vol. 62, no. 3, pp. 679–688, 2014. → pages
- [149] A. Ebrahimi, J. Scott, and K. Ghorbani, “Ultrahigh-Sensitivity Microwave Sensor for Microfluidic Complex Permittivity Measurement,” *IEEE Transactions on Microwave Theory and Techniques*, vol. 67, no. 10, pp. 4269–4277, 2019. → pages 42
- [150] K. Grenier, D. Dubuc, T. Chen, F. Artis, T. Chretiennot, M. Poupot, and J. Fournié, “Recent Advances in Microwave-Based Dielectric Spectroscopy at the Cellular Level for Cancer Investigations,” *IEEE Transactions on Microwave Theory and Techniques*, vol. 61, no. 5, pp. 2023–2030, 2013. → pages 42
- [151] A. P. Saghati, J. S. Batra, J. Kameoka, and K. Entesari, “A Metamaterial-Inspired Wideband Microwave Interferometry Sensor for Dielectric Spectroscopy of Liquid Chemicals,” *IEEE Transactions on Microwave Theory and Techniques*, vol. 65, no. 7, pp. 2558–2571, 2017. → pages 42
- [152] A. Albishi, “Intelligent Sensing Using Multiple Sensors for Material Characterization,” *MDPI*, no. November, 2019. → pages 42
- [153] N. Hosseini, M. Baghelani, and M. Daneshmand, “Selective Volume Fraction Sensing Using Resonant-Based Microwave Sensor and Its Harmonics,” *IEEE Transactions on Microwave Theory and Techniques*, pp. 1–1, 2020. → pages 43
- [154] M. A. Rafi, B. D. Wiltshire, and M. H. Zarifi, “Wideband Tunable Modified Split Ring Resonator Structure Using Liquid Metal and 3-D

- Printing,” *IEEE Microwave and Wireless Components Letters*, vol. 30, no. 5, pp. 1–4, 2020. → pages 44, 73
- [155] O. Sydoruk, E. Tatartschuk, E. Shamonina, and L. Solymar, “Analytical formulation for the resonant frequency of split rings,” *Journal of Applied Physics*, vol. 105, no. 1, pp. 1–5, 2009. → pages 45
- [156] I. A. Al-Naib, C. Jansen, and M. Koch, “Thin-film sensing with planar asymmetric metamaterial resonators,” *Applied Physics Letters*, vol. 93, no. 8, 2008. → pages 45
- [157] P. Sehgal and K. Patel, “Dual-wideband CPW-fed monopole antenna with circular split-ring resonators,” *2020 7th International Conference on Signal Processing and Integrated Networks, SPIN 2020*, pp. 1078–1083, 2020. → pages 45
- [158] M. C. Jain, A. V. Nadaraja, B. M. Vizcaino, D. J. Roberts, and M. H. Zarifi, “Differential Microwave Resonator Sensor Reveals Glucose-Dependent Growth Profile of E. coli on Solid Agar,” *IEEE Microwave and Wireless Components Letters*, vol. 30, no. 5, pp. 531–534, 2020. → pages 47
- [159] S. Zahertar, A. D. Yalcinkaya, and H. Torun, “Rectangular split-ring resonators with single-split and two-splits under different excitations at microwave frequencies,” *AIP Advances*, vol. 5, no. 11, p. 117220, nov 2015. [Online]. Available: <http://dx.doi.org/10.1063/1.4935910><http://aip.scitation.org/doi/10.1063/1.4935910> → pages 47
- [160] E. MacDonald, R. Salas, D. Espalin, M. Perez, E. Aguilera, D. Muse, and R. B. Wicker, “3D printing for the rapid prototyping of structural electronics,” *IEEE Access*, vol. 2, no. December, pp. 234–242, 2014. → pages 49
- [161] E. L. Chuma, Y. Iano, G. Fontgalland, and L. L. Bravo Roger, “Microwave sensor for liquid dielectric characterization based on metamaterial complementary split ring resonator,” *IEEE Sensors Journal*, vol. 18, no. 24, pp. 9978–9983, 2018. → pages 68
- [162] T. Islam, S. C. Mukhopadhyay, and N. K. Suryadevara, “Smart Sensors and Internet of Things: A Postgraduate Paper,” *IEEE Sensors Journal*, vol. 17, no. 3, pp. 577–584, 2017. → pages 70

- 
- [163] A. Ebrahimi, W. Withayachumnankul, S. Al-Sarawi, and D. Aboott, “High-Sensitivity Metamaterial-Inspired Sensor,” *IEEE Sens. J.*, vol. 14, no. 14(5), pp. 1345–1351, 2014. → pages
- [164] N. Sharafadinzadeh, M. Abdolrazzagli, and M. Daneshmand, “Investigation on planar microwave sensors with enhanced sensitivity from microfluidic integration,” *Sensors and Actuators, A: Physical*, vol. 301, p. 111752, 2020. [Online]. Available: <https://doi.org/10.1016/j.sna.2019.111752> → pages
- [165] —, “Highly sensitive microwave split ring resonator sensor using gap extension for glucose sensing,” *2017 IEEE MTT-S International Microwave Workshop Series on Advanced Materials and Processes for RF and THz Applications, IMWS-AMP 2017*, vol. 2018-Janua, no. September, pp. 1–3, 2018. → pages
- [166] P. Velez, K. Grenier, J. Mata-Contreras, D. Dubuc, and F. Martin, “Highly-sensitive microwave sensors based on Open Complementary Split Ring Resonators (OCSRRs) for dielectric characterization and solute concentration measurement in liquids,” *IEEE Access*, vol. 6, no. c, pp. 48 324–48 338, 2018. → pages 70
- [167] X. Bao, M. Zhang, I. Ocket, J. Bao, D. Kil, Z. Liu, R. Puers, D. Schreurs, and B. Nauwelaers, “Integration of Interdigitated Electrodes in Split-Ring Resonator for Detecting Liquid Mixtures,” *IEEE Transactions on Microwave Theory and Techniques*, vol. 68, no. 6, pp. 2080–2089, 2020. → pages 70
- [168] X. Bao, I. Ocket, G. Crupi, D. Schreurs, J. Bao, D. Kil, B. Puers, and B. Nauwelaers, “A planar one-port microwave microfluidic sensor for microliter liquids characterization,” *IEEE Journal of Electromagnetics, RF and Microwaves in Medicine and Biology*, vol. 2, no. 1, pp. 10–17, 2018. → pages 70
- [169] D. Lu, Y. Zheng, A. Penirschke, and R. Jakoby, “Highly sensitive dual-mode relative humidity sensor based on integrated SAW and LC resonators,” *Electronics Letters*, vol. 51, no. 16, pp. 1219–1220, 2015. → pages 70
- [170] S. Mohammadi, A. Vijaya Nadaraja, K. Luckasavitch, M. Chhajjer Jain, D. Roberts, and M. H. Zarifi, “A Label-free, non-Intrusive, and

## Bibliography

---

- Rapid Monitoring of Bacterial Growth on Solid Medium using Microwave Biosensor,” *IEEE Transactions on Biomedical Circuits and Systems*, vol. 14, no. 1, pp. 1–1, 2019. → pages 75
- [171] Agilent Technologies, “Oscilloscope Fundamentals,” *IEEE Communications Magazine*, vol. 42, no. 5, pp. 5–5, 2004. → pages 89